SINGLE PHOTON COUNTING X-RAY DIFFRACTION TECHNIQUES FOR THE INVESTIGATION OF SHOCK COMPRESSED CONDENSED MATTER

SHAMIM PATEL



A thesis submitted for the degree of *Doctor of Philosophy*

St. John's College

University of Oxford

Trinity Term, 2016

For my Parents

ACKNOWLEDGMENTS

First and foremost I'd like to thank my supervisor, Justin, for giving me the opportunity to work in his group in addition to his invaluable direction during my DPhil. I am also incredibly grateful to Matt, not only for his advice (of which there was a great deal) but also for putting up with me for *so many* hours in TA1 at Janus. I'd also like to thank the numerous members of the Simon room during my time here, both for their help, and their unwavering willingness to go for coffee or to the pub. Finally I must thank Andy for all his help, from my very first day in the office to his continuing guidance. This thesis could never have been possible without him and I am truly thankful for all his contributions throughout the years.

My friends both in St. Johns and elsewhere also deserve a thank you for keeping me mostly sane, particularly during the more difficult periods of this DPhil. Thanks also go to my housemates, past and present, for providing me a welcoming home to come back to. A special thanks goes to Joe and Paul, who have both been resolute friends throughout my time in Oxford. I count myself as incredibly fortunate to have had all these people to support me.

Lastly I thank my parents. Their never ending and unconditional support made this possible.

ABSTRACT

X-ray diffraction has now become a key tool in dynamic compression experiments, with a rich variety of mature diagnostics available. It is a technique which measures the arrangement of atoms in solid material, a direct measurement of the structure and density of materials. This thesis presents two new diffraction diagnostics where the key innovation is the use of a single photon counting CCD to measure energy resolved diffraction signal. Using CCDs in this way has not been done before in a high power laser experiment. The first diagnostic measures diffraction from a poly-crystalline sample and along with experimental results, a simulation code was created to support the development of the technique. The second technique is for use with single crystal samples. The energy resolving ability of the CCD is shown to give extra information about the state of the compressed material it is probing. As an extension to the experimental work, Molecular Dynamics simulations of germanium are presented which show qualitative agreement with previous work in which a phase transition occurs. The structure of the phase changed material is covered in detail.

CONTENTS

1 INTRODUCTION 1
1.1 Extreme Conditions . . . 1
1.2 Shock Physics . . . 2
1.3 Experimental Techniques . . . 3
1.4 Thesis Layout and Role of the Author . . . 5

2 THEORY AND EXPERIMENTAL BACKGROUND 7
2.1 Crystal Structures . . . 7
2.1.1 Lattices . . . 7
2.1.2 Reciprocal Lattice . . . 10
2.1.3 Lattice Planes . . . 11
2.1.4 Strain . . . 12
2.2 X-ray Diffraction . . . 14
2.2.1 Bragg's Law . . . 15
2.2.2 Experimental Techniques . . . 17
2.3 Shock Waves . . . 20
2.3.1 Rankine-Hugoniot Conditions . . . 21
2.3.2 Shock Compressed Solids . . . 22
2.4 Diffraction From Strained Materials . . . 25
2.5 Laser Plasma Interactions . . . 27
2.5.1 Plasma Physics . . . 27
2.5.2 Shock Wave Generation . . . 31
2.5.3 X-ray Generation . . . 34

3 SINGLE PHOTON ENERGY DISPERSIVE X-RAY DIFFRACTION (SPEDX) 36
3.1 Introduction . . . 36
3.2 Single Photon CCD . . . 40
3.3 First Demonstration - Janus 2012 . . . 44
3.4 Driven SPEDX - Vulcan 2013 . . . 47
3.5 Simulations . . . 56

3.6 Energy Correlations 64
3.7 Imaging Pinhole 66
3.8 Conclusion 69

4 SINGLE HIT ENERGY RESOLVED LAUE DIFFRACTION (SHIELD) 70
4.1 Introduction 70
4.2 Experiment - Janus 2014 72
4.3 Results 75
4.4 Analysis 81
4.4.1 X-ray Pulse Timings 84
4.4.2 Inelastic Wave Speeds 87
4.4.3 Diffraction Prediction 88
4.5 Experiment - Janus 2015 91
4.5.1 Analysis 92
4.5.2 Elastic Strains 96
4.6 Conclusion 99

5 MOLECULAR DYNAMICS SIMULATIONS OF SHOCK COMPRESSED GERMANIUM 100
5.1 Introduction 100
5.2 Simulation Details 102
5.2.1 Potentials 102
5.2.2 Shock Method 103
5.2.3 Initial Conditions 104
5.3 Shock Response 106
5.3.1 Simulation Benchmarking 109
5.3.2 Size Effects 113
5.4 Phase Change 115
5.4.1 Coordination Number 115
5.4.2 Band Structures 116
5.4.3 Unusual Phase Transition Location 119
5.4.4 Phase-changed Structure 123
5.4.5 Potential Stability 129
5.5 Conclusion 132

6 CONCLUSIONS 133
6.1 Single Photon Energy Dispersive X-ray Diffraction (SPEDX) . . 133

6.2 Single Hit Energy resolved Laue Diffraction (SHiELD) 136
6.3 MD Simulations of Shock Compressed Germanium 138
6.4 Summary 139
6.5 Future Work 140

REFERENCES 142

1

INTRODUCTION

1.1 EXTREME CONDITIONS

Solid materials subjected to extremely high pressures and densities are highly common throughout nature [1–4]. There have been efforts for many decades to investigate these conditions; a key motivator of these studies is to understand the properties of materials in planetary interiors [5–7]. Gaining an understanding of these materials, their structure and behaviour, would give insight not only into the structure of the Earth, but also the formation of exoplanets and other celestial bodies [8–10]. This is an increasingly active field, with the recent successes of the Kepler satellite in detecting over a thousand confirmed exoplanets [11].

Despite the fact that the bulk of planetary material is in a high density state, from an experimental viewpoint we know relatively little about how it behaves in these conditions. In fact, a recent result corrected the inner core boundary temperature of the Earth by several hundred Kelvin [12]. Even with significant experimental and theoretical efforts, the behaviour of materials at these extreme pressures and densities remains an active area of research [13–16].

Research in this area is also relevant to other planets in our solar system. A particularly captivating area is the proposition that there are iceberg sized diamonds on Neptune [17]. More recent work has been done investigating the

conductive properties of high pressure ice, which has consequences for the interiors of both Neptune and Uranus [18, 19].

Use of diamond anvil cells are one method which has been used for many years to examine the behaviour of matter at high pressures [20]. The diamond anvil cell follows earlier work by Bridgman in 1911 where opposing steel pistons were used to subject materials to high pressures [21]. The incompressibility of diamond led to it replacing the steel pistons, which continues to this day [22, 23]. There are numerous designs of such devices which have enabled very precise high pressure investigations of matter, including the use of secondary diagnostics such as x-ray diffraction to make structural measurements [24].

High pressure research also has a more commercial application in Inertial Confinement Fusion (ICF) [25–27]. With the National Ignition Facility (NIF) now online, there has been rapid progress in ICF research. The capsule implosion, at the core of ICF experiment, is a highly complex process. It takes the capsule through a large range of phase space - from cryogenic conditions, through to temperatures of hundreds of eV and pressures of hundreds of thousands of GPa. As ignition has not yet been successfully achieved, understanding the behaviour of materials as they are compressed to such extreme conditions will be vital in achieving this goal.

1.2 SHOCK PHYSICS

For many decades, shock waves have been used to compress materials to high pressures. Early work on iron in the 1940's and 50's was performed using explosively driven shock waves [28, 29]. This period was a time of rapid development in the materials community. Shock wave techniques allowed the study

of pressures beyond those available to static compression techniques, such as diamond anvil cells. This remains true even after significant progress in both fields [30, 31].

These dynamic compression experiments were performed initially by explosive drives, but later research utilised gas driven flyer plates [32]. These gas gun techniques made high pressure research practical for a larger number of researchers, given the logistical issues with using explosives. Gas gun techniques remain a method of acquiring extremely precise material measurements to this day [33].

In order to reach higher pressures, high intensity lasers and laser ablation can be used to generate shock waves in materials [34, 35]. Many of the early lasers in this field were developed for ICF research; however, there are now a number of large laser facilities in the world where materials science, performed using shock waves, is a key focus [36–38]. These facilities can reach conditions well beyond the current ≈ 7.7 MBar limit of diamond anvil cells [15, 31].

1.3 EXPERIMENTAL TECHNIQUES

Making accurate measurements of these extreme states continues to be an active area of research. There are a number of mature diagnostics used in high power laser experiments (though not exclusively) to measure both bulk properties of materials and detailed structural information.

1.3.0.1 *VISAR*

The Velocity System for Any Reflector (VISAR) was developed to perform velocity measurements over short timescale experiments [39]. It is an interfer-

ometry based diagnostic where light is reflected from the rear surface, i.e. the surface opposite the drive side, of the sample being probed. The light is split and passed through two paths of identical physical length. One path includes a precisely known length of glass which adds a precise optical length to the path. Upon recombination this produces a wavefront with an interference pattern. This interference pattern changes depending on the time-dependent phase of the light which enters the interferometer. This time-dependent profile of the light is directly related to the rear surface velocity of the sample. Using a streak camera, or other time-resolved light sensing diagnostic, the interference pattern can be recorded. This pattern can then be analysed to recover the rear surface velocity. The rear surface velocity is directly related to the in-situ particle velocity, U_p, which can then be used to infer material properties under compression [40].

In particular this was an improvement over previous techniques, especially for laser shock experiments and their correspondingly short timescales [41]. It has become a key diagnostic for shock wave experiments, and is particularly vital in ramp compression experiments - which is an increasingly active area of research [42–46].

1.3.0.2 *X-ray Diffraction*

X-ray diffraction offers a method of measuring the arrangement of atoms, or molecules, within the material *in-situ*. Early work used flash x-ray sources [47, 48], but later efforts made use of lasers to generate both the x-ray source and shock wave [49, 50]. There are now a number of different x-ray diffraction platforms, some of which are outlined later in this thesis.

1.4 THESIS LAYOUT AND ROLE OF THE AUTHOR

Much of the work in this thesis, particularly the experimental elements, were performed within a large experimental collaboration. Therefore it is inevitable that other individuals had large contributions. This section highlights the specific areas where the author had a major role as well as identifying where others had key inputs. Where the work in this thesis does not reference other material, or is not highlighted here as having had contributions from others - then it is the sole work of the author. For experimental campaigns, planning included designing experimental geometry and attending planning meetings with facility staff. Where the author was present for the experiment then he was a core member and made major contributions to the majority of elements in its running. These are too numerous to explicitly list in detail here.

Chapter 2 gives a brief review of the basic theoretical concepts, along with outlines of the experimental methods used in modern in-situ x-ray diffraction. The chapter covers basic crystal theory and lattices, with a focus on being relevant for diffraction. This is followed by a description of x-ray diffraction and how it can be applied to compressed materials. The material covered here is taken from literature and is not the author's work.

Chapter 3 covers the design and development of SPEDX. The initial experiment was performed and led by Andrew Higginbotham, Matthew Suggit, Orlando Ciricosta (who wrote the first version of the single photon analysis code) and James Hawreliak. The author was heavily involved in the analysis of this experiment. This experiment was published in [51], of which the author co-wrote a significant portion and as a result was placed as second author on the paper. The author was a core part of the experimental team which planned and

performed the second experiment at the Vulcan laser, and also performed all of the analysis for the experiment. The development of the SPEDX simulation code and analysis of the results was the work of the author.

Chapter 4 describes the SHiELD technique. Again the author was a core part of both experimental teams which worked on this. The analysis of the x-ray diffraction patterns was performed by the author. The code to extract rear surface velocity profiles was written by Paul Stubley and used by the author. Detailed analysis using this information in combination with diffraction patterns was done by the author. The results from the first experimental campaign are published in [52] where this author wrote the whole manuscript and is listed as the first author. Editing of the manuscript involved contributions from many of the other listed authors.

Chapter 5 outlines a Molecular Dynamics study of germanium. The analysis of the simulation runs were performed by the author, using code written principally by Andrew Higginbotham. A number of additions to this analysis code were made by the author, in particular concerning the analysis using coordination number. Detailed analysis of simulation outputs was performed solely by the author, as were identifying the structural parameters of the phase changed material. The original 3dPcf analysis code was written by Andrew Higginbotham but minor modifications were made by the author for this work.

Chapter 6 gives conclusions of the work in the three previous chapters. A summary of the thesis and suggestions for future work are also discussed.

2

THEORY AND EXPERIMENTAL BACKGROUND

2.1 CRYSTAL STRUCTURES

2.1.1 *Lattices*

A crystal is made up of large numbers of repeating units, known as the unit cell. For a 3-dimensional crystal, the unit cell is comprised of one or more atoms arranged in 3D. The unit cell is repeated in 3 dimensions, such that all the space is filled by the repeated cell. It is described in terms of its lattice vectors, $\mathbf{a}_1, \mathbf{a}_2$ and $\mathbf{a}_3$. These vectors define the three edges of the unit cell and give it's size and shape. The three vectors must be non-coplanar such that the volume of the unit cell, v is given by,

$$v = \mathbf{a}_1 \cdot \mathbf{a}_2 \times \mathbf{a}_3 \neq 0 \tag{1}$$

In general, the lengths of these vectors and the angles between them, usually denoted by α, β and γ, can be arbitrary. If $\mathbf{a}_1, \mathbf{a}_2$ and $\mathbf{a}_3$ have the same length and are orthogonal, i.e. $\alpha = \beta = \gamma = 90°$ then the unit cell is cubic. For a cubic lattice it is useful to define a single lattice constant, a_0, which gives the side length of the cubic unit cell.

The lattice can then be constructed by translating unit cells by integer multiples of the lattice vectors, i.e. a vector:

Table 1: Table of lattice systems and corresponding properties of lattice vectors.

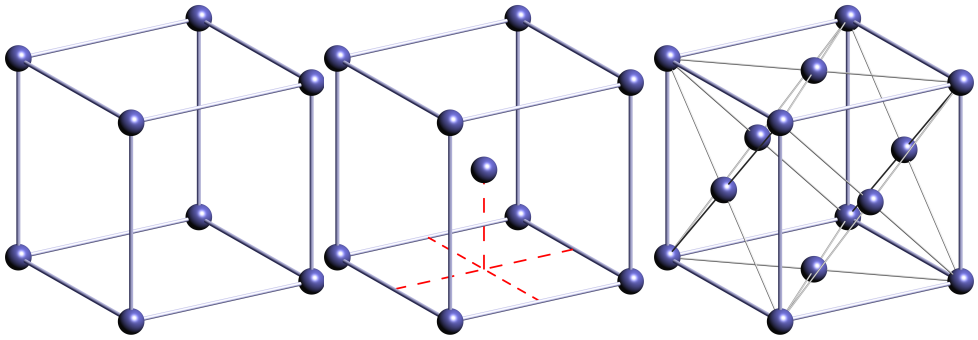
Triclinic	$a_1 \neq a_2 \neq a_3; \alpha \neq \beta \neq \gamma \neq 90°$
Monoclinic	$a_1 \neq a_2 \neq a_3; \beta > 90°, \alpha = \gamma = 90°$
Orthorhombic	$a_1 \neq a_2 \neq a_3; \alpha = \beta = \gamma = 90°$
Trigonal	$a_1 = a_2 = a_3; \alpha = \beta = \gamma < 120°$
	$a_1 = a_2 \neq a_3; \alpha = \beta = 90°, \gamma = 120°$
Tetraganol	$a_1 = a_2 \neq a_3; \alpha = \beta = \gamma = 90°$
Hexaganol	$a_1 = a_2 \neq a_3; \alpha = \beta = 90°, \gamma = 120°$
Cubic	$a_1 = a_2 = a_3; \alpha = \beta = \gamma = 90°$

$$\mathbf{R} = n_1\mathbf{a}_1 + n_2\mathbf{a}_2 + n_3\mathbf{a}_3 \tag{2}$$

where n_1, n_2 and n_3 are integers, including zero. Lattice points are equivalent such that the lattice will appear to be equivalent if the origin is placed at any lattice point. There are seven lattice systems, which are summarised in table 1. For each lattice system, additional lattices can be constructed by adding points, atoms or molecules, to the unit cell.

The primitive unit cell is one which has the smallest volume, but will still fill the volume of the lattice when repeated. A primitive unit cell will contain only a single lattice point, however it is often more convenient to use larger unit cells that can contain multiple lattice points. There are 14 distinct lattices, known as Bravais lattices.

One of the most common lattice systems found in nature is the cubic lattice. It is the lattice system with the highest symmetry. There are three Bravais lattice types which form cubic crystals; simple cubic, body centred cubic (BCC) and face centred cubic (FCC). These are shown in Fig. 1. Note that the unit cell displayed for FCC is not the primitive unit cell, but the more conventionally used one.



(a) Simple Cubic (b) BCC (c) FCC

Figure 1: Unit cells for the three cubic lattices.

The BCC unit cell can be created by adding an additional lattice point at the centre of every simple cubic cell, to total two lattice points per unit cell. The FCC unit cell instead adds points on the faces of the cell, totalling 4 lattice points per cell. The basis of a unit cell describes the positions of atoms, $\mathbf{r}_i$, relative to the lattice points. Therefore the positions of atoms in the crystal can be given by,

$$\mathbf{R}_i = n_1\mathbf{a}_1 + n_2\mathbf{a}_2 + n_3\mathbf{a}_3 + \mathbf{r}_i \tag{3}$$

$$\mathbf{r}_1 = \mathbf{0}, \mathbf{r}_2 = \frac{1}{2}(\mathbf{a}_1 + \mathbf{a}_2 + \mathbf{a}_3) \text{ (BCC)} \tag{4}$$

$$\mathbf{r}_1 = \mathbf{0}, \mathbf{r}_2 = \frac{1}{2}(\mathbf{a}_1 + \mathbf{a}_2), \mathbf{r}_3 = \frac{1}{2}(\mathbf{a}_2 + \mathbf{a}_3), \mathbf{r}_3 = \frac{1}{2}(\mathbf{a}_3 + \mathbf{a}_1) \text{ (FCC)} \tag{5}$$

Cubic Diamond (CD) is also a common cubic structure. Elements such as silicon and germanium have CD structures at ambient conditions. It is comprised of an FCC lattice with a two atom basis:

$$\mathbf{r}_1 = \mathbf{0}, \mathbf{r}_2 = \frac{1}{4}(\mathbf{A}_1 + \mathbf{A}_2 + \mathbf{A}_3) \tag{6}$$

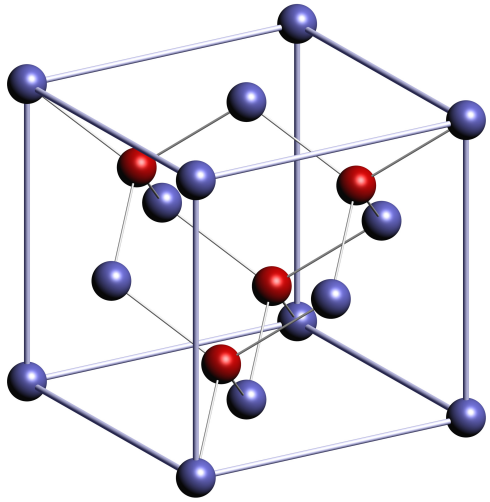


Figure 2: Unit cell for the cubic diamond structure. The atoms coloured in blue are identical to the FCC lattice whilst the red atoms represent the extra basis atoms.

Where $\mathbf{A}_i$ denotes the lattice vectors of the conventional unit cell. This leads to a unit cell with four lattice points and eight atoms per unit cell. Note this means that not all atoms lie on lattice points, which is in contrast to the cubic structures previously discussed. A diagram of the cubic diamond unit cell is given in Fig. 2.

2.1.2 *Reciprocal Lattice*

Given the three real space lattice vectors, $\mathbf{a}_1, \mathbf{a}_2$ and $\mathbf{a}_3$, the reciprocal lattice vectors, $\mathbf{b}_1, \mathbf{b}_2$ and $\mathbf{b}_3$, can be constructed using,

$$\mathbf{b}_1 = 2\pi \frac{\mathbf{a}_2 \times \mathbf{a}_3}{\mathbf{a}_1 \cdot (\mathbf{a}_2 \times \mathbf{a}_3)} \tag{7}$$

$$\mathbf{b}_2 = 2\pi \frac{\mathbf{a}_3 \times \mathbf{a}_1}{\mathbf{a}_1 \cdot (\mathbf{a}_2 \times \mathbf{a}_3)} \tag{8}$$

$$\mathbf{b}_3 = 2\pi \frac{\mathbf{a}_1 \times \mathbf{a}_2}{\mathbf{a}_1 \cdot (\mathbf{a}_2 \times \mathbf{a}_3)} \tag{9}$$

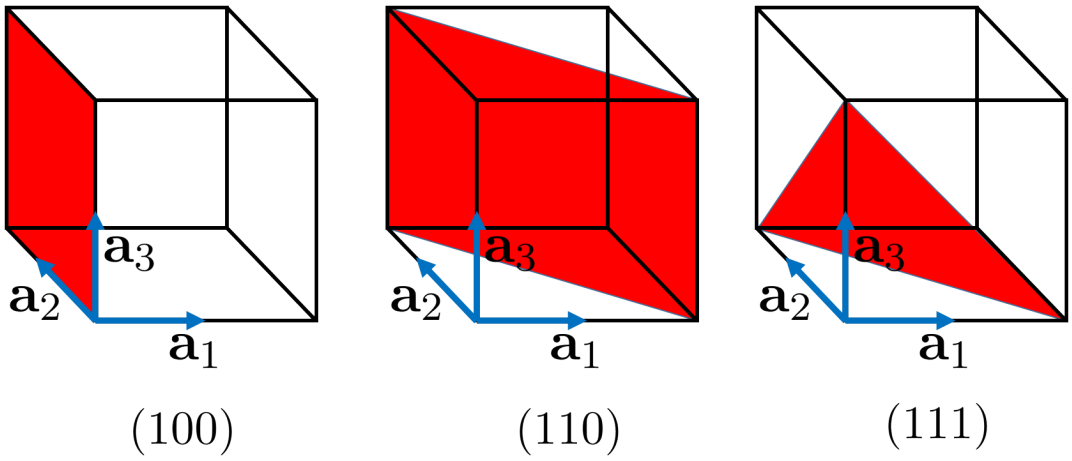


Figure 3: Examples of lattice planes in a cubic unit cell.

Reciprocal lattice points are constructed in the same manner as in equation 2 and the reciprocal lattice vector, or scattering vector, is given by,

$$\mathbf{G}_{hkl} = h\mathbf{b}_1 + k\mathbf{b}_2 + l\mathbf{b}_3 \tag{10}$$

2.1.3 *Lattice Planes*

Lattice planes are another useful geometric construct. Three lattice points, which do not lie on a straight line, can be used to construct a lattice plane. The lattice plane can be defined as a plane that intercepts the three points $\mathbf{a}_1/h, \mathbf{a}_2/k$ and $\mathbf{a}_3/l$, where h, k and l are integers. An equivalent definition is that the lattice plane (hkl) is orthogonal to the reciprocal lattice vector $\mathbf{G}_{hkl}$.

The conventional notation for a lattice plane is (hkl) where h, k, l are referred to as Miller indices. Miller indices are extremely widely used in crystallography, for example a direction in the crystal is denoted by,

$$[hkl] = h\mathbf{a}_1 + k\mathbf{a}_2 + l\mathbf{a}_3 \tag{11}$$

For a cubic crystal, the direction $[hkl]$ is perpendicular to the set of planes (hkl), which follows from the definition of the reciprocal lattice vectors. Note that shocked crystals typically do not have cubic unit cells due the non isotropic stress on the material.

The perpendicular separation of lattice planes is an extremely important quantity in crystallography; for a lattice plane (hkl) it is given by,

$$d_{hkl} = \frac{2\pi}{|\mathbf{G}_{hkl}|} \tag{12}$$

This spacing between planes is referred to as the d-spacing, and for a cubic lattice is given simply by,

$$d_{hkl} = \frac{a_0}{\sqrt{h^2 + k^2 + l^2}} \tag{13}$$

2.1.4 *Strain*

In the context of high pressure reasearch, the structure of materials will be deformed in response to these conditions. In one dimension, the compressive engineering strain is defined as,

$$\epsilon = 1 - \frac{L_1}{L_0} = \frac{\Delta L}{L_0} \tag{14}$$

$$L_1 = L_0 - \Delta L \tag{15}$$

where L_0 and L_1 represent the initial and final lengths. ΔL is the reduction in length i.e. positive for a compression. Note that this definition of the *compressive* strain results in positive strain values under compression.

In three dimensions, the strain tensor takes a form similar to the stress tensor:

$$\underline{\underline{\epsilon}} = \begin{bmatrix} \epsilon_{11} & \epsilon_{12} & \epsilon_{13} \\ \epsilon_{21} & \epsilon_{22} & \epsilon_{23} \\ \epsilon_{31} & \epsilon_{32} & \epsilon_{33} \end{bmatrix} \tag{16}$$

$$= \begin{bmatrix} e_{11} & \frac{1}{2}(e_{12}+e_{21}) & \frac{1}{2}(e_{13}+e_{31}) \\ \frac{1}{2}(e_{21}+e_{12}) & e_{22} & \frac{1}{2}(e_{23}+e_{32}) \\ \frac{1}{2}(e_{31}+e_{13}) & \frac{1}{2}(e_{32}+e_{23}) & e_{33} \end{bmatrix} \tag{17}$$

Where the subscripts ϵ_{ij} indicate the direction, i, and plane, j, on which the strain acts and the indexes 1, 2, 3 can be interchanged with the directions x, y, z respectively. e_{ij} is defined as the variation of the displacement u_i in the direction x_j such that $e_{ij} = \partial u_i / \partial x_j$.

Note that as the strain tensor is diagonal, there are only six independent components. It is also diagonalisable, which means that it can be described as three orthogonal strains. Physically, this means that there is a choice of axes where the strain (and stress) state of the material can be fully described by three orthogonal strains.

A related tensor is the deformation tensor, $\underline{\underline{\alpha}}$, which is given by,

$$\underline{\underline{\alpha}} = 1 - \underline{\underline{\epsilon}} \tag{18}$$

$$\mathbf{R}_1 = \underline{\underline{\alpha}}\mathbf{R}_0 \tag{19}$$

where equation 19 shows how a point $\mathbf{R}_0$ in the unstrained lattice is transformed to a point in the strained lattice, $\mathbf{R}_1$.

The stress tensor, $\underline{\underline{\sigma}}$, is closely related to the strain tensor and for small strains can be given by Hooke's law:

$$\epsilon_{ij} = s_{ijkl}\sigma_{kl} \tag{20}$$

where s_{ijkl} represents the corresponding element of the elastic compliance tensor, $\underline{\underline{s}}$, which is a fourth-rank tensor. The pressure of a material can then be given by $P = \frac{1}{3}(\sigma_{11} + \sigma_{22} + \sigma_{33})$. The shear stress similarly defined as $\sigma_{33} - \frac{1}{2}(\sigma_{11} + \sigma_{22})$ where the uniaxial srain is applied along axis 3 or the z axis.

For large elastic deformations, Hooke's law needs to be rewritten in the form of incremental changes:

$$\Delta\epsilon_{ij} = s_{ijkl}(\underline{\underline{\epsilon}})\Delta\sigma_{kl} \tag{21}$$

where explicit reference has been made to the fact that the compliance tensor depends on the current strain in the system. Integration of this equation allows for large macroscopic changes to be accurately described.

2.2 X-RAY DIFFRACTION

X-ray diffraction has been used for over a century to investigate the crystalline structure of materials. The short wavelength of x-rays, of the order of 10^{-10} m, is comparable to the inter-atomic spacing of many solids. Therefore, materials are able to coherently scatter radiation of this wavelength. This allows x-rays to be used as an effective tool to investigate the structure of solids.

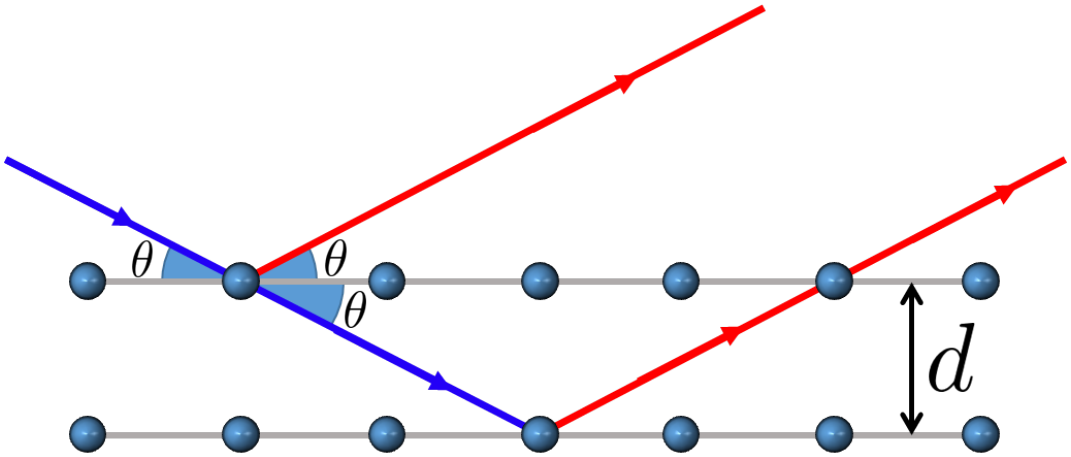


Figure 4: Diagram of x-ray paths in a solid leading to constructive interference.

2.2.1 *Bragg's Law*

Bragg's law describes the conditions for constructive interference of x-rays from planes of atoms, given radiation of a certain wavelength [53]. Diffraction occurs when radiation is scattered specularly by atoms in a lattice. X-ray scatter from atoms of two sequential planes of the same orientation, that is to say they are described by the same Miller indices. When the path difference of the x-rays is equal to an integer number of wavelengths, then constructive interference occurs resulting in a strongly reflected x-ray. This is shown schematically in Fig. 4. The condition for Bragg's law is then,

$$2d_{hkl}\sin(\theta) = n\lambda \tag{22}$$

The formulation of Bragg's law can also be expressed in vector form, with explicit reference to the direction of incoming and outgoing x-ray beams. This is given in equation 23.

$$\frac{\mathbf{s}-\mathbf{s}_0}{n\lambda} = \frac{\mathbf{G}_{hkl}}{2\pi} \tag{23}$$

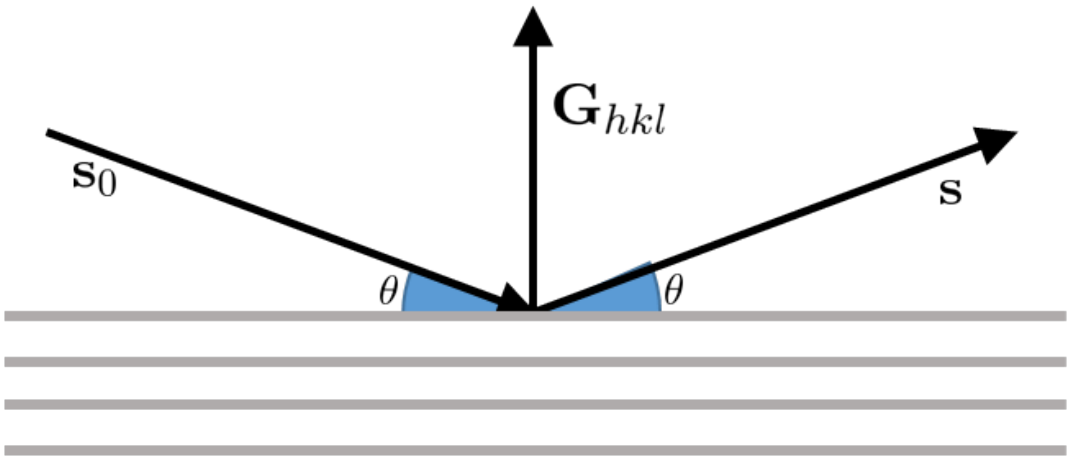


Figure 5: Diagram of x-ray input and output vectors, with reference to the angle they make with lattice planes and the scattering vector G_{hkl}.

where $\mathbf{s}_0$ and $\mathbf{s}$ are unit vectors describing the direction of the incoming and outgoing x-ray beams.

Equation 23 can easily be reduced to Bragg's law:

$$\left|\frac{\mathbf{s}-\mathbf{s}_0}{n\lambda}\right| = \left|\frac{\mathbf{G}_{hkl}}{2\pi}\right| \tag{24}$$

$$\frac{2\sin(\theta)}{n\lambda} = \frac{1}{d_{hkl}} \tag{25}$$

$$2d_{hkl}\sin(\theta) = n\lambda \tag{26}$$

Figure 5 shows how these quantities are related to each other geometrically. Note the direction of $\mathbf{G}_{hkl}$ relative to the lattice planes and that it bisects the angle between $\mathbf{s}$ and $\mathbf{s}_0$.

The Laue conditions are of use when considering diffraction from single crystal samples and are given as:

$$(\mathbf{s}-\mathbf{s}_0)\,.\mathbf{a}_0 = h\lambda \tag{27}$$

$$(\mathbf{s}-\mathbf{s}_0)\,.\mathbf{a}_1 = k\lambda \tag{28}$$

$$(\mathbf{s}-\mathbf{s}_0)\,.\mathbf{a}_2 = l\lambda \tag{29}$$

2.2.2 *Experimental Techniques*

There are a large variety of different diffraction platforms available. Here, three widely used techniques are introduced. These methods use a range of target types and x-ray sources. The methods presented here are far from exhaustive, but represent a large majority of in-situ diffraction experiments in the context of laser-plasma diffraction experiments.

2.2.2.1 *Divergent Beam Geometry*

This technique uses a monochromatic x-ray source which has a very large divergence [54–57]. The sample probed is a single crystal target. X-rays are incident on the sample at a large range of angles due to the divergence of the source. At certain angles, as governed by Bragg's law, the x-rays meet the condition for diffraction. Critically the angle of importance is the angle of the x-ray to the *lattice plane* and not to the surface of the sample; which in general are not the same. This typically results in an arc-like reflection, which is then recorded. This is shown schematically in Fig. 6.

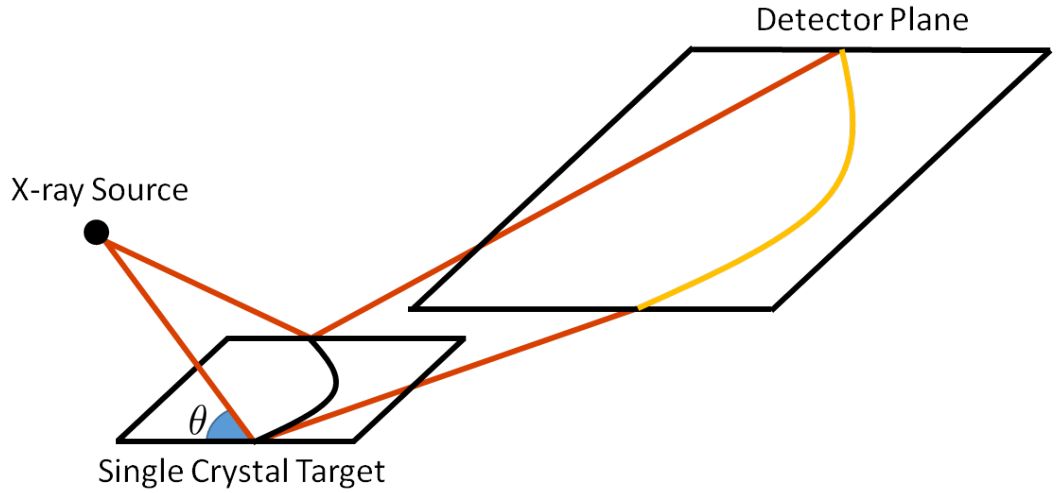


Figure 6: Diagram of divergent beam geometry.

2.2.2.2 *Laue Method*

As one of the first x-ray diffraction methods, this technique was used heavily in the early years of investigating the theory of crystalline solids. In contrast to the divergent beam geometry, a collimated (i.e. small divergence) x-ray beam is utilised. This x-ray beam is a broadband source, meaning that it is comprised of a large and continuous range of x-ray energies.

Once the x-rays irradiate the sample, the beam will meet the Laue condition with a number of lattice planes and a range of different Bragg angles. For each plane, its orientation and d-spacing will be different. Therefore the x-ray beam will be reflected to a large number of different points, which are then recorded on a, typically flat, detector [58–60].

2.2.2.3 *Powder Diffraction*

The previous techniques both probe single crystal samples. With this technique, the sample is instead a multi-crystalline sample. Whilst the title 'powder' literally implies dust like samples, it also includes targets such as metal foils.

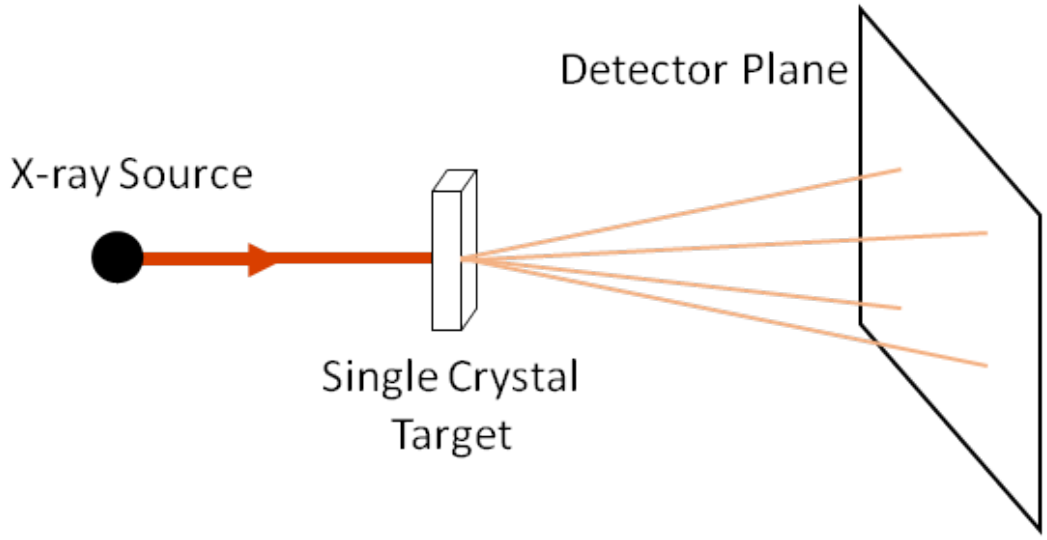


Figure 7: Schematic of Laue method.

In fact, the majority of commonly handled objects will be made of similarly multi-crystalline materials. This is due to the fact that, usually, special manufacturing techniques are required to make single crystal samples.

The x-ray source employed is monochromatic, similar to the divergent beam geometry. However the beam is now collimated similarly to the Laue method [61, 62].

Powder samples have a large number of randomly orientated grains, with each grain being a small single crystallite. The grain size affects the width of a diffraction pattern, as a smaller grain will have a broader diffraction pattern and vice versa. This is due to diffraction being a measure of long-range order and a smaller grain results in a more diffuse diffraction pattern.

In this way, the incident x-ray beam will very likely match the Laue condition with a number of crystallites in the sample. There is a degree of freedom here, where grains orientated around the axis of the input beam will lead to different scattered x-ray directions. When recorded on a flat detector, this produces diffraction rings often referred to Debye-Scherrer rings. Although if the sample

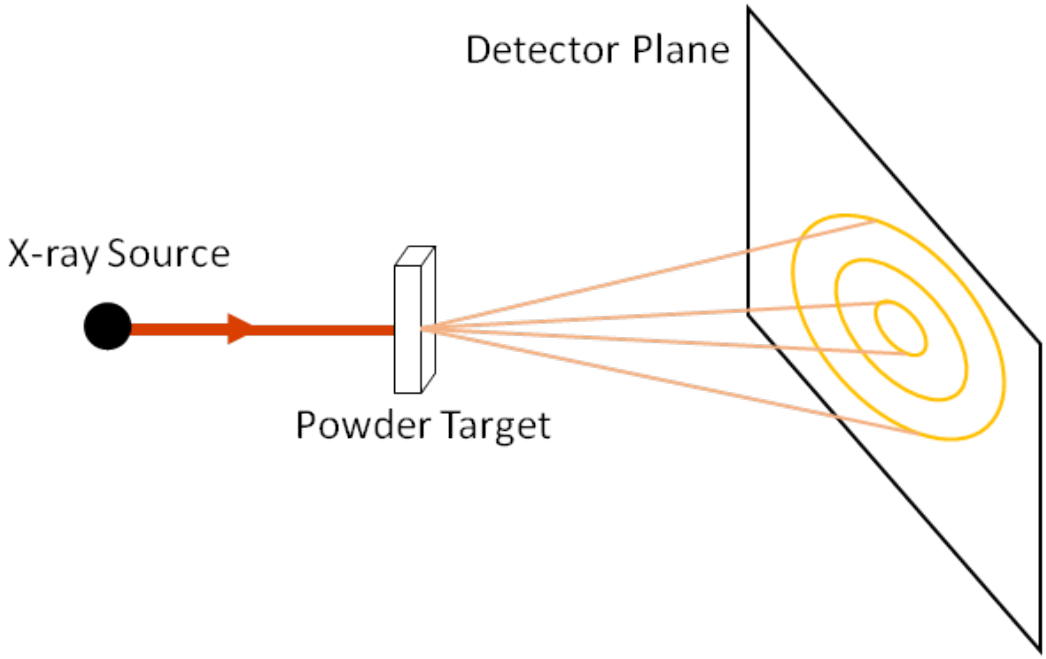


Figure 8: Schematic of Powder diffraction.

is textured, i.e. the distribution of grain orientations is incomplete, then these rings will also be incomplete.

2.3 SHOCK WAVES

A shock wave is defined as a propagating disturbance in a material. It is characterised by a discontinuity, called a shock front, in the pressure, density and internal energy of the material it is passing through [63]. They are exhibited as a steep front and require a uniaxial strain. The key requirement to create a shock in a material is that the velocity of the pulse increases with increasing pressure. This is given by:

$$\left(\frac{\partial^2 P}{\partial u^2}\right) > 0 \tag{30}$$

and the requirement that $|d\sigma/dV|$ increases with increasing σ which means that the material's compressibility decreases with increasing pressure.

In the work presented in this thesis, shock waves are used to compress samples, which are then probed using x-ray diffraction.

2.3.1 *Rankine-Hugoniot Conditions*

The Rankine-Hugoniot conditions describe the relationship between the states before, and after a shock has passed. Specifically it links the density, particle velocities, momentum and internal energies of the two states. They are derived using simple conservation of mass, momentum and energy arguments and are given in equations 31 to 33 [64–66].

$$\rho_0\, u_s = \rho_1(u_s - u_1) \tag{31}$$

$$p_1 - p_0 = \rho_1\, u_1\, (u_s - u_1) = \rho_0\, u_s\, u_1 \tag{32}$$

$$p_1\, u_1 = \rho_0\, u_s\, \left(\tfrac{1}{2}\, u_1^2 + e_1 - e_0\right) \tag{33}$$

where ρ is density, u and u_s are the particle and shock velocities respectively, p is the pressure and e is the specific internal energy. The subscripts refer to the initial and final states of the material, e.g. ρ_0 and ρ_1 refer to the initial and final densities respectively.

These equations assume a plane-parallel steady shock and no viscosity, heat conduction or any other form of energy transfer across the shock front including the effect of gravitational forces. The shock front is also assumed to be infinitesimally thin. The shear modulus is also assumed to be zero, there is no

elastic-plastic behaviour and that the material does not undergo phase transformations. Modifications to the jump conditions must be made in order to lift these assumptions.

High power laser experiments covered in this thesis enter the regimes of plasticity and polymorphic phase transitions. For both of these phenomena, the material can be modelled as multiple shocks/waves launched into the material. Shocks subsequent to the first shock must use the post-shock parameters of the immediately previous shock as initial conditions of the material rather than the static properties of the material.

2.3.2 *Shock Compressed Solids*

Unlike fluids, solids are able to support shear stresses. For a shock along the z-axis, this means that stress, and therefore strain, along the shock direction can be higher than orthogonal directions. This is due to a solid material not behaving like a fluid and being able to support a shear stress, this is discussed in more detail below. In addition, it is usually assumed that stress in directions perpendicular to the shock direction are equal to each other. Specifically this is quantified as $\epsilon_{33} \geqslant \epsilon_{11} = \epsilon_{22}$. This means that the strain tensor contains only diagonal elements and is described by only two strains; the longitudinal strain, ϵ_{33} and the transverse strain, ϵ_{11}. Note that these are directions with respect to the sample and shock, not the crystal lattice, these directions are indicated in Fig. 9.

2.3.2.1 *Hugoniot Elastic Limit*

The Hugoniot Elastic Limit (HEL) is the maximum uniaxial stress that can be supported by a solid given the stress and strain rate it is exposed to. When a shock reaches the HEL the wave profile and Pressure-Volume curve change to a shallower gradient due to the significant increase in compressibility once reached. Beyond the HEL a material response, beyond the relatively simple uniaxial compression, is required in order to be compressed further. In laser compression experiments, and for the experiments covered here, this is achieved by either the appearance of plastic behaviour or a polymorphic phase transition. Above the HEL the material loses its shear strength and behaves closer to a fluid and moves closer to a hydrostatic condition where $\sigma_{33} = \sigma_{11} = \sigma_{22}$. One way that this occurs, for some materials, is via plasticity where flow of material (typically via generation and movement of defects) can allow for the relief of shear stress.

2.3.2.2 *Shock Induced Phase Transformations*

Of particular interest in this thesis are polymorphic phase transitions. The best known polymorphic phase transition is the α to ϵ phase transition in iron [67]. Other examples include graphite to diamond which is one method of commercially producing diamonds. In such phase transformations, the structure of the material changes, typically to reduce the total shear stress of the material downstream of the shock. The work of Duvall and Graham covers this topic in detail and should be referred to for further reference [68].

Given the short timescales of shock experiments, the kinetics of the transitions can be important. Experimentally this means that the thickness of the sample material can affect the results. This is particularly relevant for Anti-

mony where there is an unusually large decay of transition stress with sample thickness [69].

It is also possible to induce chemical reactions or change the state of the material (melting or vaporisation) by the passage of a shock wave but this significantly beyond the scope of this thesis and is not relevant to the regimes investigated for this thesis.

The response of silicon to shock compression has been investigated for a number of years. Multiple gas-gun studies have shown that a multi-wave response is exhibited by the material. Whilst the first wave is easily associated with an elastic response. It is the following waves, and the mechanisms that cause them that are an open area of research.

Early work attributed the inelastic response to plasticity [70] or to a transition to a higher pressure phase [71]. Later work, some of which included measurements of structure using x-ray diffraction uncovered more about silicon's behaviour. Turneaure and Gupta (2007) found up to 23 % compression following the phase transition wave. Their other work of the same year [72] found smaller compressions than those measured by Loveridge-Smith [73] which is regarded as the benchmark piece of work on in-situ x-ray diffraction of silicon.

Loveridge-Smith used a divergent beam geometry and time-resolved x-ray diffraction to perform their measurements and observed what they call an 'anomalous' response of silicon. Turneaure and Gupta's later work of 2012 [74] also fails to observe the anomalous elastic response observed by Loveridge-Smith. Smith et al. (2012) performed work analysing only wave profiles and found both the strain rate and strength of the shock had a significant effect on the response of silicon [75]. They find that their observations are consistent with the Gilman plasticity model.

Work in 2004 observed a significant increase in conductivity at the HEL, which is consistent with a transition to the metallic β-Sn phase [76].

2.4 DIFFRACTION FROM STRAINED MATERIALS

For small amplitude shock waves, i.e those below the Hugoniot Elastic Limit (HEL), the material response is purely uniaxial and there will only be a longitudinal strain observed. Shock compressing materials beyond this limit will result in further changes in the material. In some cases the additional shear stress is relieved via a phase change; in others, plasticity will allow the material to return to a more hydrostatic state. For a poly-crystalline target in the Voigt limit, i.e. iso-strain, the strain state of all grains in the sample are identical and can be described by a single deformation tensor [77, 78]. Diffraction at different parts around the Debye-Scherrer ring will then give information about different parts of this strain state [62].

For arbitrarily strained samples, Higginbotham et al. have looked at how to extract the longitudinal and transverse strain, given measurements of the d-spacing from two independent scattering vectors [79, 80]. This is given in equation 34,

$$\left(\frac{d}{d_0}\right)^2 = \alpha_{11}^2(1-\cos^2\psi) + \alpha_{33}^2\cos^2\psi \tag{34}$$

where ψ is the angle between the scattering vector G_{hkl} and the shock direction, which is typically normal to the sample. Given measurements of d-spacing at two different values of ψ, the longitudinal and transverse strains can be calculated using:

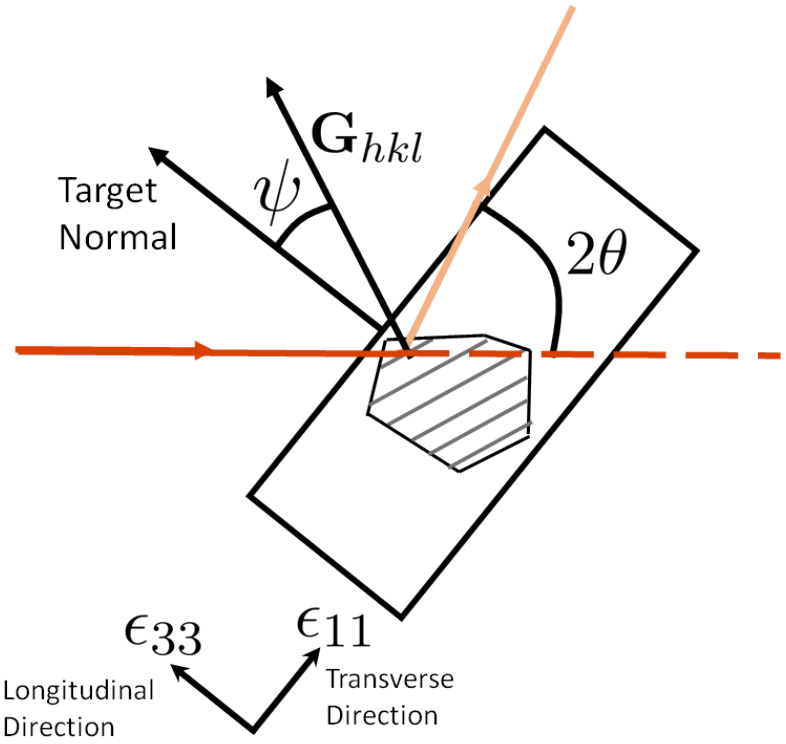


Figure 9: Schematic of diffraction from a grain within a strained powder sample. Angle between scattering vector and target normal, ψ, is highlighted. Also labelled are the longitudinal and transverse strain/stress directions with respect to the sample.

$$\epsilon_{33} = 1 - \sqrt{\frac{\left(\frac{d_b}{d_0}\right)^2 (1 - \cos^2 \psi_a) - \left(\frac{d_a}{d_0}\right)^2 (1 - \cos^2 \psi_b)}{\cos^2 \psi_b (1 - \cos^2 \psi_a) - \cos^2 \psi_a (1 - \cos^2 \psi_b)}} \tag{35}$$

$$\epsilon_{11} = 1 - \sqrt{\frac{\left(\frac{d_a}{d_0}\right)^2 \cos^2 \psi_b - \left(\frac{d_b}{d_0}\right)^2 \cos^2 \psi_a}{\cos^2 \psi_b (1 - \cos^2 \psi_a) - \cos^2 \psi_a (1 - \cos^2 \psi_b)}} \tag{36}$$

where the subscripts a and b indicate measurements of d-spacings from different detector positions.

2.5 LASER PLASMA INTERACTIONS

2.5.1 *Plasma Physics*

This section closely follows the book written by Salzmann, which should be referred to for a more thorough discussion [81].

A plasma is an electro-statically neutral collection of particles. It is comprised of electrons and ions. The electrons may be free, or bound to an ion. The average charge state, $\overline{Z}$, is given by:

$$\overline{Z} = \frac{\sum_{\zeta=0}^{Z} \zeta N_\zeta}{\sum_{\zeta=0}^{Z} N_\zeta} = \frac{n_e}{n_i} \tag{37}$$

where ζ is the charge of the ion, and N_ζ is the average partial density of a charge state ζ over the ensemble. n_e and n_i are the electron and ion number densities respectively.

The electron density can then simply be given as,

$$n_e = \overline{Z} n_i \tag{38}$$

Given the ion density, the average volume occupied by an ion can be modelled as a sphere. Therefore the ion sphere radius is given by,

$$R_i = \left(\frac{3}{4\pi n_i} \right)^{\frac{1}{3}} \tag{39}$$

which is also referred to as the Wigner-Seitz radius.

For hot plasmas at low electron densities (i.e exchange effects are negligible) and where the plasma evolution time is long compared to the electron thermalisation time then the Maxwell-Boltzmann distribution of energies and velocities can be used:

$$f_v(v)dv = n_e \left(\frac{m_e}{2\pi T_e} \right)^{3/2} 4\pi v^2 \exp\left(-\frac{mv^2}{2T_e} \right) dv \tag{40}$$

$$f_E(E)dE = \frac{2}{\sqrt{\pi}} n_e \left(\frac{E}{T_e} \right)^{1/2} \exp\left(-\frac{E}{T_e} \right) \frac{dE}{T_e} \tag{41}$$

with similar descriptions for the ions' properties.

A common concept in plasmas is the screening factor, $S(r)$, given by:

$$V(r) = \frac{Ze}{r} S(r) \tag{42}$$

where the screening factor represents the deviation of the screened potential of the ion from the standard Coulomb potential. At small distances, r, the screening factor tends to 1 (no difference from the Coulomb model) and at

large distances it tends to zero. This has the consequence that only a small number of neighbouring ions surrounding an ion have a non-negligible effect on it. There are a number of different models for the screening factor including the Debye-Hückel and Thomas-Fermi models. In the Debye-Hückel Model, the electric potential around an ion is described by:

$$\Delta^2 V(\mathbf{r}) = -4\pi e \left(\sum_{\zeta=0}^{Z} \zeta N_\zeta(\mathbf{r}) - n_e(\mathbf{r}) \right) \tag{43}$$

which leads to a screening factor of:

$$S(r) = e^{-r/D} \tag{44}$$

where D is the Debye screening length given by:

$$D = \sqrt{\frac{T}{4\pi e^2 n_i \left(\overline{Z^2} + \overline{Z} \right)}} \tag{45}$$

This model becomes inaccurate at small distances, therefore it performs poorly at high densities.

Ion sphere models are another form of ion model, which assume charge neutrality within the ion sphere. This results in the electrostatic field equalling zero at the ion sphere boundary and that there is effectively zero field from the ion beyond the sphere.

The Ion sphere model assumes that ions have Z_b bound electrons at $r = 0$ and Z_f free electrons in the surrounding sphere. The potential within the sphere is then:

$$V(r) = V_N(r) + V_{e,b}(r) + V_{e,f}(r) + V_{x,c}(r) \tag{46}$$

where V_N is the nuclear potential, $V_{e,b}$ is the potential due to the bound electrons, $V_{e,f}$ is due to the free electrons and $V_{x,c}$ is due to exchange interactions with the electrons.

The ion sphere model accurately treats the bound electrons with quantum mechanical models (either the Schrödinger or Dirac equations) using the potential described above. It does not assume the plasma consists of only one species.

Local thermodynamic equilibrium (LTE) occurs in plasmas where typical dimensions/size of the plasma are much smaller than the mean free path of photons emitted by the plasma. Also the collision length of the electrons and ions is significantly smaller than the plasma dimensions. As photons are able to travel a large distance before interacting with the plasma (if they do at all) and therefore are not necessarily in equilibrium with the electrons and ions. The short collision lengths and times of the electrons and ions mean that they are in equilibrium. Therefore he photons are described by a Planckian energy distribution whilst the electrons and ions remain described by Maxwell-Boltzmann distributions. The charge state distribution is then given by the Saha equation:

$$\frac{N_\zeta n_e}{N_{\zeta-1}} = 2\left(\frac{mc^2 T_e}{2\pi(\hbar c)^2}\right)^{3/2} \frac{z_\zeta(T_e)}{z_{\zeta-1}(T_e)} \exp\left(-\frac{E_{\zeta-1} - \Delta E_{\zeta-1}}{T_e}\right) \tag{47}$$

LTE assumes that charge state distribution follows the Saha equation and also that excited states follow a Boltzmann distribution. Outside of this, alternative methodologies must be used such as Coronal Equilibrium for low density plasmas or time dependent models where the plasma is rapidly evolving.

2.5.2 *Shock Wave Generation*

High Power lasers can be used to create a high pressure shockwave in a solid sample. This occurs due to ablation pressure generated by the irradiation of the sample by an intense laser pulse. Below $10^6\,\mathrm{W/cm^2}$ the absorption of laser energy results in evaporation of the sample material. This was first investigated in the 1960s by Ansimov and Ready [82, 83]. Inverse bremsstrahlung is responsible for this energy absorption.

The time-average kinetic energy of an electron which oscillates in the electric field of a laser is given by:

$$\overline{\frac{1}{2}m\dot{x}^2} = \frac{e^2E_0^2}{4m\omega^2} \tag{48}$$

The total energy (potential energy and kinetic energy) is twice this. As the electrons in the sample interact and collide with the nuclei their velocity along the laser polarisation direction becomes randomised. Therefore the energy associated with vibration by the electric field of the laser becomes randomised and is transferred to the thermal energy of both the electrons and nuclei (or ions in a plasma).

Beyond this laser intensity - above $10^9\,\mathrm{W/cm^2}$ a large fraction of the evaporated atoms may be ionised due the higher intensity laser and corresponding electric fields [84]. This is due to the evaporated atoms absorbing the laser energy and reaching extremely high pressures and temperatures. As a result, the plasma rapidly expands away from the sample and into the vacuum. By conservation of momentum this results in a high pressure on the sample. At a high enough laser intensity this can launch a shock wave into the sample. The ablation pressure scales with the laser intensity in this regime. This can be de-

rived using a simple analysis described by Fauquignon and Floux in 1970 whose analysis is followed here [85]. This analysis assumes the plasma has reached a steady state (specifically this means constant in time not space).

First it is assumed that the mass flux away from the surface of the sample is constant. Similarly we assume that the momentum flux is also constant. This gives:

$$\rho_a u_a = \rho_c u_c \tag{49}$$

$$P_a + \rho_a u_a^2 = P_c + \rho_c u_c^2 \tag{50}$$

where the subscripts a and c denote the ablation and critical surfaces respectively.

Finally we note that although internal energy, pressure and density change throughout the ablation plasma, total energy is still conserved with position. Therefore this is modelled as an isenthalpic process with the addition that kinetic energy of the plasma must also be included to correctly model the plasma. Finally there is a source of energy (the laser) which occurs as the critical surface. This energy is primarily absorbed near the critical density, due to the high plasma density and low group velocity of the light, and is transferred along the temperature gradient to the ablation surface by hot electrons. Therefore by considering the conservation of energy this gives:

$$\frac{1}{2}\rho_a u_a^3 + H_a \rho_a u_a + W = \frac{1}{2}\rho_c u_c^3 + H_c \rho_c u_c \tag{51}$$

where W is the laser energy absorbed per unit area. We also assume that the plasma behaves as an ideal gas and has its enthalpy can be described by:

$$H = \left(\frac{\gamma}{\gamma - 1}\right)\frac{P}{\rho} \tag{52}$$

where γ is the standard ratio of the heat capacities.

A further assumption is that the density at the ablation surface will be much higher than at the critical surface. The critical density is determined by the frequency of laser light and for a wavelength of 1 micron this will lead to a mass density of $\approx 2\times10^{-3}\,\mathrm{gcm}^{-3}$. This is significantly below the density at the ablation surface which will be closer to solid density.

We must also assume that the energy absorbed from the laser, W is the largest term on the LHS of equation 51. This can be assumed as at the ablation front $u_a \approx 0$, i.e. the material is stationary, and the dominant source of energy is the energy of the hot electrons carrying the absorbed laser energy.

The final assumption is that the velocity of the plasma at the critical surface is given by the sound velocity of the ions. Following the analysis of Fauquignon and Floux, we take the adiabatic speed of sound to give:

$$u_c = \left(\frac{\gamma P_c}{\rho_c}\right) \tag{53}$$

Thus we find:

$$W = \frac{1}{2}\rho_c u_c^3 + H_c\rho_c u_c \tag{54}$$

$$= \frac{\rho_c}{2}\left(\frac{\gamma P_c}{\rho_c}\right)^{3/2} + \left(\frac{\gamma}{\gamma-1}\right)P_c\left(\frac{\gamma P_c}{\rho_c}\right)^{1/2} \tag{55}$$

$$= \frac{1}{\sqrt{\rho_c}}P_c^{3/2}\sqrt{\gamma}\left(\frac{\gamma}{2} + \frac{1}{\gamma-1}\right) \tag{56}$$

which can be rearranged to give:

$$P_c \approx 2\rho_c^{1/3} W^{2/3} \tag{57}$$

The ablation pressure can then be given by:

$$P_a = P_c + \rho_c u_c^2 \tag{58}$$

$$= (1+\gamma)P_c = \frac{8}{3}P_c \tag{59}$$

$$= \frac{16}{3}\rho_c^{1/3} W^{2/3} \tag{60}$$

If we assume that the ablated material has approximately equal protons and neutrons, which is typical for light elements in the ablators used in the experimental work of this thesis, then:

$$\rho_c = 2 n_c m_p \tag{61}$$

Using the standard definition of the plasma frequency, then the ablation pressure is given by:

$$P_a = \frac{16}{3}\left(\frac{2\epsilon_0 m_c m_p \omega^2}{e^2}\right)^{1/3} W^{2/3} \tag{62}$$

2.5.3 *X-ray Generation*

A key experimental tool used in many high power laser experiments is an in-situ x-ray backlighter which provides a high intensity source of x-rays over the short timescale of the experiment. A similar process of inverse bremsstrahlung occurs where laser energy is deposited into the ablation plasma which reaches a

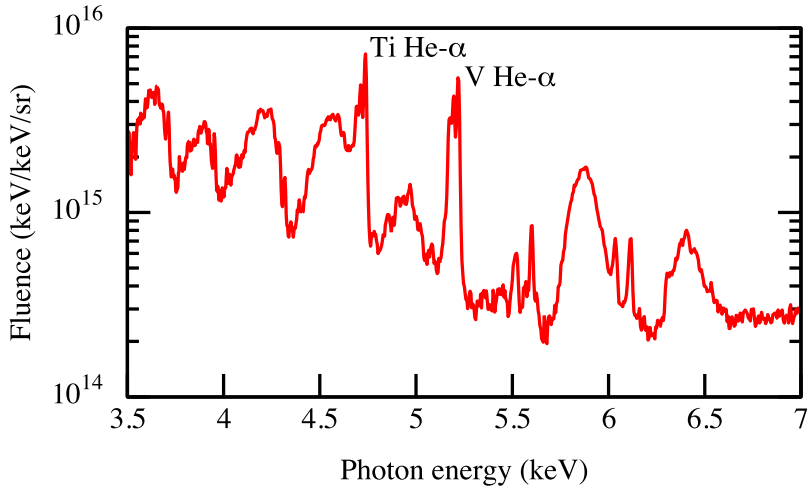


Figure 10: Typical x-ray emission spectrum from a mixed metal backlighter. Used with permission from Suggit et al. [59].

steady state. Matthews et al. review a large range of x-ray backlighter sources, covering a variety of both emission energy and laser parameters [86]

At high laser intensities, in this thesis intensities of around $10^{14}\,\mathrm{Wcm}^{-2}$, the plasma becomes highly ionised. This is due to the extremely high electron temperatures which allow ionisation of inner electron shells (i.e. beyond those just the outer shell) even for high Z elements.

Once shells have been ionised, up to forming H and He like ions, electronic transitions within the ion result in emission along characteristic lines. Typically these will be from electrons in the shell above the vacancy which will fall to a lower energy level. This results in the emission of a photon, and for a highly ionised ion this will be in the x-ray energy range.

For the mixed metal backlighters used in thesis. They were developed by Suggit et al. and are discussed in detail in [59]. A typical emission spectrum from a mixed metal backlighter is given in Fig. 10. Such spectra are typically recorded by a flat crystal spectrometer and recorded by image plate or a CCD.

3

SINGLE PHOTON ENERGY DISPERSIVE X-RAY DIFFRACTION (SPEDX)

3.1 INTRODUCTION

Advances in high power lasers are enabling solid matter to be driven to increasingly extreme states, reaching pressures unattainable by static compression [30, 42]. Generating these states of matter allows us to probe the conditions within planetary interiors, and to study the initial stages of an inertial confinement fusion implosion [87, 88].

Laser-driven shock or quasi-isentropic compression techniques not only generate extreme conditions in the sample, but also create an extremely harsh environment within the target chamber; which poses a significant challenge for diagnostics to gather high quality data [44, 89]. Even for relatively small pressures (tens of GPa) image plate based techniques require filtering to prevent noise from overpowering the diffraction signal. The issue is exacerbated when laser intensity is increased due to the rise in average energy of the x-ray noise. Additionally the diffraction signal intensity from shock compressed targets is reduced by effects such as increased temperature and highly disordered material behind the shock front.

An additional source of noise is x-ray fluorescence from the sample, which is a result of photoionization of core electron shells in the sample material by x-

rays from the backlighter. Careful choice of both sample and filtering material can mitigate this.

At the NIF, there is the additional issue of unconverted light (albeit unfocused) also being delivered to the target chamber; creating significant difficulties with the survival of diagnostics positioned close to the target, and any data recorded on them.

To overcome these difficulties, **S**ingle **P**hoton **E**nergy **D**ispersive **X**-ray diffraction (SPEDX) has been developed [51]. This technique uses the combination of a white-light x-ray source and one or more CCDs operated in single photon counting mode. This records both the position and energy of incident x-rays simultaneously. The high sensitivity of CCDs suits them to being used in this way, as they can be placed significant distances away from the interaction region, yet still be able to measure low signals (due to detectors being placed far away from the interaction region) and tell signal photons from noise photons.

For the work presented here, the quasi-white light (broadband) x-ray source was generated using a mixed metal foil, which had originally been developed as an x-ray source for white light Laue experiments [59, 90]. The foil is comprised of layered mid to high Z elements. When irradiated by laser light, reaching an intensity of $10^{14}\,\mathrm{Wcm}^{-2}$, they emit their M and L shell lines that are unresolved due to the large number of elements present. An alternative white-light source, such as an implosion capsule backlighter would produce a smoother and brighter spectrum; however they are only available on the largest laser facilities such as Omega or the NIF due to their spherical drive symmetry [91, 92].

Larger laser facilities such as the NIF, Omega and Orion all have automatic (or similar) alignment systems, where positioning and design of diagnostics are tightly constrained. Whilst this can limit the flexibility of such facilities,

there is a significant benefit gained from the highly accurate and reproducible alignment of diagnostics. In the context of SPEDX, this can mean the scattering angle of the CCD is well defined in advance of the experiment. Therefore no post-experiment fitting would be required, as is usually required at smaller laser facilities, especially when using image plate based techniques.

The energy dispersive capability of a CCD allows a single CCD to distinguish diffraction from different lattice planes despite subtending a small range of Bragg angles. The Ewald sphere is a geometric construct widely used in many diffraction contexts to show the relationship between scattering vectors, diffraction angles and the reciprocal lattice as described in Warren chap. 2 [93].

This is shown in figure 11 where the blue dashed line indicates the range of scattering vectors a single camera is sensitive to. The intersection of this line with multiple lattice spacing rings indicates how a single camera can measure diffraction from a number of different lattice spacings.

There is a correlation between scattering angle and x-ray energy, which noise processes do not possess as they are expected to be isotropic, and therefore have no relationship between energy and position. This can be exploited, either by utilising multiple CCD positions with different Bragg angles, or by quantifying the correlation between incident photon energy and position on the CCD, as each pixel lies at a different Bragg angle.

Whilst using these approaches will mitigate the effect of noise on a SPEDX experiment, significant numbers of noise photons at the *same* energy as diffraction signal on the CCD significantly reduces data quality, as diffraction signal becomes indistinguishable from noise. Care must be taken to avoid this wherever possible.

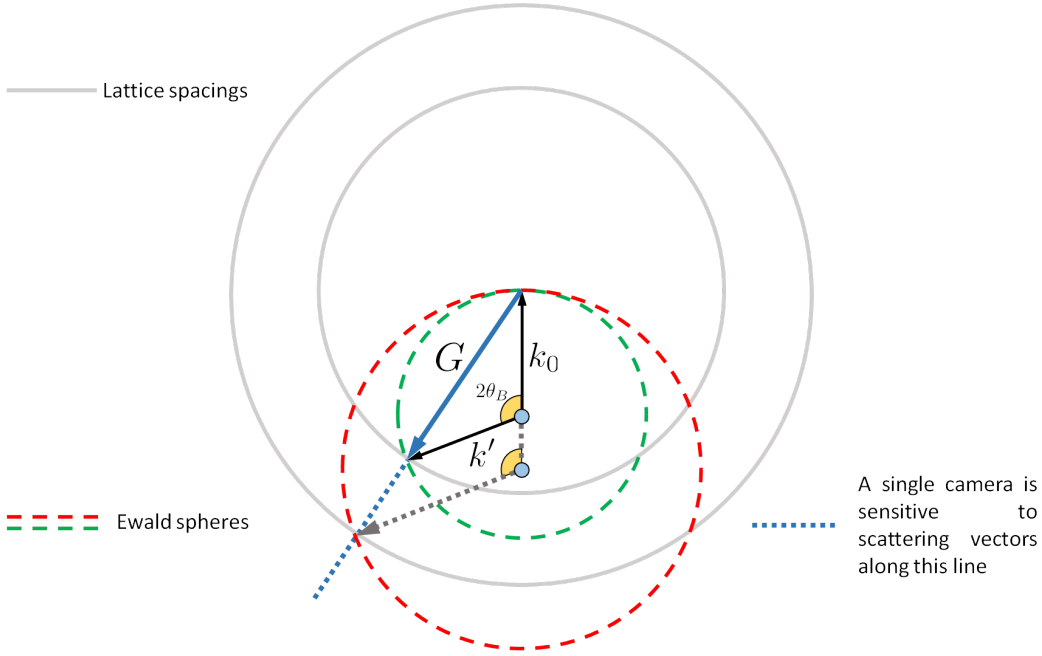


Figure 11: The Ewald construction of x-ray diffraction appropriate for SPEDX. The dashed circles represent two distinct wavelengths that will diffract from the available lattice planes (drawn in solid grey). A single camera, here subtending a single Bragg angle, is sensitive to scattering vectors along the blue dashed line. The range of reciprocal space that this camera can probe is limited by the range of wavelengths available.

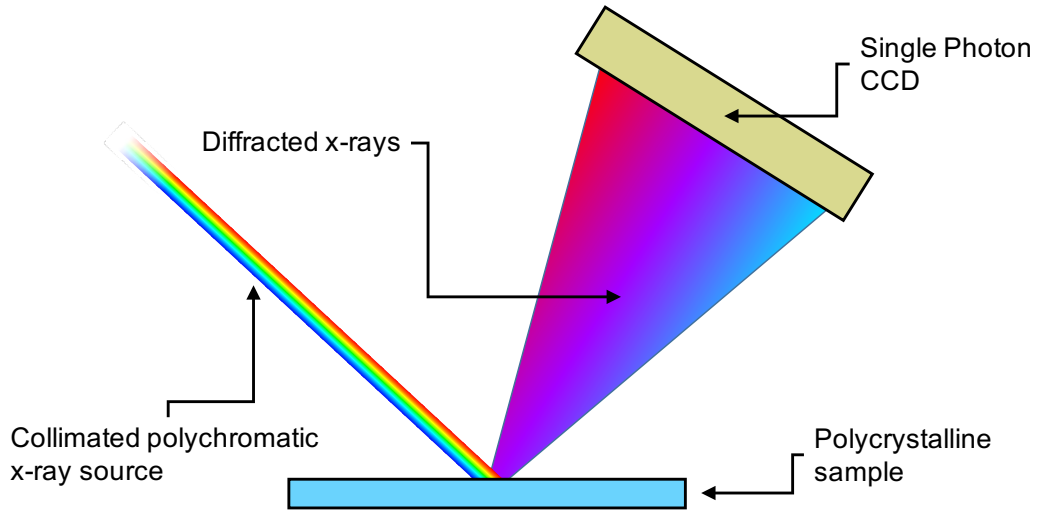


Figure 12: From a polycrystalline target, a white light x-ray beam will diffract at a range of energies and Bragg angles, via a set of diffracting planes. Each position on the CCD will therefore have a different Bragg angle for a tightly collimated backlighter beam. The range in colours at each position of the CCD in the diagram indicates the dispersion direction, where red indicates longer wavelengths than blue.

3.2 SINGLE PHOTON CCD

A key requirement of single photon counting mode is that the photon flux is low enough such that only around 1 % of pixels receive a photon. This is achieved by a combination of suitable filtering and placing the CCD a significant distance (tens of cm or more) away from the target; this in particular makes the technique ideally suited for the NIF where survival of diagnostics is a challenge.

Increasing the distance between target and detector also has the added advantage of increasing signal to noise. The flux of noise photons will be reduced by a factor of R^2; whilst diffraction signal is constrained to diffraction rings where the signal will be reduced by a factor of $R/\cos(2\theta_B)$. The intrinsic sensitivity of CCDs (the probability of absorbing an x-ray between 3 - 9 keV peaks at

80 %) allows them to detect very low signals whilst image plate based detection methods have a much lower sensitivity in the single photon regime [94, 95].

CCDs operate by the incident photon being absorbed by the semiconductor substrate, usually silicon for commercially available CCDs. This generates a large number of free electrons via photoionisation within a depletion region of the substrate, followed by the resulting charge cloud being accelerated towards the gates which collect the charge [96]. The charge is amplified and measured giving an integer value at each pixel. Calibration is required in order to match the measured charge to an x-ray energy, due to differences in the readout electronics between different CCDs. The conversion from the integer values outputted by the camera to x-ray energy was found to be linear between 3 and 9 keV for the CCDs used in this work. This was done by measuring energies of known emission lines across this energy range which both confirmed the linearity and calibrated the CCD.

There is a readout noise, r, of a few (typically < 5 for a cooled CCD) electrons, in addition to Poisson noise associated with the production of the charge cloud by the x-ray. Therefore the FWHM uncertainty of the energy measurement of any individual x-ray is given by [97],

$$\Delta E_{FWHM} = 2.35\omega\sqrt{r^2 + FE/\omega} \tag{63}$$

where ω is the average energy required to create an electron-hole pair in the CCD substrate, E is the energy of the x-ray and F is the Fano factor, 0.117 for silicon. The Fano factor reduces the uncertainty due to the constraint that the x-ray must deposit all its energy in the substrate [98]. For silicon, ω is 3.65 eV which corresponds to the direct band gap of silicon. As seen from figure 13 the energy resolution of a silicon substrate CCD is intrinsically poor compared to

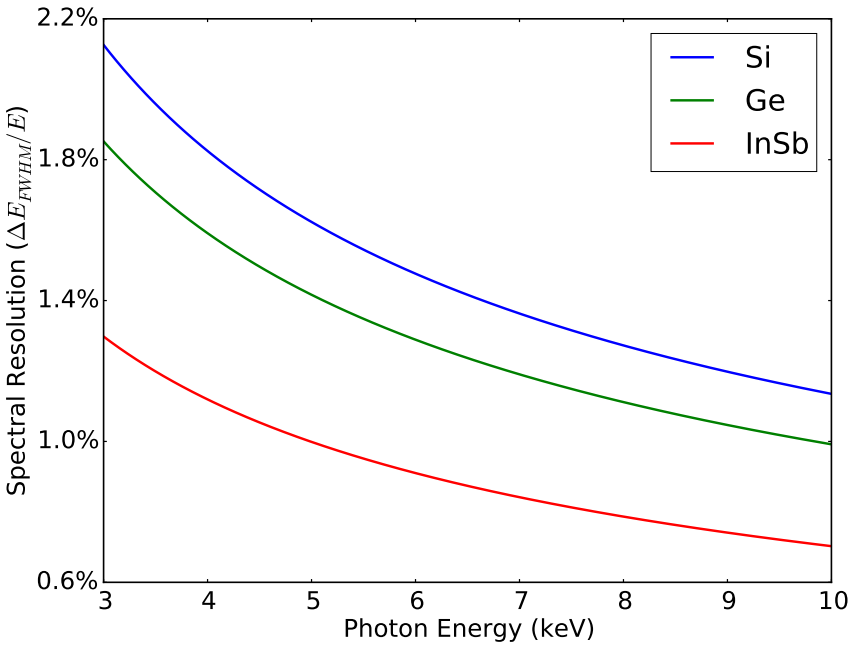


Figure 13: Intrinsic spectral resolution ($\Delta E_{FWHM}/E$) for a CCD in single photon mode for several detector substrates. The electron-hole pair energies are taken from Devanathan el al. [99] and the Fano factors are taken from Papp et al. [100].

crystal spectrometers, which means that a large number of photons are required to perform accurate measurements. This figure is representative of the energy resolution achieved by the CCDs in this experiment.

Designing experiments to perform diffraction at higher energies, with the use of a high energy x-ray source would increase the spectral resolution; although the quantum efficiency of the CCD, the probability of an x-ray being absorbed, at energies above 9 keV rapidly decreases, requiring the x-ray source to be brighter as a consequence. Using higher Z substrates can both increase this efficiency and improve spectral resolution, however such devices are not commercially available.

CCDs have been used in laser-plasma experiments for a number of years [101, 102] to perform spectroscopic measurements, however SPEDX is the first use of CCDs to perform *in-situ* x-ray diffraction. These previous uses of CCDs have

taken a histogram of every pixel in the array and have fit a background and signal to it. This method includes events where the charge cloud created from the absorption of a single photon has been collected by more than one pixel. Additionally, if these 'pixel bleeding' events occur in a pixel next to a single pixel event, then this will change the inferred photon energy of the event. Pixel bleeding alone creates a low energy tail along with extra counts at very low energies. The 'contamination' of single pixel events by pixel bleeding increases the apparent energy of the single pixel event. These two scenarios significantly increase the width of any peaks in the final spectrum measured by the CCD.

A key improvement made in this work is the use of an algorithm to separate single photon events from events where there is pixel bleeding; resulting in a substantial increase of the signal to noise ratio of the spectra measured by the CCD [103, 104].

The algorithm searches for pixels where the measured number of counts is higher than a predetermined threshold. Upon finding any such pixels, all neighbouring pixels are also checked for counts above the threshold. The threshold was chosen in order to optimise the signal to noise ratio of measurements and was found to be $\approx 2\,\%$ of a typical single photon event.

When a hot pixel is adjacent to another, it is assumed that some degree of pixel bleeding has occurred, although it is possible two x-rays have been absorbed in each pixel, and it is not included in the final single photon event spectrum. This is equivalent to only using grade 0 events in the ACIS grading system, a widely used classification scheme in the astrophysics community for x-ray CCDs [105].

Expanding the event search to multi-pixel events results in a significant increase in the width of peaks, increasing the standard deviation of a peak by a

factor of approximately 1.5, whilst having no effect on the peak position and therefore only single pixel events are considered.

3.3 FIRST DEMONSTRATION - JANUS 2012

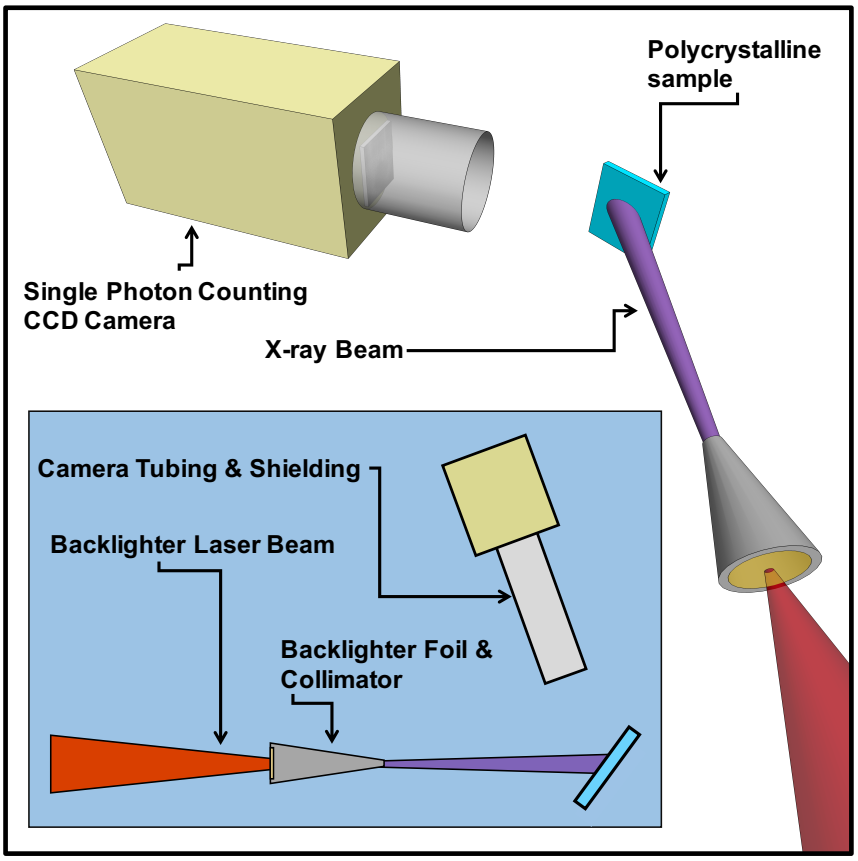


Figure 14: Diagram of Janus 2012 Experiment, not to scale due to large differences in relative sizes of various experimental components. Inset: Plan view of experiment. Colours are consistent between inset diagram and 3D view for labelling purposes.

The first demonstration of the SPEDX technique was performed using the Janus laser at the Jupiter Laser Facility within the Lawrence Livermore National Laboratory [51]. Two 2 ns laser pulses of 527 nm light delivered a total of 350 J to the mixed metal foil backlighters, using temporally square pulse

shapes. The pulses were timed to be simultaneous but were spatially separated by approximately 150 µm and individually focussed so that each laser spot reached $10^{14}\,\mathrm{Wcm}^{-2}$ at the surface of the foil backlighters. In order to observe diffraction at different Bragg angles, the backlighter position could be adjusted to change the scattering angle, $2\theta_B$.

The x-rays were collimated by a steel barrel, to give a divergence of 100 mrad at the sample. In this experiment the samples were 25 µm thick V and Ta polycrystalline foils. Vanadium was chosen as it has fluorescence lines at energies within the range of the backlighter spectrum, which are useful for performing a calibration of the CCD. The relatively high scattering efficiency of tantalum meant that it was well suited to demonstrate diffraction.

A single Princeton Instruments MTE camera positioned outside the target chamber, approximately 55 cm from the target was used to detect x-rays. A steel tube was used to restrict the field of view of the CCD cameras to only the samples. This minimised the exposure of the CCD to noise sources, such as incoherent scatter of x-rays by the target chamber, which do not originate from the sample. Two 3 mm thick Be windows were also used to filter out optical and other low energy photons. A Diagram of the experiment is shown in Fig. 14.

The CCD was operated at -30 °C and water cooled to reduce the number of dark counts generated; the slowest readout mode was used to minimise readout noise, r, to 2. The Princeton MTE cameras are rear-illuminated thinned CCDs, which minimise the spatial size of the charge cloud; therefore reducing the degree of pixel bleeding.

The spectra measured from two different shots, where the Bragg angle has been changed by 1.5°, using tantalum samples are shown in Fig. 15 along with a moving window average.

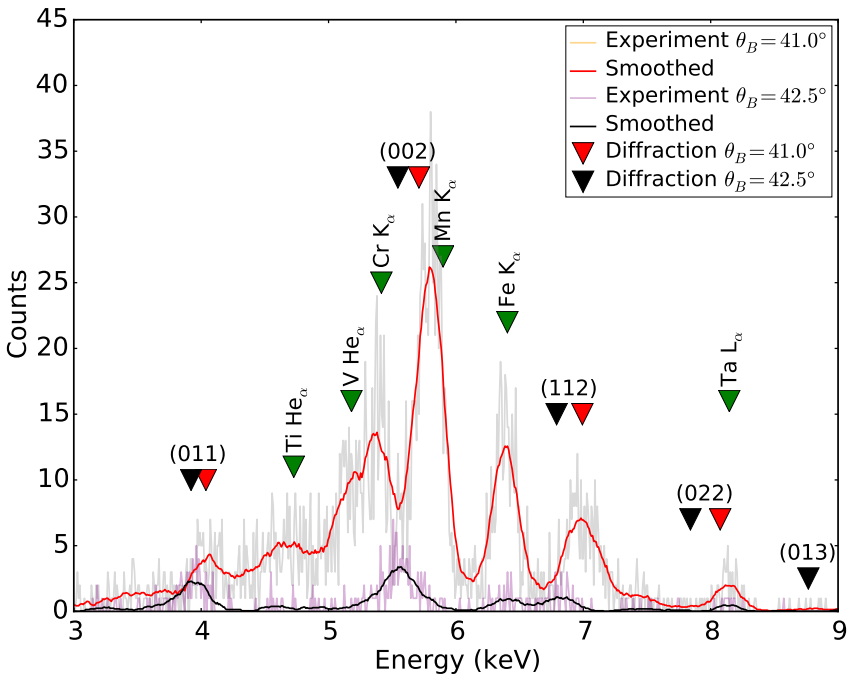


Figure 15: Spectra measured from separate shots with tantalum samples where the scattering angle has been changed between shots. The expected position of diffraction peaks has been indicated along with relevant spectral lines.

There are a number of differences between the two spectra, however there is a clear shift in the position of the diffraction peaks which is consistent with the indicated change in Bragg angle. Note that the difference in Bragg angle (although not the absolute value of the Bragg angle itself) between shots was accurately measured during the experiment, and is not a fit from the data. This increases the confidence that these peaks are a result of diffraction. The peak above 8 keV does not shift position between shots and it has been interpreted as being due to tantalum L_α fluorescence rather than diffraction. This is not unexpected as the backlighter is weak at these higher energies and therefore there is unlikely to be significant diffraction at this energy. Conversely *all* photons above the tantalum L edge will contribute to the L_α fluorescence, and as a result it appears in the measured spectra.

The shot at $\theta_B = 41.0°$ has more lines present than the shot at the higher Bragg angle, in addition to being significantly brighter. The position of spectral lines has been indicated in Fig. 15, where the elements are either present in the backlighter or the steel tube that was used to restrict the field of view. He_α lines are believed to come from the backlighter whilst K_α lines are from fluorescence of the experimental apparatus. The fact that the backlighter was significantly brighter for this shot, confirmed by a separate crystal spectrometer directly measuring it, would explain the presence of significantly more noise. Moreover, for a separate shot where a copper backlighter was used, He_α emission was measured; indicating that strong lines from the backlighter can be detected by the CCD and seeing them in Fig. 15 is not surprising. A representative backlighter spectrum is given in Section 2.5.3.

The (002) diffraction peak of the brighter of the two shots appears to be at the incorrect energy for the indicated Bragg angle. The most likely reason for this is the presence of a large number of Mn K_α photons, an element present in the steel tube used to restrict the field of view of the CCD, thereby moving it away from the expected position. This shows that spectral overlap of noise and diffraction signal can lead to significant difficulties when analysing the results of SPEDX experiments, and care must be taken to avoid this in future experiments.

3.4 DRIVEN SPEDX - VULCAN 2013

In order to demonstrate the SPEDX technique on laser driven targets, an experiment was performed at the Rutherford Appleton Laboratory. In addition to laser driven targets, the experiment also utilised multi-target mounts and

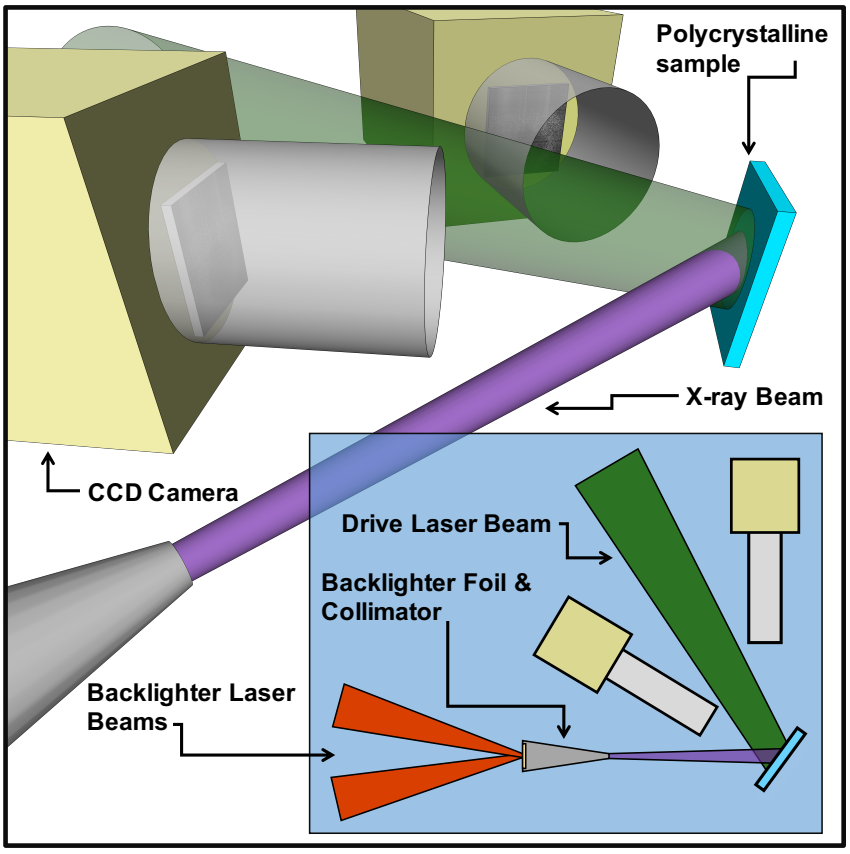


Figure 16: Diagram of Vulcan 2013 Experiment, not to scale due to large differences in relative sizes of various experimental components. Inset: Plan view of experiment. Colours are consistent between inset diagram and 3D view for labelling purposes.

remote alignment to significantly increase the shot rate, thereby reducing the need to cycle the target chamber between each shot [106].

The experiment was performed using the Vulcan laser in Target Area West. Six beams were co-timed to deliver up to 600 J of frequency doubled 532 nm laser light to the mixed metal backlighter target in 1 - 2.5 ns. The beams were defocused to a spot size ≈100 µm to generate intensities of 10^{14} Wcm^{-2} in a similar fashion to the previous experiment. The backlighters for this experiment used a modified mixture of elements so that the large noise peaks present in the previous SPEDX experiment, attributed to incoherent scatter from the backlighter, would not be present again. Specifically this makes the backlighter

made of 300 nm layers of Pd, Ag, Sn, Sm, CsI coated onto the same 10 µm plastic film.

The x-rays were collimated to limit the x-ray spot size to $\approx 0.5\,\mathrm{mm}^2$ in a similar fashion to the previous SPEDX experiment. Constraining the size of the x-ray spot ensures that it is smaller than the drive spot, which ensures that diffraction is only observed from the driven region of the sample. A further improvement in this campaign was the use of a molybdenum collimator which is significantly thicker than the previous steel design. The characteristic fluorescence lines of molybdenum are also outside of the energy range of interest for this experiment. Therefore they were not expected to appear in the measured spectra.

A long pulse beam was used to deliver 10 - 80 J over 3 - 8 ns, using square pulse shapes with rise times of order 10 ps, to shock compress the metal foil samples. Random phase plates were used to provide uniform drive intensity over the drive spot. The minimum area of the drive spot was $1\,\mathrm{mm}^2$ which could be defocused to reduce drive intensity. This achieves an intensity of up to 10^{12} Wcm^{-2} and a drive pressure of up to 60 GPa [67]. There were two different long pulse beams available; their use was alternated in order to increase the shot rate of the experiment.

A range of delays between the drive and backlighter beams were used in order to probe the target material at different stages of its compression. The two sets of beams, i.e. the backlighter and drive beams, were co-timed during setup using a fast diode such that the delay was accurate to 0.5 ns.

The sample materials were 30 µm polycrystalline metal foils of tantalum coated with 10 µm of parylene-N plastic as an ablator and an aluminium flash layer 5 nm thick.

Two Princeton MTE x-ray CCD cameras were used during the experiment to collect x-rays at different Bragg angles and were placed 50 - 70 cm away from the target. The cameras were again operated at −30°C in order to minimise the number of dark counts accumulated by the CCDs.

The use of two cameras at different angles allows for determination of the strain state of the compressed material along two different reciprocal lattice directions. This allows the transverse and longitudinal strain in the material to be inferred and therefore an estimate of residual strength to be made [79].

Note that during the experiment, the camera positions were altered along with target angle, relative to the x-ray beam. Therefore the cameras did not have consistent values of ψ (the angle between the shock direction and the scattering vector), nor was one camera always more sensitive to longitudinal (or transverse) strain. The cameras' ψ values were recorded in detail so the analysis was not impaired by this. The values of ψ ranged from 29 to -19.3° and the maximum difference between the two cameras for any shot was 12.7°.

Thick aluminium tubes, several mm thick, were used to restrict the field of view of the CCD to the samples. Aluminium was chosen to minimise the impact of noise photons from the tubes, which was a significant issue with the steel tube used previously. A 100 µm filter of PETP plastic was placed at the end of the shielding tubes to reduce the number of low-energy x-rays collected from drive noise, which can lead to the CCD no longer being in the single-photon regime.

The tubes and cameras were also covered by a large amount of lead shielding to minimise the number of stray photons from the backlighter being recorded on the CCD. A diagram of the experimental setup is shown in Fig. 16.

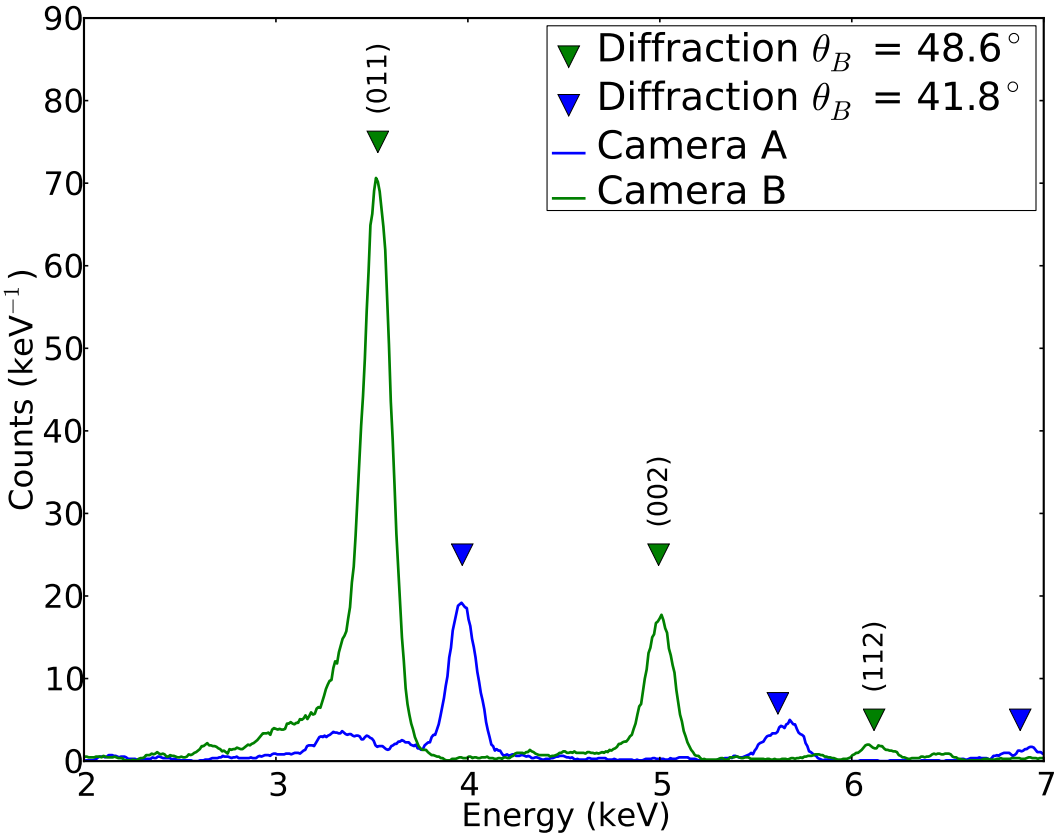


Figure 17: Spectra measured from an undriven tantalum target recorded by two different CCD cameras simultaneously. The smoothed spectra have been plotted and the expected positions for diffraction signal, given the indicated Bragg angles, have been indicated.

Mounting the targets on pinwheels allowed for multiple shots to be taken in succession, without the need for replacing targets every shot and subsequently cycling the target chamber vacuum; therefore providing a significant increase in shot rate. Due to being the only Vulcan users during the experiment it was also possible to interleave the use of beams to further increase the shot rate up to a maximum of shooting once every 10 minutes.

Spectra from a single shot for an undriven target are shown in Fig. 17. The improvements made to this experiment resulted in a significant increase in signal to noise of the measured spectra, which is clearly evident when compared to the results from the previous experiment shown in Fig. 15. In particular the

signal to noise ratio is higher and there are no significant lines from fluorescence or the backlighter, such as the titanium and vanadium lines seen previously. In part this is due to having a brighter backlighter. This was possible due to the Vulcan laser's larger size, where almost double the laser energy is available compared to Janus. Using plastic capsule implosions as an x-ray source would likely give a corresponding increase in data quality, due to their increased brightness over mixed metal foils.

The spectra shown in Fig. 17 are typical for all undriven shots during the experiment, where the (011) diffraction peaks at 3.5 - 4 keV is brightest due to the backlighter spectrum being brightest at that energy.

The results from a single shot with a driven tantalum sample is shown in Fig. 18 along with comparison to an undriven sample. The spectra have been converted to d-spacing using the Bragg angles of the individual cameras, which have been determined from previous shots using undriven samples.

Both cameras measure a small shift to a smaller d-spacing indicating compressive strains of 2.7 ± 0.6 and 1.5 ± 0.8 % for cameras A and B respectively. These compressions indicate a pressure of approximately 20 GPa. The different compressive strains measured on the two cameras indicate that the tantalum is in a non-hydrostatic condition, i.e. exhibits some degree of residual strength. If the material was hydrostatic, both cameras would measure the same d-spacing regardless of their position.

As the angle of the target, therefore the shock direction, is known relative to the incoming x-ray direction, then the longitudinal and transverse strains can be inferred. However, it was found for many shots throughout the campaign, when these two strains were calculated, that there was a higher transverse than longitudinal strain. That is to say the sample was found to be more compressed

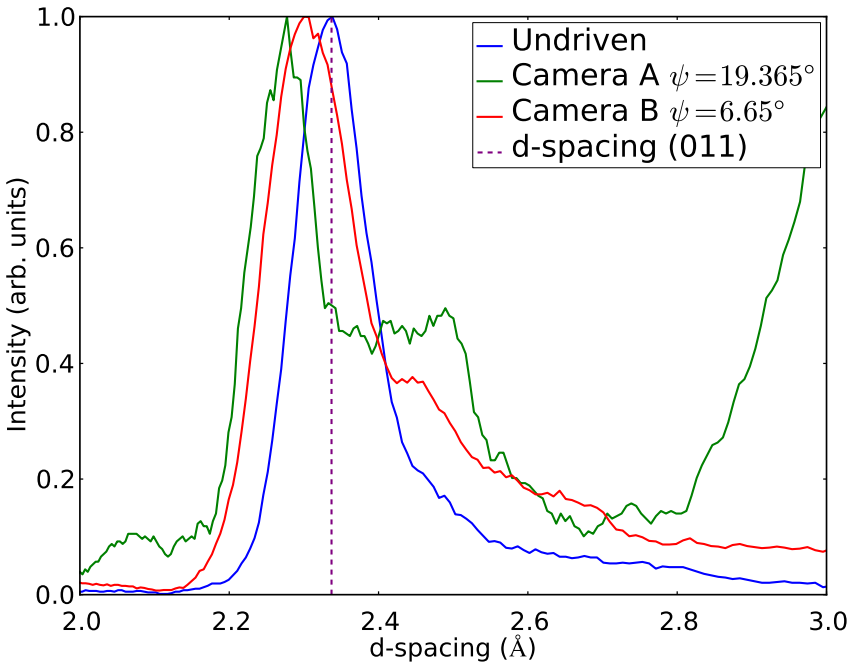


Figure 18: Diffraction pattern from a driven tantalum sample. The undriven pattern, taken from a separate shot, is shown for comparison. The high intensity by Camera A at ≈ 2.5 Å is due to low energy drive noise.

in directions perpendicular to the shock direction than along it. Furthermore for a small number of shots it was found that there was a negative transverse strain, i.e. expansion, along with a compressive longitudinal strain. The shot shown in Fig. 18 happens to be one such shot. Before analysis there is no simple way of identifying this unusual strain state from the diffraction pattern alone. Additionally, for some shots the strain could not be inferred at all. This is due to the expression within the square roots in equations 35 and 36 evaluating as negative.

These results are particularly surprising, as they are not consistent with typical material responses to compression, via a shock or otherwise. At the pressures reached in this experiment, tens of GPa, the material response is expected to be mediated by plasticity and described by a diagonal strain tensor. This model would suggest some degree of strain anisotropy, with a higher

longitudinal than transverse strain, although the sample being in a hydrostatic state would not be an unsurprising material response.

Strain gradients are unlikely to be the cause of the unusual measurements as this would be observed as significant broadening of the diffraction peaks. In addition, the use of an ablator and square drive pulses were specifically used to avoid significant strain gradients. The rise times of the drive pulses were of the order of tens of picoseconds at most. The backlighter delays and short absorption length of 3 - 9 keV x-rays in tantalum, less than 6 µm, also reduce the experiment's sensitivity to any strain gradients.

A more likely explanation of these results is due to the positioning of the cameras and uncertainty in the measurements. Whilst the two cameras do differ in scattering angle; the difference in ψ, the angle between reciprocal lattice vector and shock direction, between the two cameras is small. Whilst ψ was varied by rotating the sample and changing the camera position, the largest difference in ψ during the experiment between the two cameras was 12.7°. Moreover both CCDs were both sensitive to mostly longitudinal strain with the largest value of ψ during the experiment being 29°.

The combination of small strain anisotropy, which is expected at these pressures [107], along with the impact of uncertainty in the measurements could lead to misinterpretation of the results as showing unusual strain states. As seen in Fig. 18 the driven peaks are only just resolvable from the undriven peak. The previous SPEDX campaign showed that the presence of noise peaks can shift the apparent position of a diffraction peak, and here a small shift in peak position could lead to inferring unusual strain anisotropies.

The fact that for some shots a transverse expansion is observed, something that is physically very unfeasible when there is also a longitudinal compression,

indicates that this is a more likely explanation than the tantalum being in such an unusual strain state.

Wehrenberg et al. (2015) report a relaxation of shear stress in tantalum in approximately 1 ns [107]. Their work is for higher pressure conditions (50 GPa and above) and so longer relaxation times are expected for the lower pressures reached here. However as the cameras are highly sensitive to longitudinal strains, and with the largest strain measured by either camera during the experiment being 5.0 % i.e. much smaller than the strain anisotropies observed by Wehrenberg et al.; it is most likely that only the relaxed final state was observed during the experiment and not any early states with a large uniaxial strain. The long x-ray pulse time, 1 - 2.5 ns, joined with the short lived uniaxially compressed state favours this interpretation i.e. the tantalum is (or is close to) hydrostatic and uncertainties in measurements of compression have lead to the unusual estimations of strain anisotropy.

Possible sources of uncertainties could be noise photons or sharp changes in the backlighter spectrum, which are both known to occur. Although it is not clear what the source of these noise photons would be in this experiment, at these energies, it can not be ruled out.

Clearly for future experiments there need to be improvements made to allow for measurements of residual shear strength and strain anisotropy. One such improvement would be to choose a more suitable combination of camera positions and target angles, such that the ψ of the two cameras is significantly different. This can potentially be achieved by placing one camera in transmission which also has the added advantage of making it significantly less sensitive to drive noise. However diffraction signal can be significantly weaker in transmission, particularly for high Z materials; therefore a brighter and higher energy back-

lighter would be highly advantageous. Optimising the experiment for diffraction at higher energies brings other advantages, such as allowing for more filtering. This was an issue for this experiment where excessive drive noise was close to overwhelming the CCD and taking it out of the single photon regime. An alternative scheme for performing diffraction at higher energies is by using smaller scattering angles, such that the diffraction peaks will be observed at higher energies where there is both better energy resolution and the absolute shift in energy for the same strain is higher.

Alternatively, placing CCDs at the same scattering angle but at different azimuthal angles around the Debye-Sherrer ring would also result in the two cameras positions having different values of ψ.

SPEDX would be well suited to experiments in which there are significant changes in crystal symmetry under compression, since the appearance of new peaks are a clear and distinct signal compared to shifting of peaks which, as shown, can be challenging. Materials such as iron, which undergo a phase transition under compression, would be suitable to demonstrate this.

Using materials which exhibit high strain anisotropy, such as silicon below its HEL [73], would also be materials where using SPEDX could be advantageous.

3.5 SIMULATIONS

In order to support the analysis of this technique, a Monte Carlo ray-tracing code was developed to simulate diffraction and fluorescence from the target. Similar codes have been employed throughout x-ray optics [108].

The code simulates photons emitted from a point white light x-ray source and are collimated onto a poly-crystalline sample. The integrated intensity, or

reflectivity, R of a powder is the probability that an individual photon will be diffracted by a set of lattice planes into a cone of half angle $2\theta_B$ [93].

$$R = \frac{M_{hkl} r_e^2 \lambda^3 |F_T|^2 \left(1 + \cos^2(2\theta_B)\right)}{16 V^2 \mu \sin(\theta_B)} \tag{64}$$

where M_{hkl} is the multiplicity for a set of Bragg planes with miller indices hkl, r_e is the classical electron radius, λ is the wavelength of the photon, V is the volume of the unit cell and μ is the linear absorption coefficient. F_T is the temperature diffuse corrected scattering factor defined in equation 66. The expression in equation 64 assumes the sample is thick compared with the absorption length of the x-rays and that they are unpolarised.

The structure factor, F, for a Bragg reflection can be used to determine which reflections will be missing or present due to evaluating to zero or non-zero, and can be calculated from,

$$F = \sum_{n}^{\text{unit cell}} f_n e^{2i\pi(hx_n + ky_n + lz_n)} \tag{65}$$

where x_n, y_n and z_n are the fractional coordinates of the atoms in the unit cell using the lattice vectors as a basis and f_n is the atomic scattering factor which depends on the wavelength of the scattered x-ray and the angle through which it is scattered [109]. The intensity of a Bragg reflection is proportional to $|F|^2$ and so the observed intensity of a Bragg peak is highly dependent on it. The scattering factor decreases with increasing scattering angle and energy which results in diffraction from higher order lattice planes being less efficient.

Bragg's law assumes that atoms lie exactly on a perfect lattice, however this would only be true at 0 K; in a real crystal atoms will be displaced due to

thermal vibrations. This section follows Warren who gives a clear analysis of this effect [93].

If this thermal displacement away from ideal lattice points is assumed to be described by a gaussian distribution, then the disorder introduced by the vibrations effectively reduces the magnitude of the structure factor. This gives the temperature diffuse corrected scattering factor as,

$$|F_T|^2 = |F|^2 e^{-2M} \tag{66}$$

$$2M = 16\pi^2 \left\langle u_s^2 \right\rangle \sin^2\theta_B/\lambda^2, \tag{67}$$

where $\left\langle u_s^2 \right\rangle$ is the average square displacement of the atom in the direction normal to the diffracting lattice planes. The average displacement is highly dependent on the material in question and its structure. For a cubic crystal comprised of a single element it can be approximated; resulting in,

$$2M = \frac{12h^2T}{mk\Theta_M^2}\left[\Phi(x) + \frac{x}{4}\right]\left(\frac{\sin(\theta_B)}{\lambda}\right)^2, \tag{68}$$

where h is Planck's constant, T is the temperature, m is the atomic mass, Θ_M is the Debye temperature, $x = \Theta_M/T$, k is the Boltzmann constant and

$$\Phi(x) = \frac{1}{x}\int_0^x \frac{\epsilon d\epsilon}{e^\epsilon - 1}\ . \tag{69}$$

Modelling of x-ray fluorescence is required to give accurate estimates of the number of noise photons emitted by a sample. The fluorescence modelled here is a result of the backlighter spectrum causing photoionisation of inner-electron shells, which results in emission of x-rays at characteristic energies when the

vacancies are filled by electrons in higher shells. The probability of an x-ray being absorbed is given by,

$$1 - \exp(-\mu L) \ . \tag{70}$$

where L is the thickness of the material in the direction of the x-ray path [110]. The cross-section of particular shells can be estimated by fitting separate absorption curves to the transmission spectrum of the target element. Using this it is possible to estimate the relative probabilities of each shell being ionised due to an x-ray being absorbed, and therefore choose which shell has been ionised during the simulation. The probability of an ionised shell fluorescing is given by its fluorescence yield, which is different for each shell, and decreases for shells with a higher principal quantum number [111]. The energy of the emitted photon can be chosen by the relative line intensities of the emission lines [112].

Fluorescence emission is isotropic so the generated photon is emitted in a random direction. However, for the purpose of speeding up the simulation, photons with a direction that returns into the sample are neglected. The same absorption calculation is also performed for the emitted photon as it exits the crystal to determine if it is re-absorbed. Fluorescence from this secondary absorption is neglected, as it is assumed it will be too low in energy and filtered out.

This method neglects emission from any ablation plasma at the surface of the target, due to the driver beams, or inelastic scattering of the backlighter, which are also key sources of noise.

Figure 19 shows the spectrum measured from a shot using a vanadium sample alongside results from a simulation of the experiment.

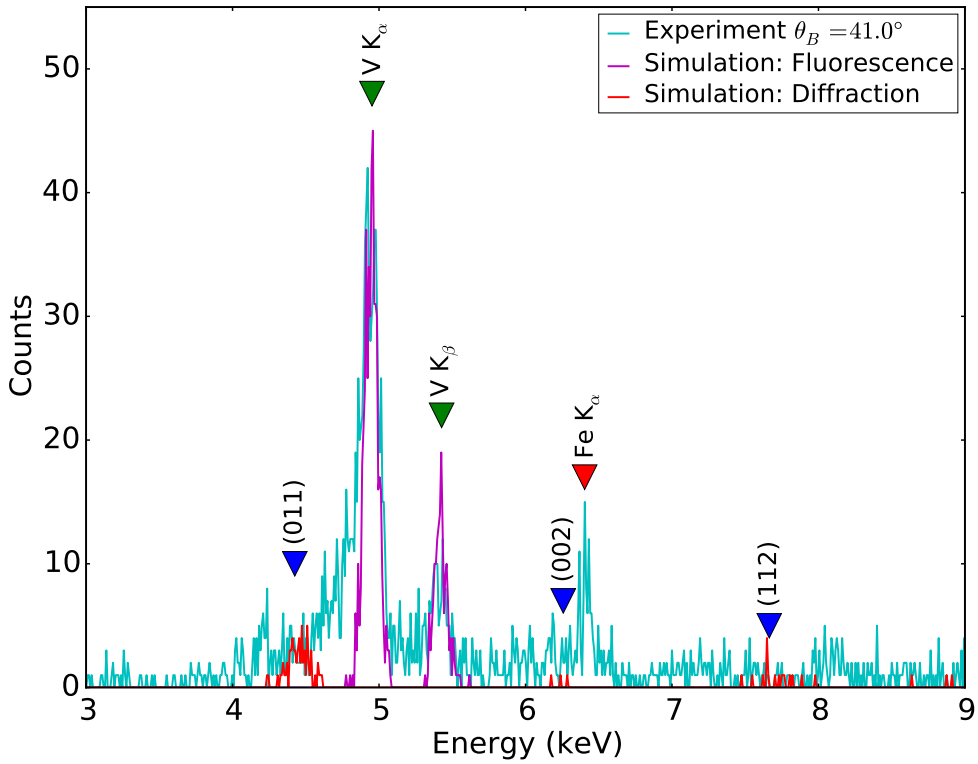


Figure 19: Spectrum measured from Vanadium shot in addition to results from a simulation of the experiment.

There is good agreement between the experiment and simulations for the vanadium emission lines with the position and width of the K_β line matching closely. The good agreement of peak widths and relative heights indicates that the spectral response of the CCD is being modelled well, i.e. its energy resolution and quantum efficiency.

The vanadium K_α line has a low energy tail which could be explained by inelastic scattering, but the significant number of photons in the tail would make this unlikely due to the comparatively low probability of a photon being inelastically scattered.

Charge leakage due to pixel bleeding could explain the low energy tail, as it would result in some of the x-rays being measured as having a lower energy. However the large number of photons in the tail would then suggest a significantly larger number of K_α x-rays than would be consistent with the ratio between the K_α and K_β intensities. Alternatively the tail could be due to titanium He_α emission, an element that was present in the backlighter foil. This is consistent with a different shot where a monochromatic copper backlighter was used and the low energy tail is no longer present, though a broad feature at the copper He_α energy does appear. Incoherent scattering of photons from the backlighter by the target chamber, sample or experimental apparatus could all contribute to producing these peaks.

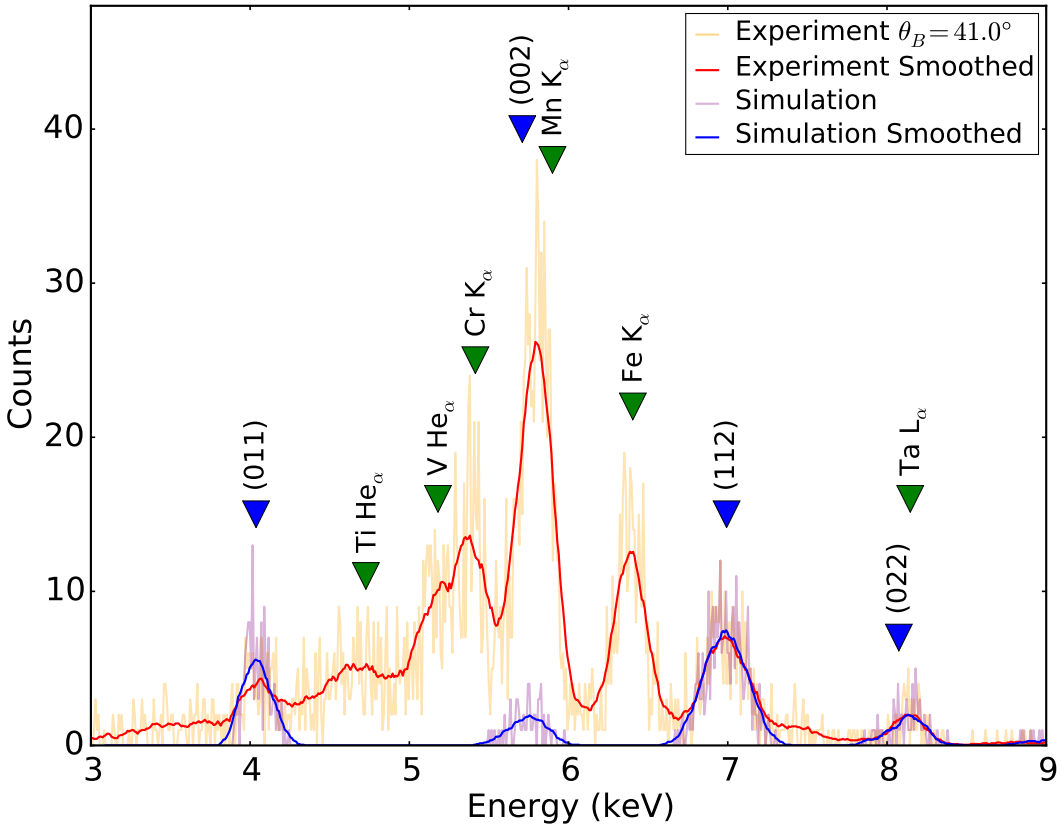
The peak at approximately 6.4 keV is due to iron K_α fluorescence and it was present in many shots throughout the SPEDX campaign.

The simulation shows that a small number of diffracted photons are predicted to be seen in this shot. While there are a small number of x-rays observed at the expected diffraction energies, there are not enough to distinguish from the background. The simulation agreeing with experiment on this point is encour-

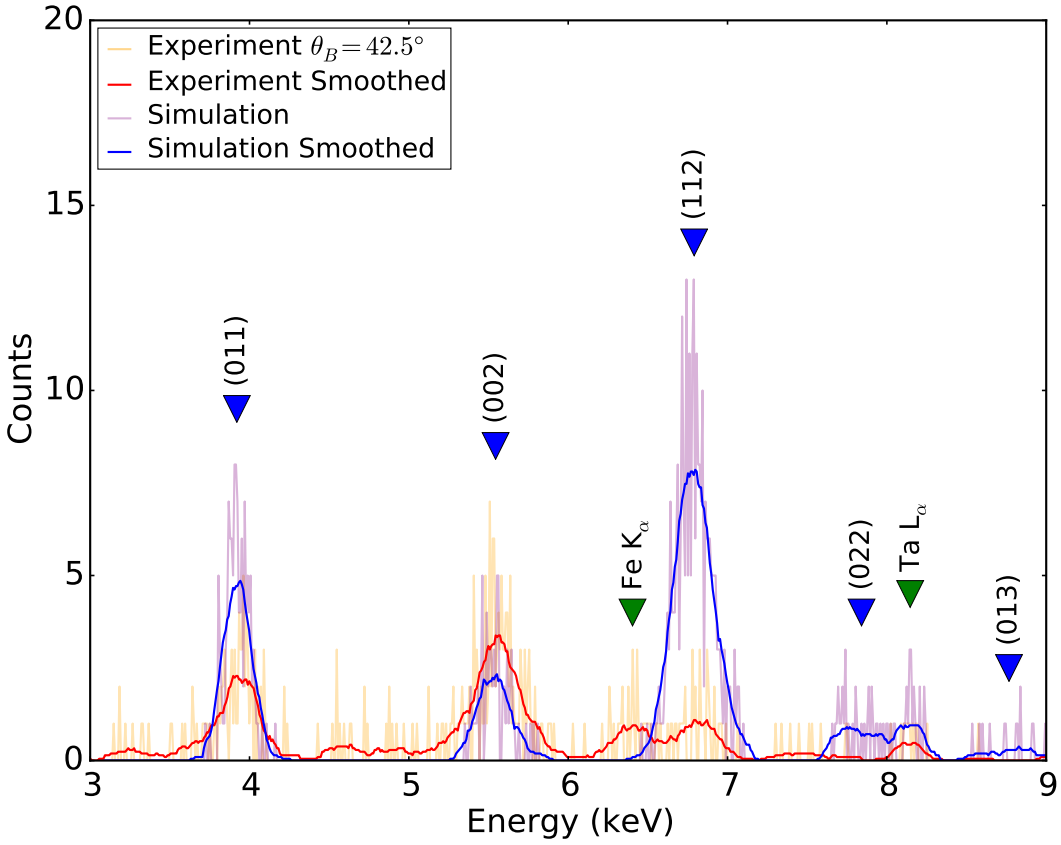
aging, however it shows that one must be mindful of the ratio of fluorescence to diffraction. For elements with a low atomic number, such as vanadium with a correspondingly low reflectivity, when combined with a low energy absorption edge leads to an abundance of fluorescence; thereby limiting the number of pixels available for recording diffraction. This shows that care must be taken when choosing materials with which to use SPEDX. Indeed this is shown in the spectra recorded from tantalum samples where the high reflectivity and lack of emission lines, between 3 and 8 keV, has resulted in clear diffraction peaks.

The tantalum shots were also simulated by the Monte Carlo code and are shown in figure 20. The simulated signal is separated into its diffraction and fluorescence components. We model the x-ray spectrum as blackbody emission with a radiation temperature of 750 eV. This approach allows us to take into account the effects of the high energy tail (that lies beyond the range accessible to our spectrometer), which is responsible for initiating much of the fluorescence. Especially important in the case of Ta where the L-edge lies at the upper end of the backlighter spectrum. In order to account for the variation in backlighter intensity between shots, we adjust the incoming photon flux to approximately match peak heights for each data set. The variation in photon number was found to be consistent with backlighter variation, as estimated from the flat crystal spectrometer data.

The simulations show good agreement with the experimental data in terms of predicted peak positions, with the exception of Ta (002) which also shows a marked discrepancy in peak position. As discussed above this is likely due additional contributions at this energy, perhaps from Mn fluorescence, or a spike in backlighter intensity around 6 keV (outside of the range recorded on the spectrometer). Peak widths are consistent with those observed experimentally.



(a) $\theta_B = 41.0°$



(b) $\theta_B = 42.5°$

Figure 20: Experimental data and simulations of the two laser shots. Relevant spectral lines are indicated along with expected diffraction positions.

3.6 ENERGY CORRELATIONS

Photons which are diffracted by the sample will possess a correlation between scattering angle, i.e. their position on the CCD, and energy. Photons generated from noise processes, such as fluorescence or drive noise, have no such correlation. Subsequently this can be exploited to determine whether a peak is as a result of diffraction or noise. Using multiple CCDs is one such way to do this; however as each pixel on a CCD lies at a different Bragg angle it is possible to do this with a single CCD too.

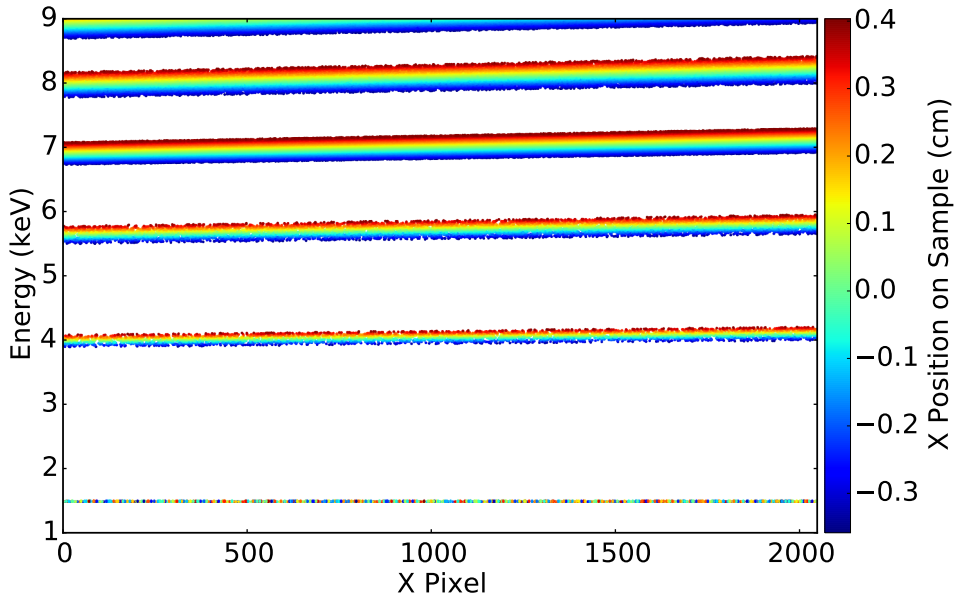


Figure 21: Plot of X-ray energy against position of X-ray along CCD x-axis. Each point is coloured by where on the target it has originated. This simulation was performed with a flat spectrum from 3 to 9 keV for a Bragg angle of 41.0°.

Figure 21 plots the energy of photons against the x-coordinate of the pixel on the CCD, i.e. the dispersion direction in this geometry, from a simulation. Using this, it is possible to investigate the correlation of diffracted photons in comparison to noise photons. From this figure it is clear, due to the gradient of

the lines, that in this geometry, the energy of diffracted photons varies across the CCD for each set of diffracting planes, whilst fluorescence photons do not. The width of the line is an effect of the divergent backlighter beam hitting a large area of the target, resulting in each pixel of the CCD lying at a small range of Bragg angles. The colour of each point indicates where on the target it has diffracted from. It is clear that the fluoresced photons at 1.5 keV, from a simulated aluminium filter, do not show the same correlation.

The correlation (the link between CCD position and diffraction energy) can be quantified by finding Pearson's Correlation Coefficient which is a widely used measure of linear correlation between two variables, typically denoted by the symbol R [113]. It has been calculated from the data presented in Fig. 15 to range from 0.2 up to 0.4 for higher order lattice planes.

These correlation values are lower than would be expected for two correlated variables, likely due to the poor energy resolution of the CCD, but are significantly larger than correlation values for noise photons which show no relationship between position and energy which have correlation coefficients of 0. When the simulation does not include the energy resolution of the CCD the calculated correlations are higher.

These values of R agree with those calculated from matching SPEDX simulations, showing this analysis technique can give some measure of additional confidence that peaks are from diffraction and not a separate noise source such as fluorescence.

3.7 IMAGING PINHOLE

The correlation between scattering angle and energy can further exploited by placing a pinhole between the sample and CCD. This method makes use of the non-zero spatial extent of the CCD and the divergence of the x-ray source.

With a judicious choice of pinhole geometry, this can reverse the dispersion direction of the diffracted x-rays across the CCD. Without a pinhole, the energy of diffracted x-rays will vary with position on the CCD in a certain direction. The use of a pinhole can reverse the direction of this energy dispersion as shown in Fig. 22.

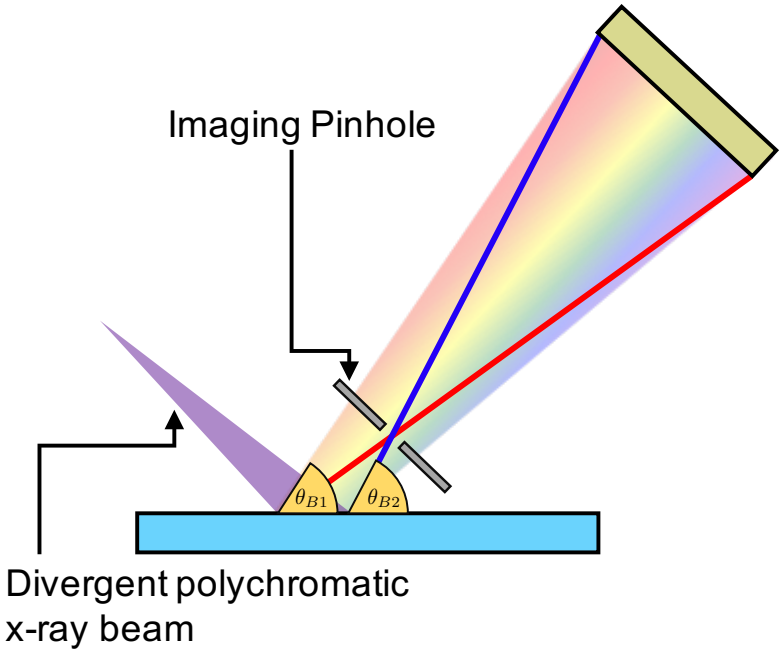


Figure 22: Diagram of SPEDX experiment with pinhole. The pinhole blocks certain x-ray paths so that each position on the CCD can only receive x-rays from a small part of the sample. Given a suitable geometry, $\theta_{B1} > \theta_{B2}$ such that the average diffracted x-ray energy received by the CCD at the leftmost edge of the CCD. Vice versa for the opposite edge.

The presence of the pinhole blocks the majority of x-ray paths, such that each position on the CCD has a much more constrained field of view. This results in each position on the CCD mapping to a small part of the sample and therefore a small range of Bragg angles. This reduces the total number of photons reaching the CCD, but does not affect the signal to noise ratio as each position on the CCD is now mapped to a specific region of the sample.

If the pinhole is positioned correctly then the direction of the dispersion will be reversed compared to those that are discussed in Section 3.6. With specific reference to Fig. 21, each band (due to diffraction from a set of lattice planes) is modified and only photons from the top left to the bottom right of a single band will be able to pass through the pinhole.

In order to determine the optimal pinhole geometry, a simulation with a very large number of photons and geometry identical to that used in Fig. 20a was post-processed with a range of pinholes. The radius and distance between sample and pinhole was varied and the correlation coefficient, R, was calculated for the (112) diffraction peak. The pinhole was modelled as being made of aluminium and was 5 mm thick and fluorescence from it was not modelled as it was assumed it would be filtered out in a real experiment. The pinhole was modelled to be parallel to the CCD surface. The results of these simulations have been plotted in Fig. 23.

Figure 23 shows that there is a large parameter space where using a pinhole will result in a change in dispersion direction. This region is bounded by the yellow region which represents a correlation of zero, i.e. no statistical correlation between photon energy and CCD position, which is the expected behaviour of a noise peak. This plot includes the CCDs spectral response and shows that the use of the pinhole can produce higher correlation values (the blue region

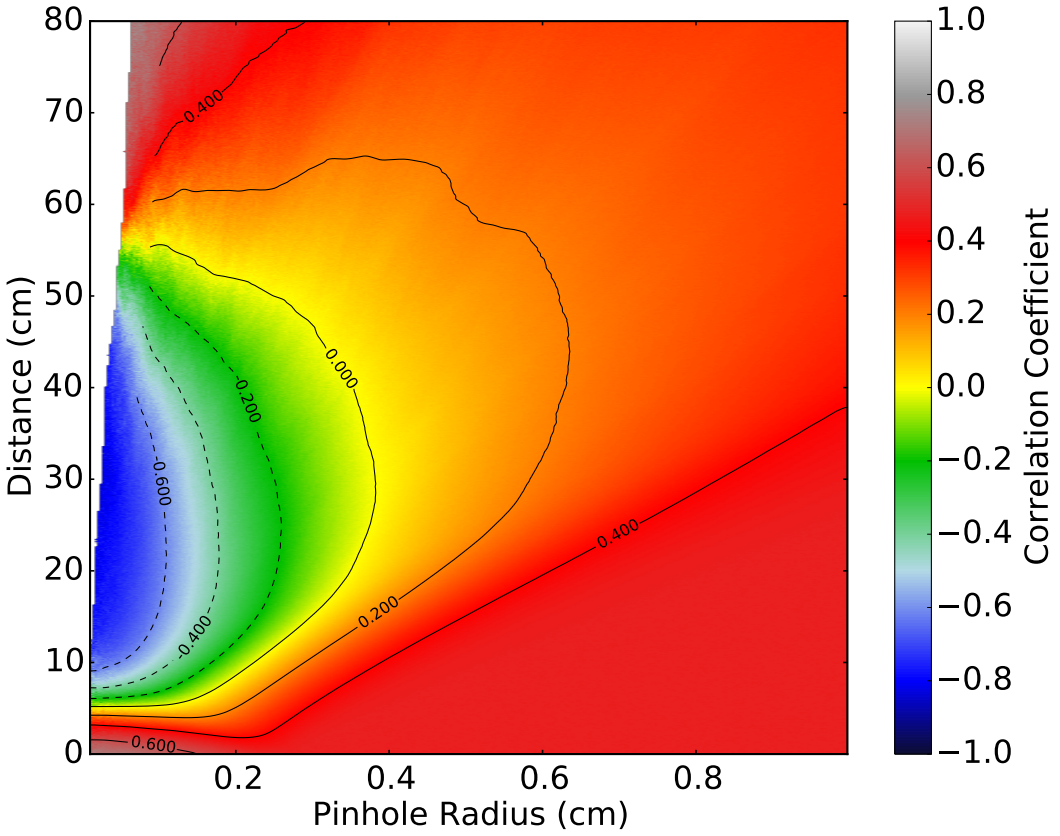


Figure 23: Plot showing correlation coefficient, R, of the (112) diffraction peak from a simulation with a large number of photons, using the geometry simulation in Fig. 20a. It was post-processed to include a pinhole of varying size and distance from the sample. The blank region in the top left indicated that not enough photons (fewer than 100) passed through the pinhole. The contour lines have been calculated using a smoothed dataset to mitigate the effect of random variations.

of the plot) than without the use of one (the red region). This shows that the pinhole can be used as an additional way of determining whether measured peaks are due to noise or diffraction, although this is at the expense of total signal.

The large range of pinhole distances and radii which invert the energy dispersion mean that there is also significant freedom to optimise for other parameters, such as using a wide enough pinhole to allow a larger number of photons

through while still maintaining a high correlation coefficient. For pinhole radii of over 0.05 cm then at least 300 photons are allowed through the pinhole. Thickness, orientation and composition of the pinhole are other parameters that could be explored.

A potential improvement that could be made using this technique is to use an x-ray source with an intentionally large divergence so that there is a correspondingly larger range of scattering angles between sample and CCD. Increasing the divergence would result in increasing the thickness of the lines in Fig. 21 as more of the sample will be illuminated by the x-rays. Care would need to be taken so that the x-ray spot is not larger than the drive spot, which would result in signal being measured from static material.

3.8 CONCLUSION

This chapter covers the first use of the SPEDX technique by any group. It aims to solve or mitigate a number of issues with performing x-ray diffraction experiments at large high power laser facilities. It has also been used to measure diffraction from shock compressed material. The understanding of the material response remains a challenge from this experiment alone, however improvements to the technique are suggested. A simulation code was also developed to help understanding of the technique, which gives particular insight into fluorescence as a source of noise. It can be used to test experimental geometries as part of the planning process. In addition it has been used to investigate a novel experimental geometry using a pinhole to create correlations in the data which could be used to aid in analysis of experimental data.

4

SINGLE HIT ENERGY RESOLVED LAUE DIFFRACTION (SHIELD)

4.1 INTRODUCTION

In-situ Laue diffraction has been used for a number of years to investigate the response of materials under shock compression [59]. A particular strength of the Laue platform is its sensitivity to measuring change in the unit cell of a material [90]. This can be used to infer information about a material's strength, in the context of uniaxial compression; or the symmetry of a unit cell which indicates its phase [60, 90, 114].

Furthermore, the size and shape of the Laue spots can give a great deal of information concerning the number and nature of defects in the material [115].

Laue diffraction is similar to SPEDX in that both utilise a broadband x-ray source, however a single crystal sample is used instead of a polycrystalline one. The x-ray source is similarly collimated onto the sample; the resulting Laue spots are recorded on image plate based detectors, with their positions related to the orientation of the diffracting lattice planes [59]. This ability to record plane orientation allows access to information on symmetry of the unit cell, and in the context of laser compression, has been used successfully to infer strength [60] and defect mediated lattice rotation [90]. However, as only plane orientation and not spacing can be determined from this technique, a full

determination of volumetric compression, a key quantity in materials research, is lacking.

Single **Hi**t **E**nergy-resolved **L**aue **D**iffraction (SHiELD) is an *in-situ* white light Laue x-ray diffraction platform, with the advantage that both the volume and aspect ratio of the unit cell can be measured from the diffraction pattern recorded in a single shot. It utilises one or more CCD cameras, operated in single-photon mode, to record x-rays diffracted from a single crystal sample. As photons are detected individually by the CCD, their energy, and thus the spacing of the diffracting plane, can be recovered. By measuring photon energy for a small subset of Laue reflections, one can fully supplement the cell aspect ratio information provided by the standard Laue technique to provide more complete strain state information for the sample. In particular, measuring the energy of a single Laue spot, and therefore the magnitude of the scattering vector, along with a diffraction pattern recorded on image plate allows the measurement of both the unit cell's aspect ratio and total volume.

This is a particular advantage of the SHiELD technique as it does not compromise the existing Laue platform but instead supplements it, the single photon counting nature of the technique therefore does not affect the platform.

The high signal to noise level associated with the Laue diffraction platform, coupled with the sensitivity of single photon counting, means that the technique is also well suited to high noise environments. This is a feature which may become important in efforts to obtain diffraction from materials at higher pressures, which in turn will necessitate greater laser ablation pressures, resulting in increased noise owing to x-rays emitted by the ablation plume.

The advantages are not limited to higher pressure experiments. More detailed measurements of micro-structure, which the Laue technique is already sensitive

to, are also possible. An example would be to measure the energy of the split Laue spots observed in copper [90]. An energy resolved measurement of this Laue pattern could confirm that they are due to small lattice rotations, or indicate that a different mechanism is responsible.

4.2 EXPERIMENT - JANUS 2014

The first SHiELD experimental campaign was performed at the Jupiter Laser Facility within the Lawrence Livermore National Laboratory. A quasi-white light x-ray source was generated by irradiation of a mixed metal foil backlighter by a 2 ns laser pulse at 527 nm. The beam delivered up to 200 J and was defocused to reach an intensity of $10^{14}\,\mathrm{Wcm^{-2}}$ in a similar manner to the SPEDX campaign discussed in Section 3.4. Again the Ti and V was not present in the backlighter in order to prevent their appearance as noise peaks in any measured spectra.

The x-rays were collimated using a molybdenum tube to limit the divergence of the x-ray beam, constraining the size of the x-ray spot to a diameter of ≈ 2.5 mm on the samples, which are placed 4.2 cm from the x-ray source. A schematic of the experimental setup is shown in figure 24.

A second beam was used to shock compress single crystal samples, via laser-plasma ablation, using temporally square pulses 5 - 8 ns long with up to 70 J of energy. A random phase plate was used with the drive beam, creating a $1\,\mathrm{mm^2}$ square spot on the sample. This achieved intensities of up to $8\times10^{11}\,\mathrm{Wcm^{-2}}$ on target, producing a planar shock of up to 25 GPa within the sample. During the experiment the x-ray backlighter beam was delayed relative to the drive beam, so that the x-rays could probe the sample at different stages of its compression.

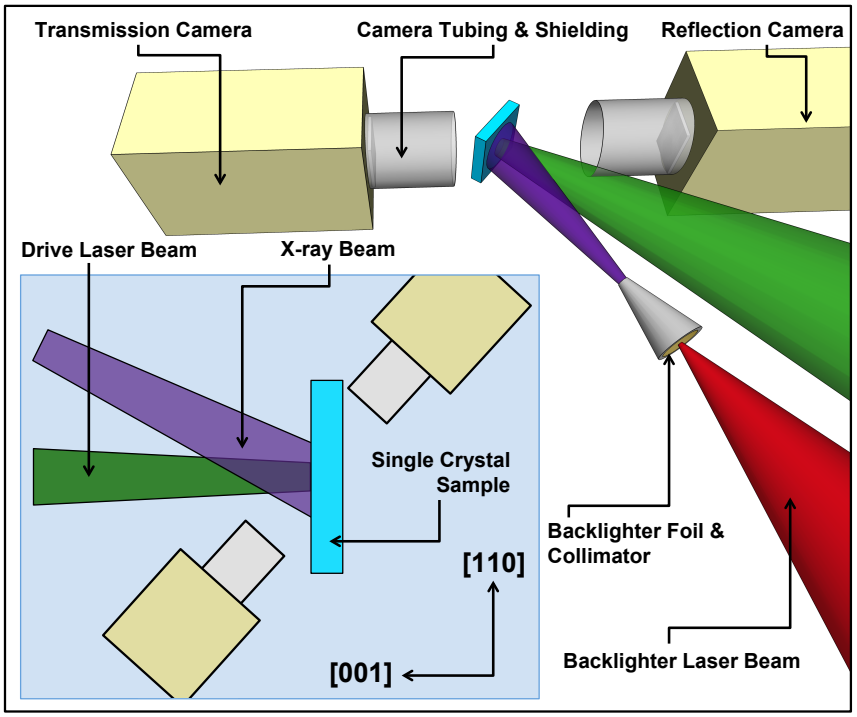


Figure 24: Schematic diagram of the experimental setup. Inset: Top-down view of the experiment highlighting orientation relative to crystal axes.

Samples were 50 µm thick, [001] oriented silicon single crystals with a 30 µm parylene-N ablator and an aluminium flash layer. Silicon was used as near perfect single crystal samples can be easily produced. This also means that it can be more easily simulated by molecular dynamics techniques. In addition, it is highly resistant to forming defects which also have low mobility [116]. This is similar to diamond which has the same structure. The two materials also have higher HEL's than common metals; this is one of the reasons why diamond is often used in high pressure ramp compression experiments. Gaining an understanding of silicon's behaviour under shock compression could lead to further understanding of diamond's response due to the similarities in shock response (High HEL, undergo polymorphic phase transition) between the two.

The sample's rear surface velocity was measured with a velocity interferometer (VISAR), allowing for the determination of sample pressure and shock

planarity [117]. Two different synchronised VISAR measurements were made using different etalon thicknesses, achieving velocity per fringe values of 988 and 1731 ms^{-1}, in order to remove ambiguity due to large fringe shifts whilst still being sensitive enough to measure the shock arrival times.

Two Princeton Instruments MTE CCD cameras were used to detect x-rays diffracted from the sample. They were cooled to - 30 °C to minimise the number of dark counts generated in each pixel. Both cameras were shielded from optical light by thin Be windows and Al coated plastic tubing was used to restrict their field of view to only the target.

For a diagonalised deformation tensor (i.e. one that is parameterised by a transverse and longitudinal strain with no off-diagonal elements), such as one would expect for a purely elastically compressed material, the cameras can be positioned such that they receive signal from Laue spots that do not move under compression. Specifically, these are spots whose associated reciprocal lattice vector lies either parallel or perpendicular to the compression axis. This greatly simplifies setup, allowing us to record diffraction from both ambient and compressed material simultaneously (assuming that the backlighter is timed such that the compression wave is only part way through the sample). For the [001] oriented silicon used here, we record diffraction from the (004) plane, which contains only information on strain along the compression axis, and (220), which is only sensitive to transverse strains due to their geometrical alignment with the sample. The shift in diffraction peak energy allows a measurement of strain to be extracted.

For the camera on the driven side of the sample (the reflection camera which records the (004) diffraction) x-rays from the target were attenuated by a 50 µm aluminium filter and 300 µm PETE plastic placed at the end of the plastic

tubing. This reduced the signal levels measured on the camera and significantly attenuated drive noise (which is typically of photon energy $< 4\,\mathrm{keV}$) from the sample in order to ensure the cameras operated in the single photon regime. The relatively large degree of filtering, compared with standard Laue diffraction, was primarily used to reduce the intensity of the diffraction signal. This is typical for a Laue diffraction pattern and indicates the technique's suitability for high noise environments. For the camera which recorded the (220) reflection (the transmission camera positioned behind the sample) only a beryllium filter was used in order to maximise diffraction signal at the expense of increased sensitivity to drive noise.

4.3 RESULTS

A representative spectrum of photon energies measured from both cameras, for a shot with a driven sample, is shown in figure 25. The data shows a clear peak in the drive side camera spectrum for which the photon energy corresponds to diffraction from the (004) plane of silicon. A similar peak is seen in the transmission diffraction spectrum, where here the main peak corresponds to diffraction from the (220) plane. Note that since the camera recording the (220) plane used less filtering, it is more sensitive to scattered background photons. The peak of the photon energies are very close to those expected for an undriven silicon crystal sample, which are indicated by the green triangles in the figure. This is because the size of the region on the crystal that can Laue-diffract x-rays (which is determined by the x-ray divergence) is larger than the region of the crystal within it which is shock-compressed (which is determined by the size of the drive beam). Therefore the width of the diffraction peak is

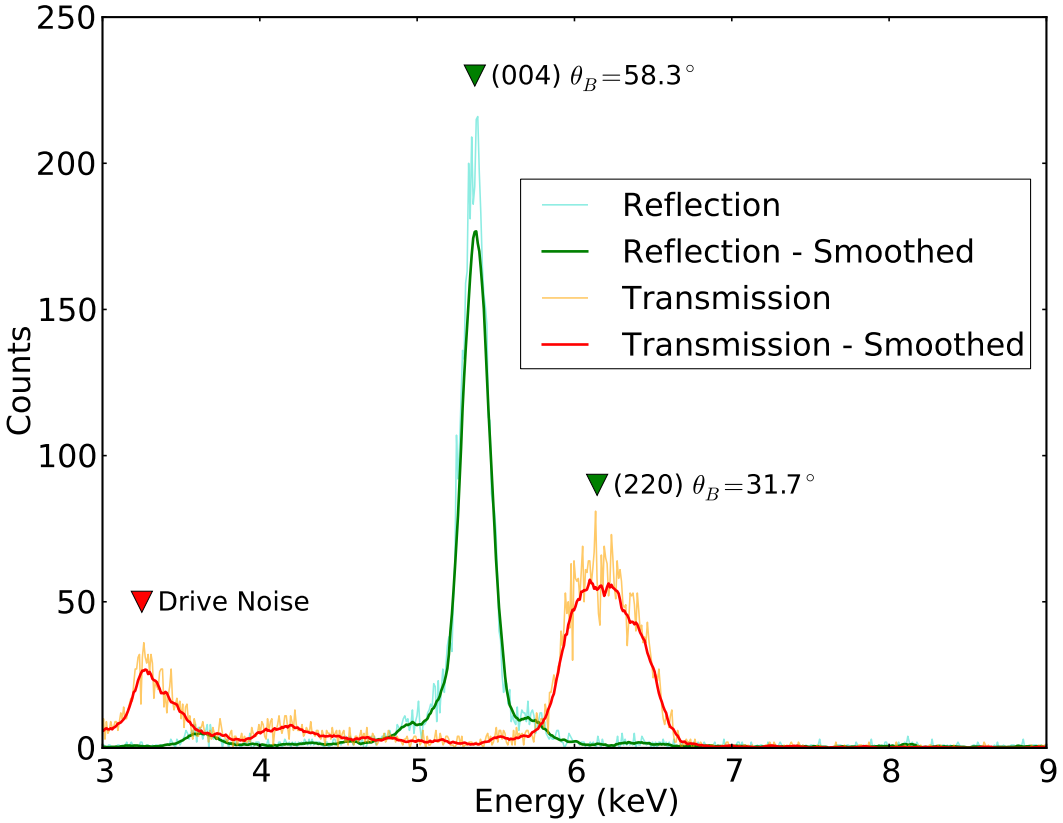


Figure 25: Representative diffraction spectra measured by the two cameras from a single shot. The two Bragg angles indicated sum to 90° which is consistent with diffraction from planes that are perpendicular to each other. The transmission camera measures a large amount of noise from ablation plasma due to having significantly less filtering. This signal is only present on shots with driven samples and the photons are randomly distributed across the entire the CCD which is consistent with noise processes. An example of a Laue spot this has been extracted from is given in Fig. 26

governed primarily by the x-ray divergence which obscured the signal from any driven material.

The position of the photons, colour-coded by energy, which comprise the (004) diffraction peak are plotted in figure 26. It shows a variation in diffracted photon energy across the CCD due to the divergence of the x-ray source. The square drive spot is clearly evident in the centre of the diffraction spot as the region where there is a reduced number of recorded photons. We discuss below the reason for this reduction in the number of recorded photons within the drive spot, but for the moment note that this spatial resolution of the driven region not only allows us to verify the alignment between the x-rays incident on the crystal and the driven region, but furthermore means we can analyse the energy of only those photons that come from the drive region (or, of course, are noise, but may be discarded owing to poor correlation between position and energy).

Additionally, the relative backlighter fluence between shots can be quantitatively measured by measuring the number of diffracted photons per unit area in the undriven region of the diffraction pattern; a measurement which would otherwise require a separate spectrometer. The sharp cut-off of diffracted photons towards the top of the CCD is due to the edge of the single-crystal sample. Photons detected outside of these peaks are believed to be from noise sources, such as incoherent scatter of backlighter or drive plasma x-rays from the target chamber. This interpretation is supported by noting that for these photons we do not see any correlation between photon energy and spatial position on the CCD (i.e. scattering angle).

The spectrum of photon energies measured by the reflection camera, taken solely from the region of the CCD corresponding to diffraction from driven ma-

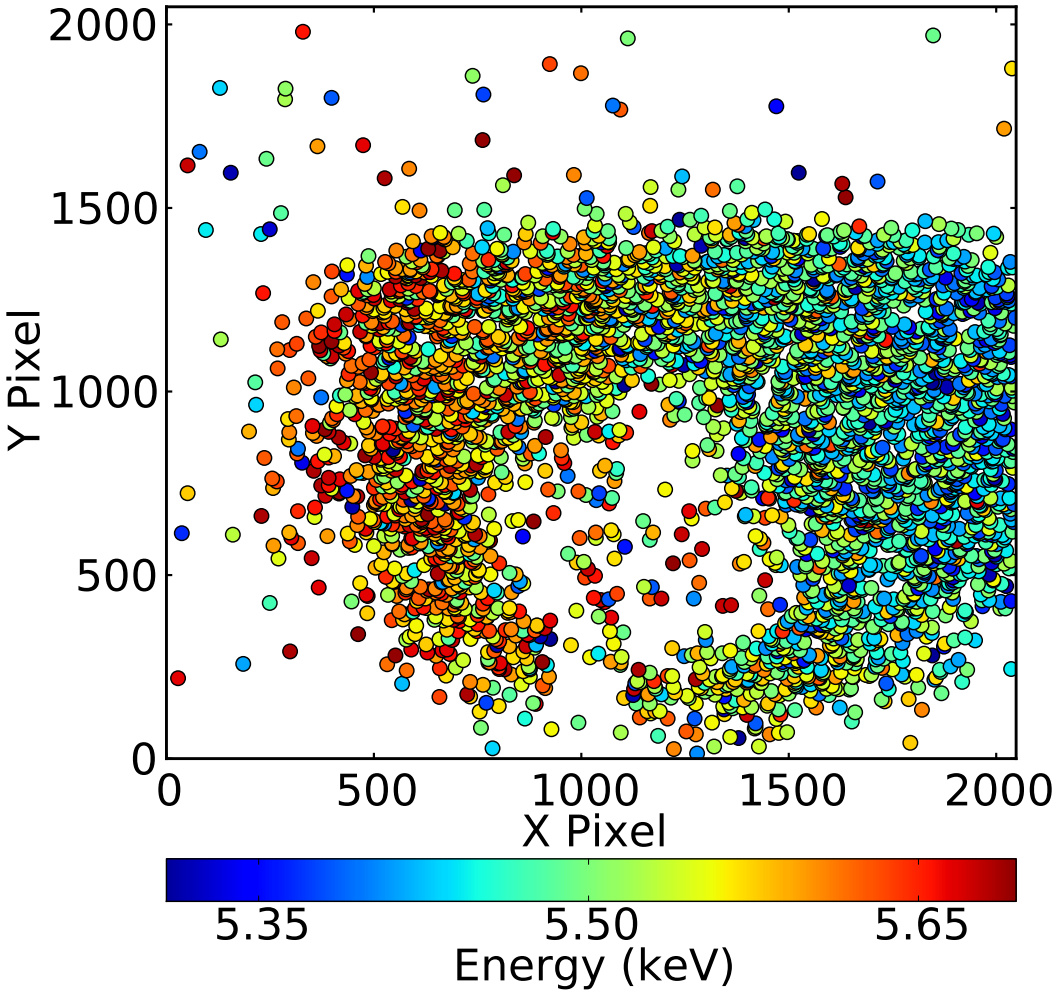


Figure 26: Single photon events comprising the (004) diffraction peak plotted by pixel location. Each photon is coloured by its energy. Note the correlation between energy and spatial position within the diffraction spot which is absent for the noise photons lying outside it.

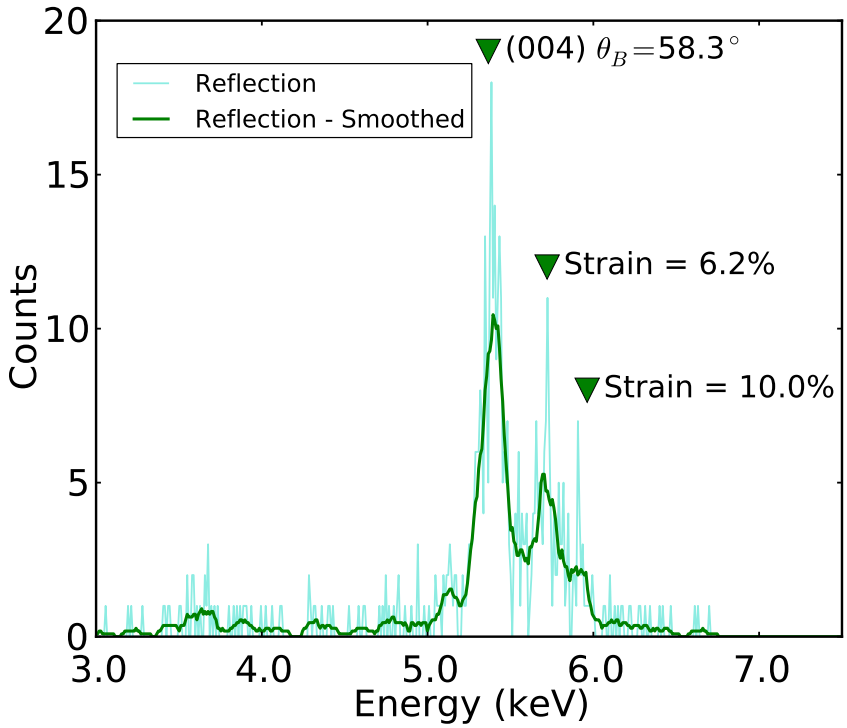


Figure 27: Spectrum of photons taken from within the square driven region, corresponding to driven material, seen in figure 26.

terial, is shown in figure 27. This spectrum shows the diffraction peak from uncompressed crystal, but also a second peak consistent with compressive strain of 6.2 % along the shock direction. There are also indications of elastic response from material at higher strains up to 11 % which is consistent with previous laser compression work where similar anomalous elastic strains are reported [73].

A similar analysis was performed on the energies of the diffracted photons recorded by the transmission camera (i.e. from the (220) planes). However no evidence of transverse strain was observed - only uncompressed material. This observation is also consistent with previous in-situ diffraction work on silicon where no transverse strain was observed, indicating only a purely elastic response from the compressed material contributed to the observed diffrac-

tion [73, 118]. This allows us to infer that the observed strains correspond to $6.2 \pm 0.3\,\%$ (and potentially up to $11 \pm 0.1\,\%$) volumetric compression of the sample. We determine this as volumetric compression as there is only longitudinal compression observed, therefore the total reduction in size of the unit cell (the volumetric compression) is here given by the elastic compression.

Note that without the information about photon energy, which we glean from this single photon detection technique, the white light Laue technique would only enable us to determine that a $6.2\,\%$ differential between longitudinal and transverse strains was present, not the absolute values of these strains. Furthermore, even this information would require diffraction from planes with normals that are not parallel or perpendicular to the compression direction (e.g. in this case (111)) as these are the Laue spots that move under uniaxial compression.

Note also that this technique retains a large degree of spatial resolution. Therefore, in the case of material undergoing small rotations, for which the diffraction will remain within the area of the CCD chip and energy. Thus strain can be resolved over multiple distinct structures, as has been seen in previous work employing Laue diffraction where the splitting of Laue spots allowed for complex material response to be investigated [90].

The velocity profiles which are shown in figure 28 clearly indicate the presence of a two wave structure. The first can be identified as the elastic shock front reaching the rear surface, and corresponds to a free surface velocity of $1\,\mathrm{kms}^{-1}$, which is consistent with a Hugoniot elastic limit of order $9.2\,\mathrm{GPa}$ [71].

The cause of the second wave, corresponding here to a stress of $25\,\mathrm{GPa}$, has previously been associated with plasticity or a phase change [75, 119, 120],

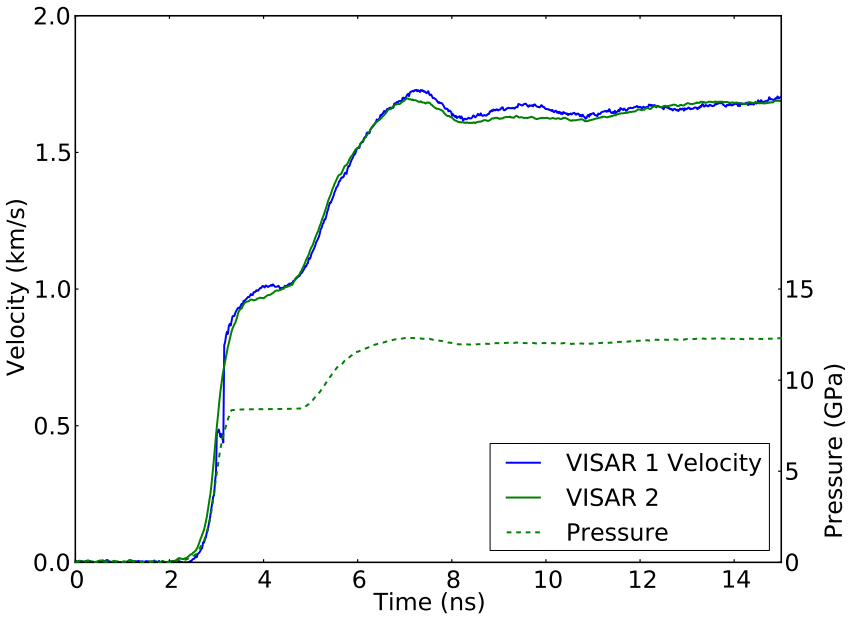


Figure 28: Typical VISAR velocity profile with clear two wave structure. There was similar agreement between both VISAR tracks for all shots. The inferred longitudinal stress has also been plotted.

although there was no direct evidence of plasticity or a phase change in the diffraction data recorded in this experiment.

4.4 ANALYSIS

The decrease in diffraction signal intensity within the driven region of the sample is of particular interest. One possible explanation is that there is simply less material to diffract from and therefore a weaker diffraction signal. This is unlikely to be the case as the loss of diffraction signal occurs for all driven shots. The x-ray pulse was timed such that the shock wave had not reached the rear surface of the silicon. This means that there should have been many microns of silicon remaining throughout the x-ray pulse. As single crystal silicon can

be easily manufactured with near-zero defect density, the dynamical model of diffraction is applicable for the unstrained regions.

The dynamical extinction depth (here, this is the thickness of material beyond which diffraction is not sensitive to) of silicon for this Laue reflection is of order 5 µm; which is much less than the thickness of uncompressed material that remains during the x-ray pulse. Furthermore, a range of x-ray pulse timings were used which all showed a similar reduction in diffraction signal, even for very early backlighter timings.

The reduction in diffraction signal is also surprising due to Loveridge-Smith et al. seeing an increase in diffraction intensity upon compression. This is due to elastically compressed silicon becoming more reflective due to strain gradients in the crystal as it is shock compressed. In turn this results in diffraction from the compressed material being governed by the kinematic model of diffraction. Counter-intuitively this can result in an imperfect crystal having a higher reflectivity than one that is otherwise perfect. This is due to the lack of extinction in a disordered crystal and therefore more material can contribute to the diffraction signal; leading to a higher reflectivity, as long the thickness of the imperfect crystal is high enough.

This indicates a physical discrepancy between this experiment and that of Loveridge-Smith. It is believed that the presence of a second inelastic wave behind the initial elastic wave is responsible for this. Recent work on the Orion laser [121], along with molecular dynamics simulations of silicon have shown that there is a phase change initiated upon shock compression of silicon [114]. This phase change is responsible for the presence of two elastic strains, as were observed in this experiment, along with an inelastic wave behind the initial shock.

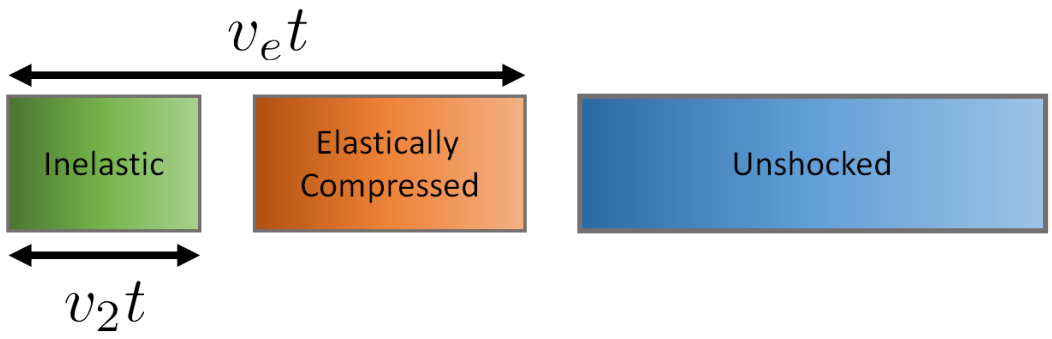


Figure 29: Simple diagram indicating the three distinct regions that are present within the silicon during the x-ray pulse. The shock travels from left to right.

Material downstream of this inelastic wave is believed to be highly disordered and will not diffract efficiently. Therefore it will act as an attenuator and serve to reduce the observed diffraction signal of the material upstream of it. There are then three regions of interest in the sample during the x-ray pulse - the times that the experiment is sensitive to - which are shown in Fig. 29

There are two key differences between this work and the experiment of Loveridge-Smith which could explain the discrepancy between these two experiments. The first is that in this work the diffraction is performed in reflection from the drive surface, not from the rear surface as it was for Loveridge-Smith. As the x-rays must here pass twice through the inelastic region, this experiment is more sensitive to this attenuating material, and so the attentuation is more easily observed and more evident in this work.

The next key difference is that the drive for the Loveridge-Smith work was from a hohlraum type drive and not direct laser ablation. There were also no records of either the laser pulse shapes used to drive the hohlraum nor were any in-situ measurements, such as VISAR, made of the targets. It is plausible that the hohlraum drive had significant pre-heat of the target or a more ramp-like rise in drive pressure. This would then delay the onset of a phase transition and

therefore the inelastic wave relative to the initial elastic shock. This is due to the drive pressure not increasing past the transition pressure for some unknown amount of time past the initial shock. The experiment, therefore, would not be sensitive to the effects of the inelastic material due to its small, or negligible, thickness. Given this second point is based on lack of information, we are less confident about its validity.

4.4.1 *X-ray Pulse Timings*

The extra information gained by SHiELD can be used to validate this three region model of shocked silicon. We start by using the degree of attenuation to determine the timing of the x-ray pulse. This is already approximately known due to the requested and measured delay between backlighter and drive laser pulses. The timing of the x-ray pulse relative to the shock entering the silicon, however, is not accurately known from shot parameters alone due to the dependence of shock speed in the plastic ablator with pressure.

We assume all material behind the elastic shock front, which travels at $v_e = 8.67\,\mathrm{kms}^{-1}$ along the [001] axis of silicon (from Gust & Royce [71]), attenuates diffraction signal from the undisturbed silicon upstream and does not contribute to the static diffraction signal. This region comprises both the elastically compressed material and the inelastic region.

Therefore at any time after the shock enters the silicon, the degree of attenuation of the static diffraction signal by the shocked material can be calculated. The attenuation model assumes the x-rays pass twice through the shocked material at an angle to the target normal. This angle is well known due to the measurement of the Bragg angle of the static diffraction signal. The standard

exponential attenuation model is used and the absorption coefficient is taken from tabulated values [110]. The energy of the x-rays is known (from Fig. 25) and is significantly distinct from any absorption edges in silicon, therefore this model is valid.

This calculation assumes that the remaining undisturbed silicon diffracts as efficiently as the entire length of unshocked material, which is valid as there are tens of microns of silicon remaining during the x-ray pulse which is much greater than the dynamical extinction depth for silicon.

As the lengths and positions of the three regions in the silicon change by a large amount during the x-ray pulse, a time integrated analysis must be used. Therefore the attenuation is integrated for the whole x-ray pulse duration, t_P. Nominally this is 2 ns, but this can vary from shot to shot. As the laser pulse was measured for each shot using a fast diode, this more accurate measurement was used; although the actual length of the backlighter pulse did not vary by more than 0.15 ns for any shot.

The expected attenuation of the static diffraction signal, by the compressed material, can then be calculated as a function of x-ray pulse start time, t_0. Note that this is relative to the shock entering the silicon, which occurs at time zero, and can in principle be negative i.e. the x-ray pulse starts before the drive pulse has entered the silicon, which did occur for one shot. Figure 30 shows an x-t diagram of this, highlighting the x-ray pulse relative to the timings of the experiment.

This calculation means that a measurement of how much the static diffraction signal is attenuated allows the x-ray pulse start time to be inferred. This analysis gives x-ray pulse timings ranging from 1.2 ns before the shock enters the silicon to 1.5 ns afterwards, with each delay consistent with the requested

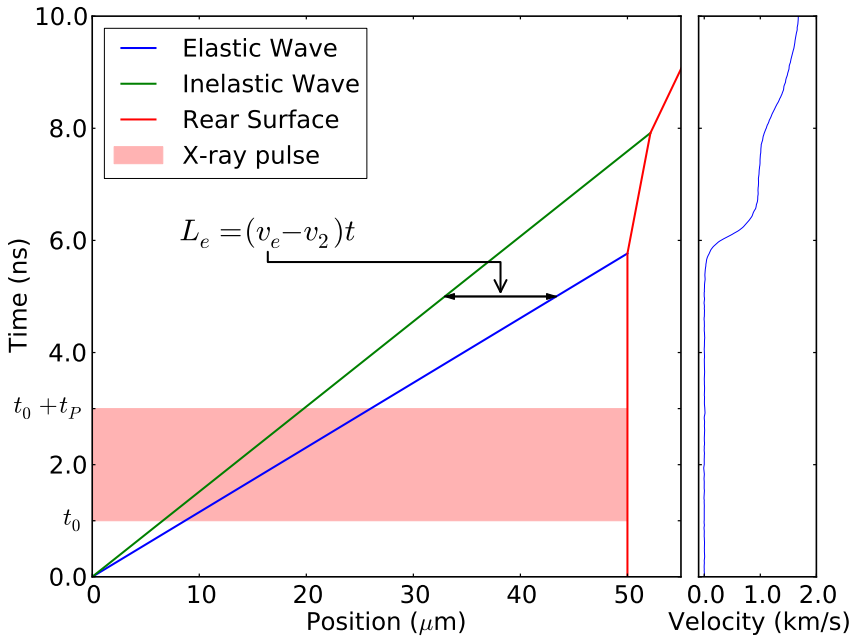


Figure 30: x-t diagram of silicon under laser shock compression plotted alongside the VISAR velocity profile given in Fig. 28 for reference. The x-ray pulse timing is also highlighted.

backlighter beam delay used in the campaign, as shown in Fig. 31. The outlying data point corresponds to a shot with particularly high drive intensity where the shock through the ablator will be faster. Therefore the x-ray pulse is later relative to the shock entering the silicon and the data point is consequently shifted up in the graph.

Finding the backlighter timing (using the analysis described in this section) in this way would not be possible using a single diffraction spot when using image plate based techniques. This is another advantage of using SHiELD where additional information has been gained by virtue of its ability to measure the energy of photons at the same spatial location.

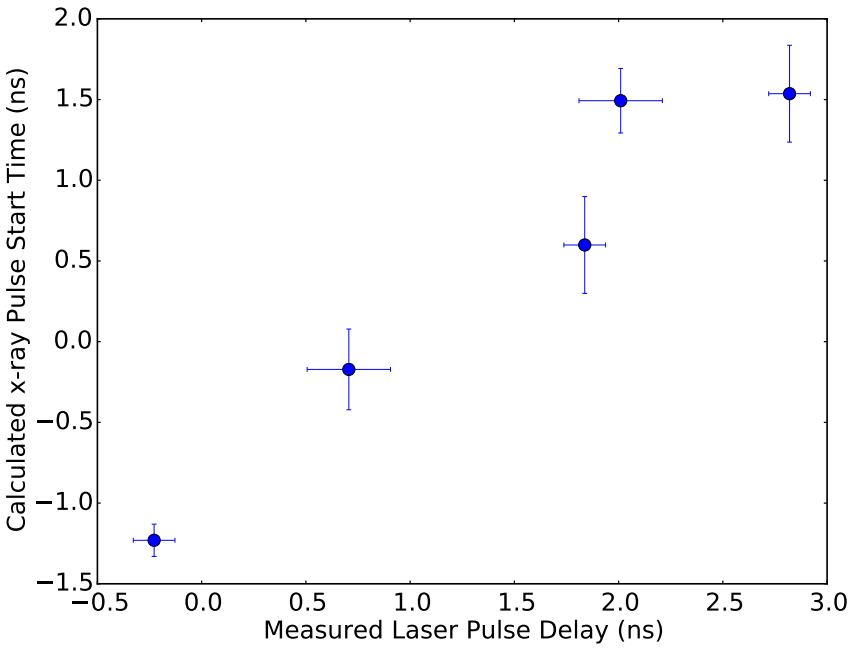


Figure 31: Plot showing the delay of the backlighter laser beam with the x-ray pulse delay calculated from the analysis in section 4.4.1.

4.4.2 *Inelastic Wave Speeds*

We assume that the second wave originates from the silicon loading surface at the same time as the elastic shock wave. This is typical for material responses, which have not been over-driven, where the elastic wave travels faster than plastic or phase change waves.

The material can then be modelled as three distinct regions: the undisturbed silicon at the rear surface; an elastically compressed length of silicon which becomes longer over time but is eaten away by a second wave which serves to attenuate diffraction signal from the two regions ahead; and the material downstream of this second wave. This third region appears to only attenuate diffraction signal from deeper regions as there is no evidence of diffraction from it.

As the speed of the elastic wave is known (8.67 km/s), along with the thickness of the target (50 µm) it is therefore possible to infer the speed of the second, inelastic wave, v_2. This gives wave speeds, v_2, ranging from 6.6 - 7.9 km/s which includes a small correction due to the rear surface moving after the arrival of the first wave. These are consistent with the wave speeds found by Goto et al. and Gust and Royce, [71, 122] where they identify the second wave as a plastic wave. These wave speeds, however, are higher than those observed by Turneaure and Gupta [120]. On the other hand their experiment looked exclusively at stronger shocks than this study; where three successive waves were observed and not just the two found here. It is also worth noting that the sample lengths and timescales of these gas gun experiments were significantly longer than in laser compression experiments. This means that laser experiments are more sensitive to the short timescale dynamics of the phase change and so measuring different wave speeds is not entirely unsurprising [114, 123].

4.4.3 *Diffraction Prediction*

By knowing the the timing of the x-ray pulse and the wave speeds in the silicon, we now have a fully time resolved model of the shocked silicon. That is to say, at any time, relative to the shock entering the silicon sample, we can know the length of inelastic, elastically compressed and static material in the sample. This information comes exclusively from the VISAR measurements.

The degree of attenuation of diffraction signal gives a measurement of x-ray pulse time. The measurement assumes that material downstream of the elastic shock only acts to attenuate the static diffraction signal due to its length.

Importantly it does not assume what the exact nature of this material is and the calculation treats it as a single region.

With this model we can then predict the amount of diffraction we expect to observe from the elastically compressed material, for a particular shot, as we know its length and position. Integration of this for the duration of the x-ray pulse gives a prediction of the effective reflectivity of the elastically compressed material for the whole x-ray pulse. This quantity, denoted E, is explicitly given in equation 71 where terms that do not vary shot to shot have been dropped from the kinematic integrated reflectivity, which is given in Warren [93]. Simplifying in this way means that E is only proportional to the reflectivity. This expression also accounts for attenuation due to material downstream of the second wave.

$$E = \int_{t_0}^{t_0+t_P} \frac{\exp\left(\frac{-2\mu v_2 t}{\sin\theta_B}\right)}{\mu(1-\epsilon_z)^2}\left[1-\exp\left(\frac{-2\mu L_e}{\sin\theta_B}\right)\right]dt, t \geqslant 0 \tag{71}$$

where $L_e = (v_e - v_2)\,t$ is the length of elastically compressed material at time t after the shock has entered the silicon, μ is the absorption coefficient of silicon and ϵ_z is the compressive elastic strain. For times before the shock has entered the silicon (i.e. $t < 0$) the integrand is set to zero.

This is plotted in figure 32 against the measured number of diffracted photons per unit area from the compressed material which has also been normalised by the relative backlighter fluence. This is required to make reasonable shot-to-shot comparisons. The backlighter fluence can be measured from the number of x-rays measured per unit area in the *undriven* region of the sample. This measurement could also be made by using a separate spectrometer which measures the backlighter. However, this method assumes that the spectrum measured by a spectrometer is identical to the one which irradiates the sample. Whilst this is

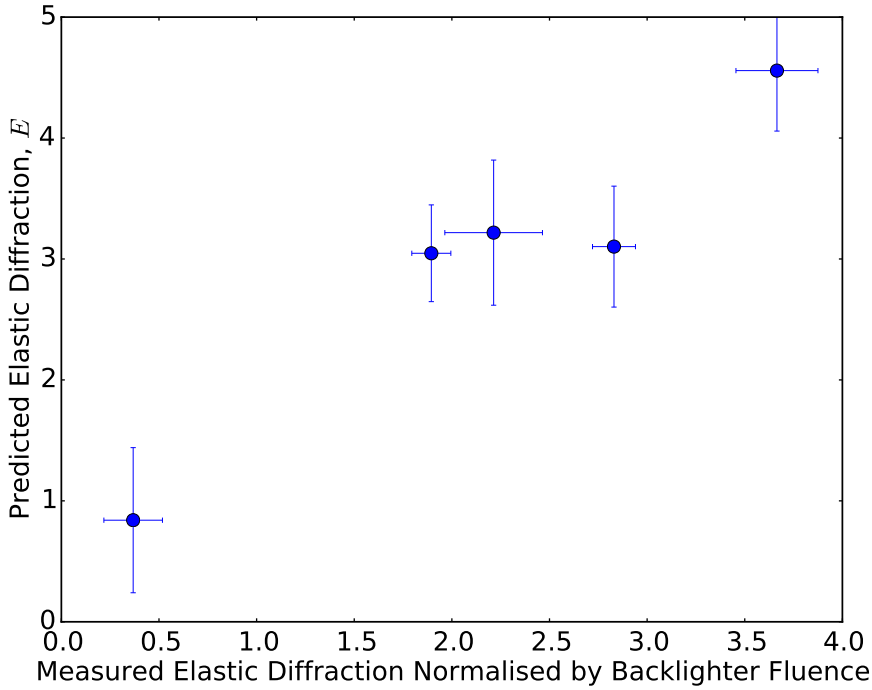


Figure 32: Elastic diffraction predicted using x-ray pulse timing and wave speeds (E) vs amount of diffraction observed from elastically compressed material normalised by relative backlighter fluence. The fact that there is a clear correlation between these two quantities (one a prediction, one a measurement) indicates the validity of the shock response model of silicon proposed here. The similar numbers on both axes, which are in arbitrary units, is coincidental.

likely to be the case, a measurement by the sample itself is more reliable. The figure shows clear correlation between the two quantities, as expected. Note that the x-axis is purely taken from experimental data, whilst the y-axis is the result of the analysis described here which is independent of the x-axis.

Whilst this does not unambiguously show that the model of shock compressed silicon presented here is correct, it is consistent with having three separate regions, giving some confidence to our interpretation. Further work to investigate the nature of the inelastic region would be of great benefit in investigating this.

4.5 EXPERIMENT - JANUS 2015

To follow on from the experiment discussed in Section 4.2, a similar SHiELD experiment was performed. This experiment was nearly identical to the previous experimental geometry, but with a small number of differences. A key difference was sample design, where germanium was used instead of silicon. For many of the same reasons discussed in Section 4.2, work on germanium can lead to gaining understanding of other group 14 materials. An advantage of using germanium is that its phase transition occurs at a lower pressure than both diamond and silicon. Therefore experiments to investigate its behaviour near the phase transition can be done using less intense laser pulses and so result in an experiment with less intense noise sources.

Additionally the germanium samples were orientated with the [111] axis being perpendicular to the sample's surface. There has been relatively little work done on shock compression of [111] germanium compared to silicon and diamond; investigating the response of germanium when shocked along [111] could lead to further insight on how cubic diamond materials of this group relieve shear stress given their similar high HELs and that these materials all undergo a polymorphic phase transition.

The samples were also thick 500 µm targets. Importantly this means that no useful VISAR data could be gathered. This is due to the fact that the release wave from the end of the drive pulse will overtake the inelastic and elastic waves, before they reach the rear surface. Note that this means the analysis of wave speeds in Section 4.4.2 is not possible in this study.

In addition, as the targets are thick, there was no expectation of recording diffraction signal on the CCD placed in transmission, i.e. the camera positioned

opposite to the drive side of the sample. Whilst a CCD was placed in the same transmission position as the previous experiment, it did not detect any diffraction signal for any shots.

4.5.1 *Analysis*

A new analysis method was developed to analyse the diffraction pattern recorded by the SHiELD technique. As the CCD subtends a small range of Bragg angles the energy of diffracted photons will vary across the CCD. This is seen in Figs. 26 and 33 where the colour variation across the image indicates this variation in energy.

This variation in diffraction energy leads to increased width of the diffraction peaks; which is disadvantageous as it makes it more challenging to gather precise structural measurements. Furthermore it prevents making measurements of quantities such as defect density which are closely related to the width of diffraction peaks.

Instead of fitting the entire CCD to a single Bragg angle, for this later experiment we instead fit it as having a Bragg angle that changes across the CCD surface in the dispersion direction of the experiment, which in Fig. 33 is along the horizontal axis. There was no vertical dispersion found in any shots of either experiment which is unsurprising considering the geometry of the experiment.

In an effort to make this process as automated as possible, which will become increasingly important for upcoming laser systems where the shot rate can be sensibly described in Hz, this analysis was written to be primarily governed by a computer; rather than require a human to perform manual fits at every step.

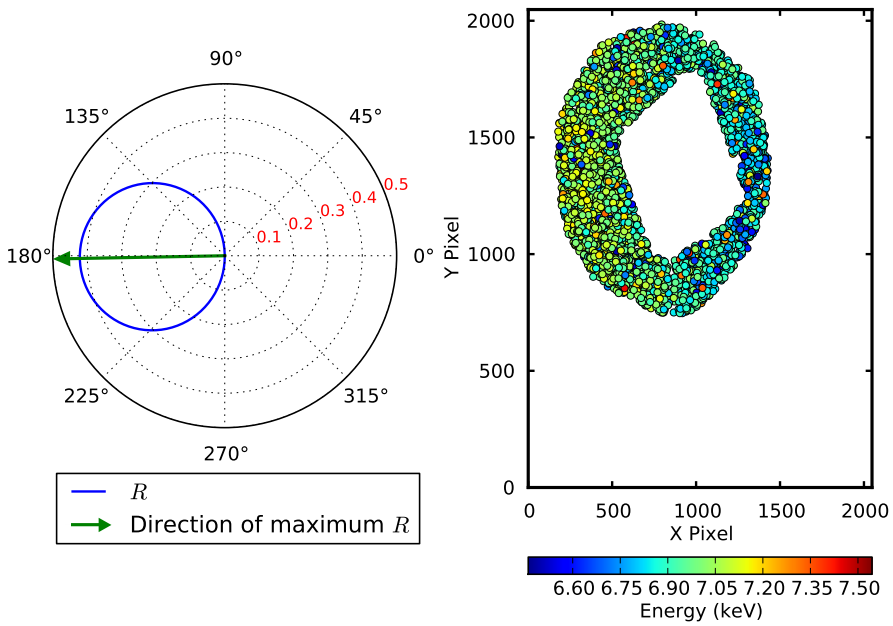


Figure 33: Left: Polar plot of correlation coefficient with angle on CCD. Right: Figure of photons diffracted from undriven part of the sample. The variation in colour indicates the dispersion across the CCD that we are trying to find.

First, only photons from the undriven region of the diffraction pattern are used. This prevents the photons from the driven region, which are from a potentially different lattice spacing and so follow a different dispersion relation across the CCD, from hindering the analysis. Note that once CCD position has been linked to Bragg angle, this can then be used for the driven region. It is only the initial determination of this relationship that must use the diffraction signal from the undriven region of sample.

Given these photons and their positions on the CCD, the direction of highest correlation between position and energy is found. Specifically this means that a dispersion direction is assumed, e.g. 45° from the horizontal, and all the photon positions are fit to that direction. This is done from 0 to 360° and the correlation coefficient is calculated for all of them. The highest correlation coefficient indicates the 'best fit' for dispersion direction.

This is shown in Fig. 33, where shown on the left is the polar plot showing how the correlation coefficient varies with the assumed dispersion direction. The green line indicates the maximum dispersion direction. Note that for angles going clockwise from 90 to 270°, the correlation coefficient is negative and therefore overlaps the positive correlation coefficients is the opposite direction i.e. 180° around the figure.

It should be noted that this analysis assumes a linear dispersion across the CCD. Other forms such as a quadratic dispersion or one based on a trigonometric function were tried. However as the CCD subtends a small range of Bragg angles these were not found to perform any better and so a linear dispersion was assumed. For experiments where the CCD is placed closer to the sample and with a more divergent x-ray source, it may be effective to assume an alternative model for the dispersion.

The dispersion direction was found to agree for all shots to within 3° which is a highly consistent fit. This is unsurprising considering the repeatability of the experiment. The variation may be the limit of the analysis technique. It could also be a result of small physical variations in the experiment such as small movements the in backlighter, sample or CCD positions.

Once the dispersion direction has been found, locations on the CCD can then be fit to the corresponding Bragg angle. Therefore each photon, with its energy and location having been measured, can be assigned a d-spacing value. Therefore instead of plotting the diffraction pattern in energy it can be plotted in d-space, which is often a more useful quantity than energy as it is directly related to the lattice being measured. This has been done for the shot analysed in Fig. 33 and is shown in Fig. 34.

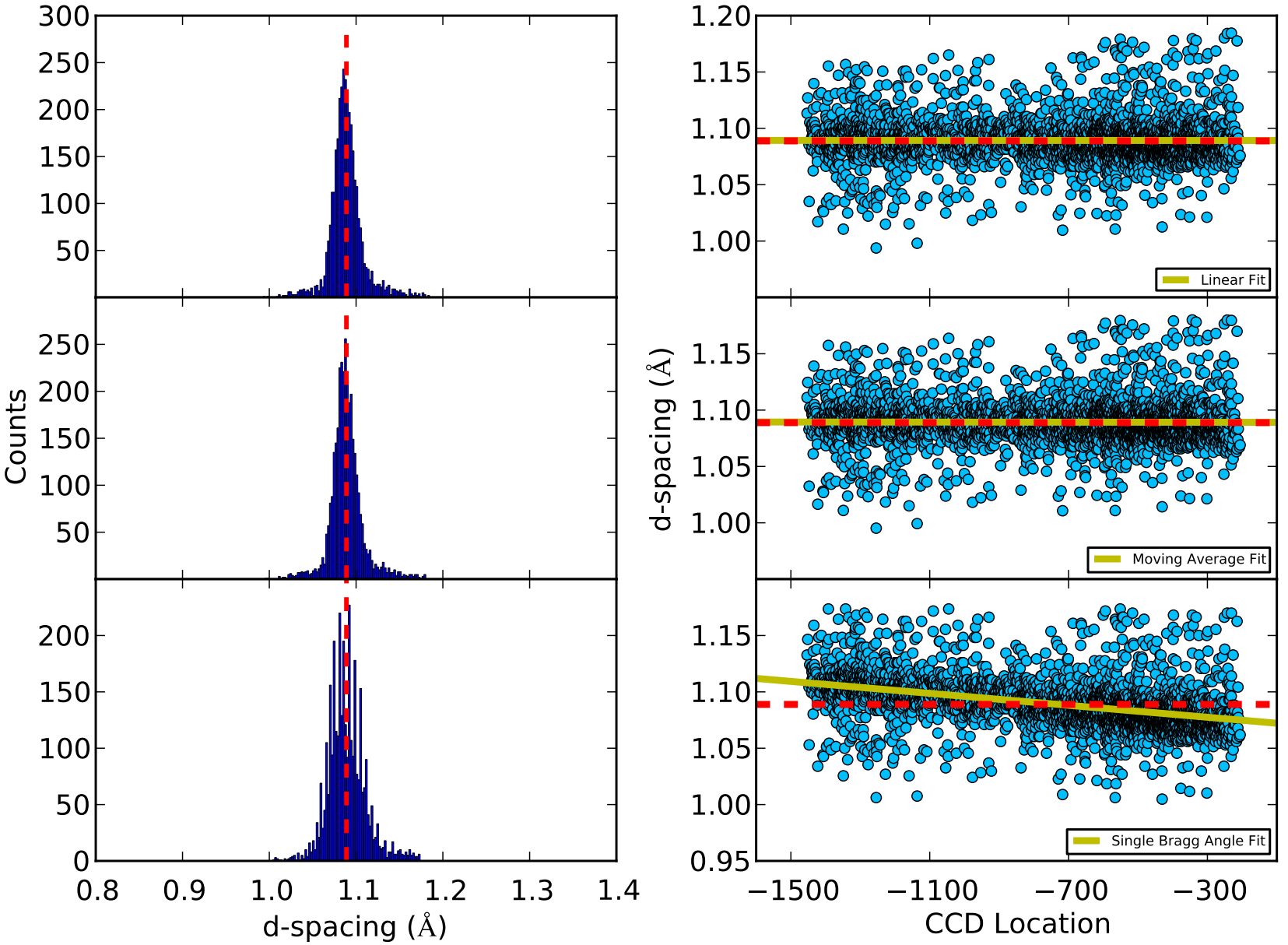


Figure 34: Plots showing results from different methods of fitting the CCD to Bragg angle. Left: Plots of diffraction patterns in d-space. Right: Plots of photons showing their position on the CCD, along the dispersion direction, with inferred d-spacing. Top: Linear Bragg angle fit across CCD. Middle: Average photon energy at each position used to infer Bragg angle. Bottom: Single Bragg angle used for entire CCD

This figure compares the difference between the previous method of analysing the diffraction patterns and the alternative one discussed here. It is immediately evident that the shape of the diffraction peak has changed significantly. Surprisingly the width of the peak has not significantly changed, its standard deviation remains at 0.02 Å; however it much more closely resembles a smooth gaussian than the previous, highly structured peak shape.

4.5.2 *Elastic Strains*

The process of fitting of the CCD surface to corresponding Bragg angles, as described in the previous section, allows diffraction patterns to now be plotted in d-space instead of energy. This has been done for a representative shot on germanium shown in Fig. 35, where the diffraction pattern from the driven region has been plotted.

In this figure there is the familiar combination of undriven and driven peaks, similar to those seen for silicon. There is a small 3.0 % compressive strain, which is just resolvable from the (333) peak. A similar peak can be resolved from the (444) peak however it is very close to the background noise level at only 3 counts. In addition there is a noise peak very close to this, which has a higher number of counts, thus casting a great deal of doubt over whether this peak is really diffraction from the (444) plane of compressed germanium.

In comparison to the results from Section 4.3, the driven diffraction peaks measured from germanium are less resolved compared with the peaks observed from silicon, despite the fact that the diffraction signal is actually stronger from germanium. This is not surprising as germanium has a lower HEL at a lower corresponding compression. Therefore the highest elastic compression

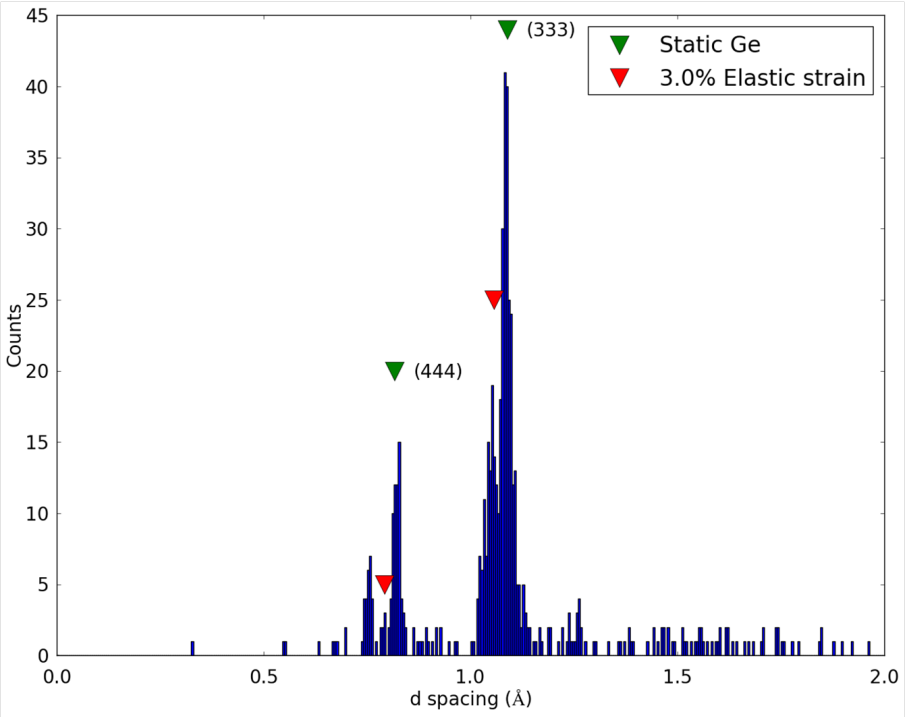


Figure 35: Representative diffraction pattern corresponding to the driven region of a germanium shot.

that germanium reaches is expected to be lower than that of silicon. The smaller change in d-spacing will therefore be difficult to resolve from the natural width of the lines; which are a result of the energy resolution of the CCD. As with SPEDX, performing the experiment at higher energies, and therefore being able to diffract from higher order lattice planes, would be advantageous.

Additionally only a single elastic strain was observed from germanium for any individual shot; in contrast to the multiple strains observed simultaneously in silicon. This indicates that they were either unresolvable using this technique, or that they were not present. Without further experiments it is not possible to distinguish which of these cases is true.

This analysis was repeated for all the driven shots in the campaign. As there were no VISAR measurements made, the shots can not accurately be assigned a pressure. However as the drive pulse shapes were nominally similar for all the

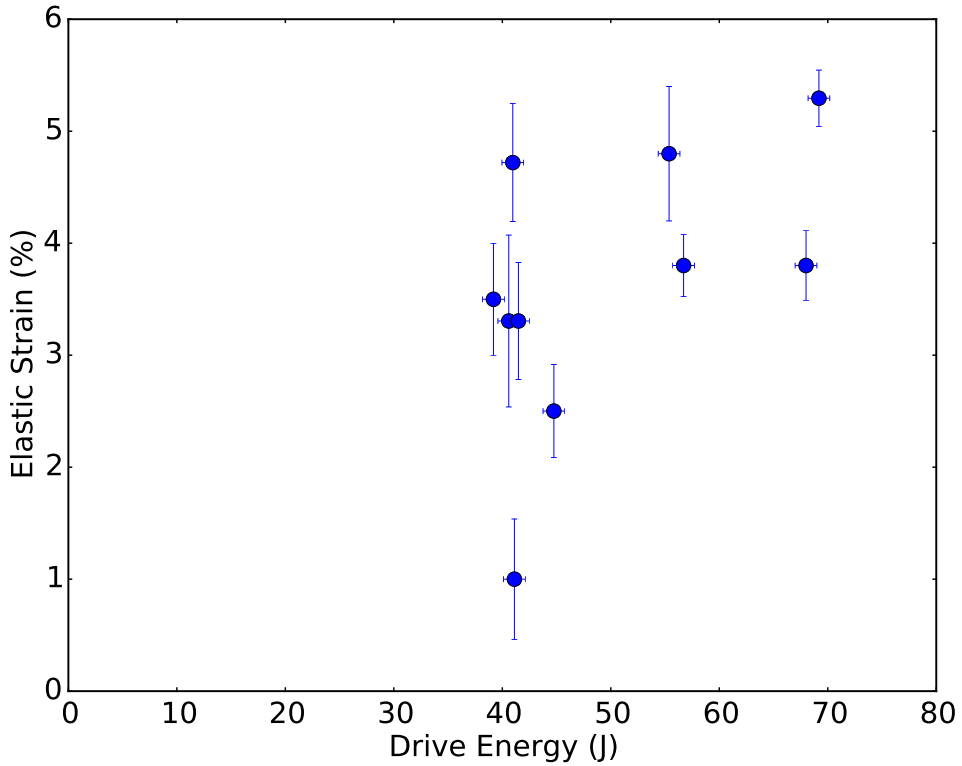


Figure 36: Plot of measured elastic strains against drive energy. Each point represents a distinct shot.

shots, in pulse length and shape; they can be compared by drive energy. This has been done in Fig. 36.

This figure clearly shows a rapid rise in elastic strain with drive energy, which is directly linked with drive intensity. However there is no clear link between the two which indicates that drive energy alone is not a good measure of material pressure. This could be due to small differences in the pulse shape, such as the rise time of the pulse, having a larger than expected effect on the material. Given that there is no in-situ measurement of the material compression, other than diffraction, in this experiment it is difficult to draw conclusions from this figure.

It does however indicate that a range of compressive strains were observed, from as low as 1 % to as high as 5.4 %. If this compression is assumed to be

elastic, then this corresponds to a maximum pressure of ≈ 10 GPa. Interestingly these elastic compressions are higher than the HEL, which corresponds to 2.7 % elastic compression at 4.7 GPa for [111] orientated germanium [124]. However, elastic compressions above the HEL have been observed before in a laser-driven experiment. Nakamura et al. observed compression of 4.3 % [125, 126]. Whilst their work did not go to higher drive energies, so this is not an upper limit, it is consistent with this study showing elastic compressions above the HEL.

4.6 CONCLUSION

SHiELD has been shown to be a useful extension of the Laue diffraction platform. It has been used successfully on the first attempt to both prove the technique and also gain an increased understanding of Silicon. This improves upon the results of Loveridge-Smith where this experiment makes measurements of rear surface velocities and has improved drive characteristics. The technique was also used successfully to investigate germanium, where there has been little x-ray diffraction work on shock compressed samples. Steps towards automated analysis have also been made, which will be key in the future on high repetition rate experiments where the volume of data is too high to be analysed by hand.

5

MOLECULAR DYNAMICS SIMULATIONS OF SHOCK COMPRESSED GERMANIUM

5.1 INTRODUCTION

Molecular Dynamics (MD) is a simulation technique that has been used for many decades to study the evolution of many body systems [127, 128]. The simulations are comprised of many interacting atoms or molecules. Current state of the art simulations can contain billions of particles [129]. The interactions between particles are calculated using inter-atomic potentials, of which there are many forms. The earliest, and simplest, potentials take Lennard-Jones like forms where the interaction is described by pairwise and radially uniform attractive and repulsive terms [130, 131]. Later work resulted in increasingly complex potentials taking into account the effects such as many body interactions and included contributions from density functional theory calculations [132–134].

The simplest form of molecular dynamics conserves the number, volume and energy of particles in the system. This is commonly referred to as an NVE ensemble which is equivalent to the microcanonical ensemble in statistical mechanics. This is achieved by integration of Newton's laws using the chosen potential which describes the forces between interacting particles. This is the integration scheme used in the work presented here, which corresponds to an adiabatic process. Other ensembles exist to conserve other variables, such as

temperature or pressure, where modifications to Newton's equations are used to model interactions with some external energy source or sink. Simulations of this kind are completely deterministic where the evolution of a system will be identical given the same initial conditions and boundaries.

A key advantage of MD codes over others, such as hydrocodes based on a fluid model, is that full information of every particle can be determined at any arbitrary time step. That is to say, quantities such as potential energy, position and velocity can readily be extracted from simulations. This allows for detailed examination of the evolution of the microstructure of materials rather than being limited to bulk properties alone (which can also be easily recovered from MD simulations). One significant success being the phase transition of iron predicted by MD simulations, whilst predictions of other microstructural effects such as twinning have too been made [135, 136].

Classical MD simulations were performed using the Large-scale Atomic/-Molecular Massively Parallel Simulator (LAMMPS) code developed by Sandia National Laboratories [137].

In order to aid the analysis of the Janus experiment discussed in Chapter 4, a number of molecular dynamics simulations were performed to simulate the response of shock compressed germanium. Indeed, there have been very few molecular dynamics studies of shock compressed germanium, with the majority of studies being limited to low pressure work and interactions with other materials, such as silicon, in nanoscale structures [138–140].

In fact the only published MD work on shock compressed germanium up to high pressures is limited to Lane and Thompson (2009) [141]. In their work, primarily concerning shock compression along the [001] direction, they find that beyond the HEL, shear stress is relieved by a polymorphic phase transition

to a β-Sn phase. The phase changed material develops in bands which are qualitatively similar to the responses seen in MD simulations of silicon and carbon [119, 142], other group 14 elements that also have stable cubic diamond structures at ambient conditions. This is in stark contrast to MD studies of materials such as copper where shear stress is relieved by defect mediated plasticity [143].

A more detailed MD study of germanium could therefore give insight into both germanium's response to shock compression and that of other cubic diamond materials.

5.2 SIMULATION DETAILS

This section discusses in detail how to reproduce the simulations of this work.

5.2.1 *Potentials*

There are very few potentials available for germanium compared to silicon and carbon, perhaps owing to their more ubiquitous presence in nature. This study was performed using the second of the two germanium Tersoff potentials [132] and a recent Modified Embedded-Atom Method (MEAM) potential which purports to be a better match to experimental data than the Baskes potential [144]. These potentials were chosen as they had not been used in the work of Lane and Thompson and both claim to be improvements upon previous potentials of the same type. Note however than none of these potentials have been fit to high pressure work, gained via dynamically compressed or static techniques.

Both potentials calculate the potential energy of an atom from a series of pairwise interactions between nearby particles within a cutoff radius, but also include the effect of the local environment by considering the location of a third atom. In particular the MEAM potential studied here is a second nearest neighbour (or 2NN) type where an additional neighbouring atom is considered compared to the standard MEAM formulation.

The majority of the work presented here is using the more advanced MEAM potential. It should be assumed that this is the potential being used, unless the Tersoff potential is specifically referred to.

5.2.2 *Shock Method*

There are several methods of launching shocks in MD simulations, such as creating a high temperature or pressure region to emulate a drive surface [145–147]. Simulations of this kind are commonly referred to as Non-Equilibrium Molecular Dynamics (NEMD) simulations. The most common approach of initiating a shock, and the one employed in this work, is to create an artificial piston at the surface of the simulation box. The piston is comprised of a number of layers of atoms each given an artificial velocity which launches a shock into the material. The piston needs to be thick enough to prevent atoms from the driven material passing through it. This is easily achieved by having a piston many lattice constants thick and for the simulations presented here the piston has a thickness of 15 Å.

The piston was a 'warm' piston; the atoms that comprised it were allowed to equilibrate with other atoms in the simulation for a length of time, referred to as the equilibration time. Following this equilibration time, lasting 2 ps, the forces

on the piston atoms were set to zero for every timestep and their velocity was set to the desired piston velocity. This prevents the piston from being affected by the remaining atoms in the sample but does allow the piston atoms to affect the others. This results in the piston retaining its structure, whilst still driving a shock into the sample.

Creating a piston in this way results in the particle velocity, U_p, being equal to the piston velocity. This facilitates easy and accurate control of this variable in simulations. This is confirmed when the particle velocity is calculated from the simulation and found to very closely agree with the input piston velocity.

5.2.3 *Initial Conditions*

There are a number of simulation parameters beyond choice of potential and piston type. Of particular importance are the initial conditions of the simulation which can have a significant effect on the result of the simulation. In particular, initial pressure and temperature (and therefore density) play an important role in the later evolution of the simulation. This study covers two initial temperatures, 5 and 300 K. Simulations at 300 K were performed as they more closely resemble experiment; whilst simulations at 5 K were used due to the reduced amount of random thermal vibrations of atomic positions, which greatly aid in the analysis of the microstructure of the simulated material. Choice of initial temperature is a relatively straight forward parameter to control in the LAMMPS code, as it is directly related to the initial velocities given to each atom. The direction of all these velocities are randomly generated and isotropic, however their magnitudes have a gaussian distribution where the mean is scaled to give the desired temperature.

As dynamic compression experiments are usually performed at zero initial pressure, these simulations were set up to match that. Integration techniques other than NVE can achieve this, but a simple and more robust way to control initial pressure is by setting the initial lattice constant, i.e. the initial density. The ideal lattice constant to achieve zero initial pressure is different for each temperature, due to thermal expansion and can vary between different potentials. We found the variation in lattice constant to be small, less than 0.3 %, for the temperature range covered in this work.

Determination of the ideal lattice constant is not trivial and requires the use of separate simulations to determine it. A cubic simulation box was used with side length equal to 50 lattice spacings. The simulation boundaries were set to be free surfaces so that the lattice was able to freely expand or contract. The temperature of the simulation is set using the same method described previously. This lattice was then simulated for 100 ps with snapshots of the simulation taken every picosecond.

Simply using the volume of the simulation box to calculate the lattice constant can lead to large errors due to the sensitivity of the box size to only the outer layer of atoms and not the lattice as a whole. Additionally the surface boundaries as reported by LAMMPS do not necessarily correspond to the edges of the lattice; which while useful for computational purposes leads to errors in using this to determine the lattice constant. Therefore it is extremely important to use a Fourier Transform (FT) which is calculated from the positions of all of the atoms and is insensitive to these issues. The FT specifically used here is discussed in Section 5.4.3.1.

The lattice constant, determined every picosecond, is averaged which is then used as the initial lattice constant for a second otherwise identical simulation.

This second simulation has a significantly smaller oscillation around its mean due to the initial state being closer to the equilibrium. The average lattice constant from this second simulation is then used for the shock simulations. This process was repeated for each potential and both temperatures, however it was found that, within the uncertainty of this calculation, the lattice constants were the same for both potentials for each temperature.

The lattice was orientated such that the [111] direction corresponded to the z direction of the simulation box. The $[1\bar{1}0]$ and $[11\bar{2}]$ directions corresponded to the x and y directions respectively. Orienting the lattice in this way preserves the cubic lattice as these crystal directions form a mutually orthogonal set. The choice of using this crystal orientation is somewhat arbitrary due to rotational symmetry around the [111] axis.

A small number of simulations were done with different choices for the x and y crystallographic directions, but the bulk properties were not found to be different and so they were not investigated in detail. Work to check if the structure of the phase changed material in these alternate simulations is similar to that in the main series of simulations would be useful. This would aid in determining the physical accuracy of this MD study as rotating the crystal around the [111] axis should have no change to germanium's physical response.

5.3 SHOCK RESPONSE

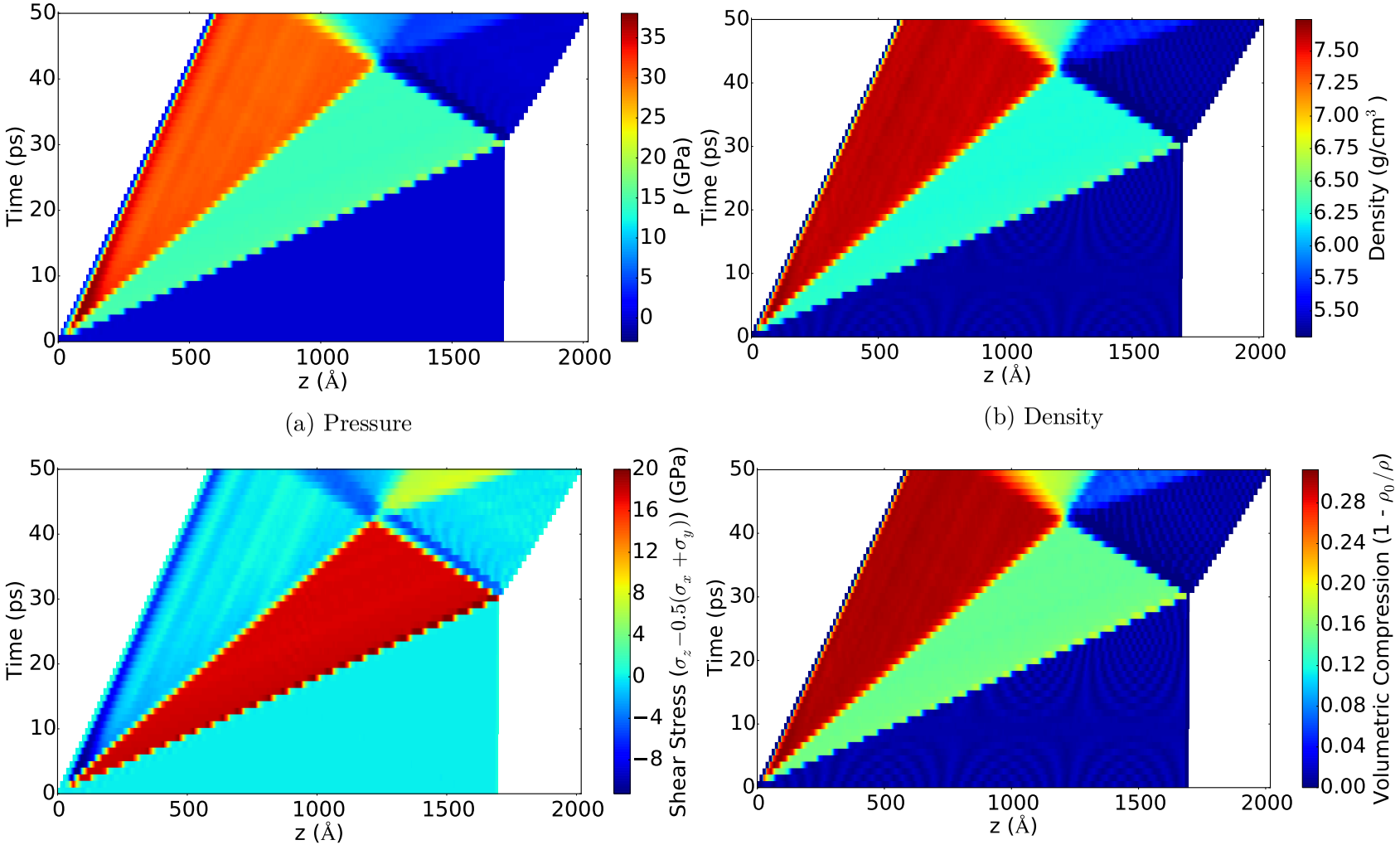
The response of germanium under shock compression in the simulations presented here is qualitatively similar to the responses seen in MD simulations of other cubic diamond materials. Figure 37 displays x-t plots of a $U_p = 1.2\,\mathrm{kms}^{-1}$ simulation and transverse side length 250 Å. A number of key bulk variables

are displayed. In this particular simulation, the pressure reaches over 30 GPa, with the material compressed by almost 30 %. For simulations which have a high enough U_p to initiate a phase transition, the response is qualitatively similar. This is true across the range of particle velocities studied and for both the MEAM and Tersoff potentials.

There is initially a purely elastic response where the shear stress very rapidly rises to over 15 GPa. This is followed by a second wave behind which there is an inelastic response. A phase transition acts to rapidly relieve the shear stress of the material as seen in Fig. 37c.

The phase transitioned material develops in bands with no evidence of defects forming in either the phase changed material or the remaining material, which remains elastically compressed. The boundaries between the bands and cubic diamond do however appear highly disordered, as can be seen in figures 42 and 43. The phase change relieves the shear stress of the material behind the inelastic wave, for both the phase changed and remaining elastically compressed material. This is consistent with studies on other cubic diamond materials [119, 142]. The structure of this phase changed material is discussed in detail in Section 5.4.

An x-t plot of the same simulation is shown in Fig. 38 where colour represents the fraction of atoms in that region that are part of phase changed material. The determination of whether an atom is part of phase changed material is performed via calculating its coordination number, this is discussed in depth in Section 5.4.1. The results of this simulation are typical of the majority of simulations where a phase change occurs, in which the second wave originates from the piston surface and propagates through the sample. Simulations with a smaller transverse size show higher variance in phase fraction but the same



(a) Pressure

(b) Density

(c) Shear Stress

(d) Volumetric Compression Ratio

Figure 37: x-t plots displaying different bulk variables of a $U_p = 1.2\,\mathrm{km/s}$ simulation.

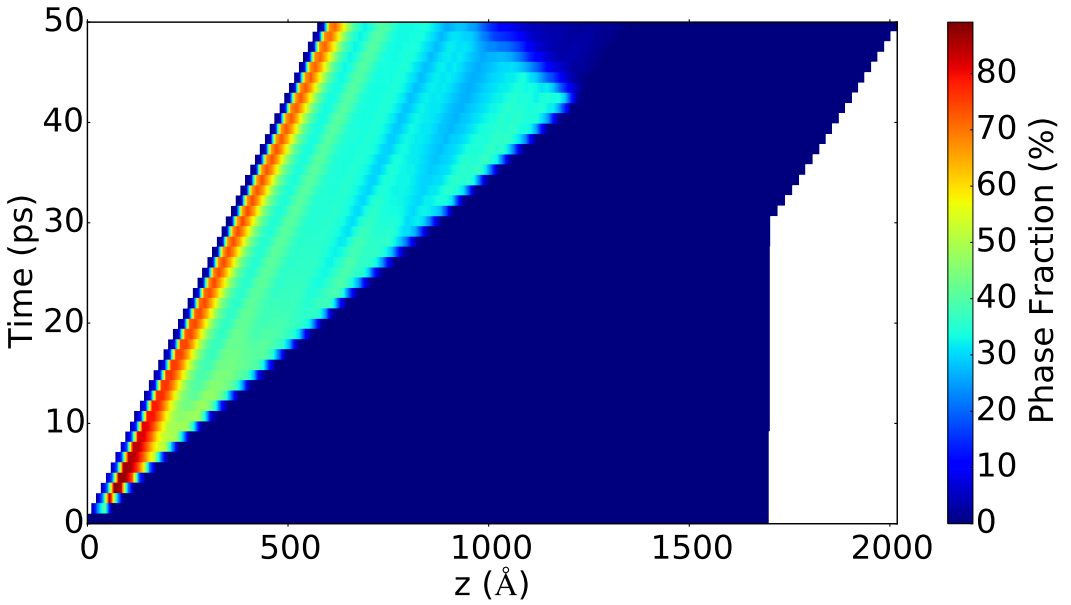
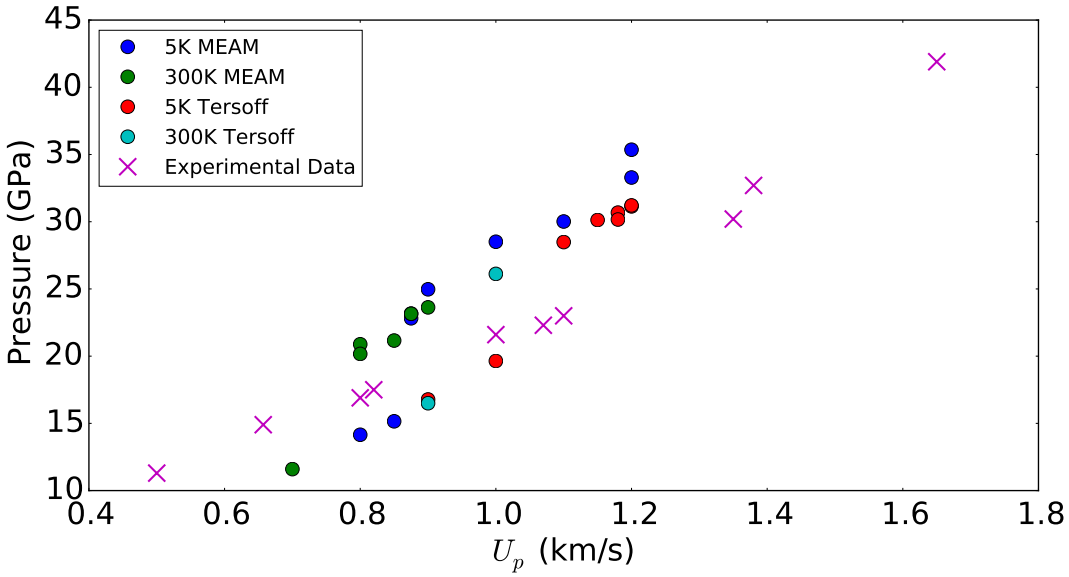


Figure 38: x-t plot of shock compressed germanium. Colour indicates fraction of atoms in that region being part of phase changed material. The warm piston method was used to create the shock with a particle velocity of 1.2 km/s. The simulation had side lengths of 25 nm in directions perpendicular to the shock direction.

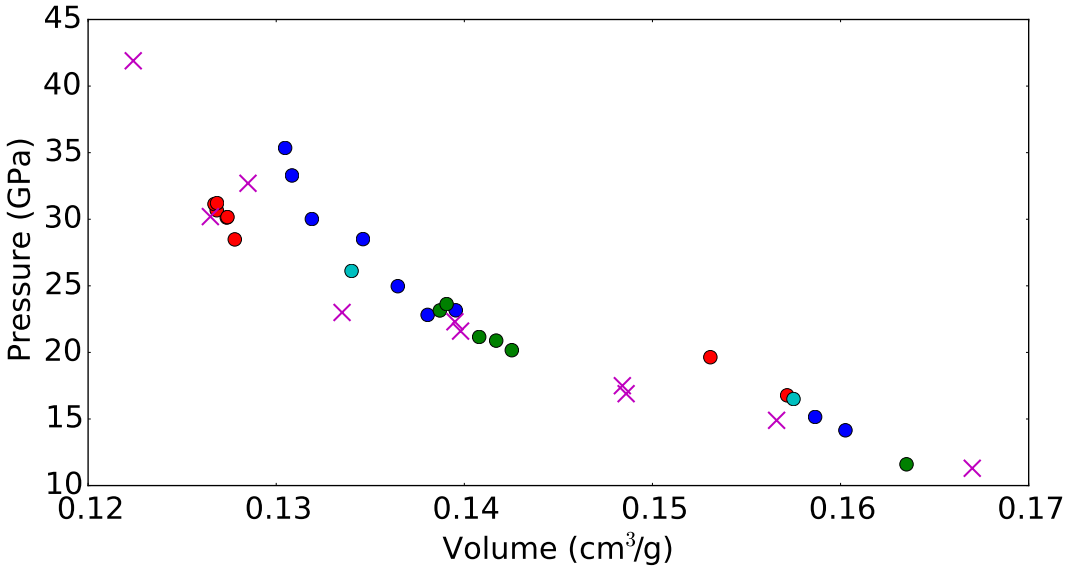
average value. The effects of simulation size are discussed in detail in Section 5.3.2.

5.3.1 *Simulation Benchmarking*

As there is no published work on these potentials' use with high pressure simulations, their response to shock compression (as described in Section 5.2.2) was compared to hugoniot data gathered from gas gun experiments. A comparison of the hugoniots of the two potentials and experimental data are shown in Fig. 39, where the pressure and density calculated from simulations have been plotted alongside results from Gust and Royce (1972) [124].



(a) P - U_p



(b) P - V

Figure 39: Comparison of hugoniots from Molecular Dynamics simulations to gas gun data [124].

For all simulations with a two wave response, the average pressure and density was calculated from a steady region of the material downstream of the inelastic wave. In simulations which did not exhibit an inelastic response, ones where the piston velocity was not high enough, the same analysis was performed for a large length of material downstream of the elastic shock front. The analysis was performed at the same timestep for all simulations, 30 ps after the launch of the shock, just before the elastic shock front reaches the rear surface. This time was chosen to prevent effects of the shock reflecting off of the rear surface from affecting the results, whilst still allowing for a large amount of material to develop behind the inelastic wave. However it was found that the results of this analysis were insensitive to the timestep in which the analysis was performed, provided that the material had reached a steady state behind the inelastic wave.

5.3.1.1 *Wave Speeds*

A significant difference between these simulations and the experimental data is the presence of only two waves in the MD simulations, whilst Gust and Royce always observe three waves for this range of particle velocities. Simulations performed at much higher piston velocities, up to $2.2\,\mathrm{kms}^{-1}$ do not show the presence of any third wave.

There is a small disagreement in the literature on the shock strength required to initiate the third wave, as Graham et. al. (1966) [148] do not observe a third wave for particle velocities below $0.6015\,\mathrm{kms}^{-1}$, whilst Gust and Royce observe the third wave at a particle velocity of $0.479\,\mathrm{kms}^{-1}$. Although this casts doubt on the actual particle velocity required to launch a third wave, it does regardless show that the mechanism which generates the inelastic waves does

not automatically produce two of them, that is to say only a single inelastic wave can be produced with a sufficiently small drive.

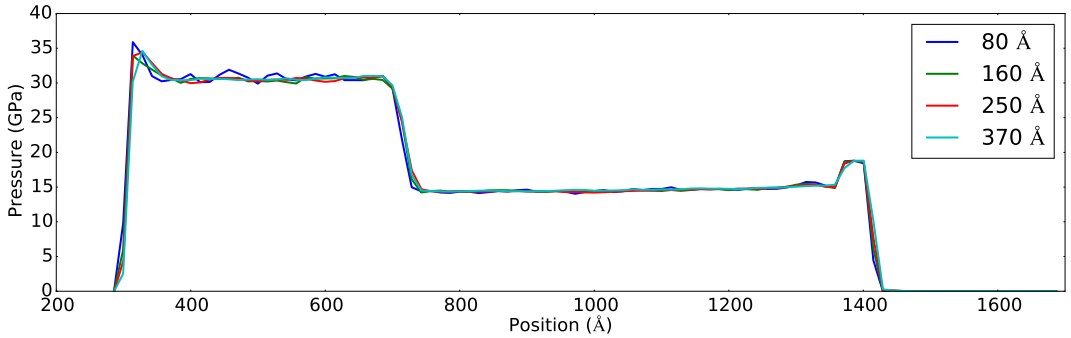
In fact, both studies agree on the point that the third wave is the result of a solid-solid phase transition and Graham et. al. suggest that the second wave is due to a transition between elastic and plastic behaviour.

An additional difference between the literature and this study, is that the onset of inelastic behaviour occurs at a markedly different point than in gas gun experiments. As discussed, a three wave structure is experimentally observed in germanium for particle velocities above $\approx 0.5\,\mathrm{kms}^{-1}$. The earliest that a phase transition was observed in this study is at $0.8\,\mathrm{kms}^{-1}$ which was seen when using the MEAM potential at 300 K.

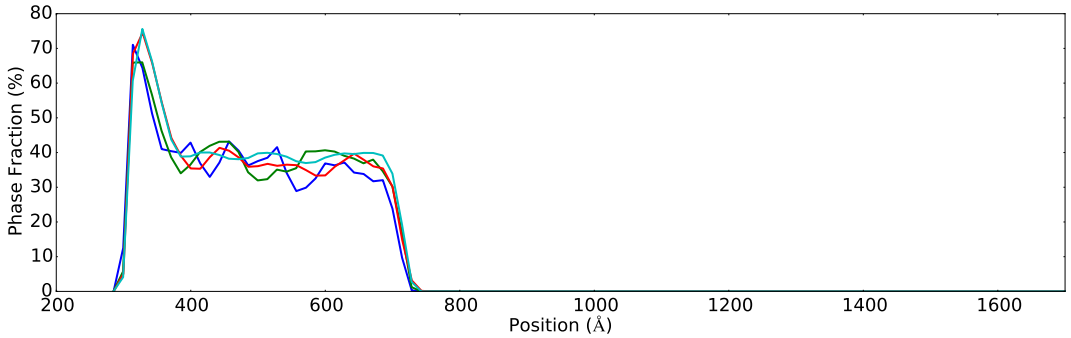
Previous MD work on germanium and silicon also required that piston velocities be significantly above those needed for gas gun experiments to initiate a phase transition [119, 141]. Choosing to simulate perfect, defect free samples may be a reason for this discrepancy, as the simulated material will have no nucleation points for the phase change. However the ready availability of near defect free samples for experimental use does not support this explanation.

It is perhaps not surprising that the simulations do not closely match high pressure experimental data, considering that the potentials used have primarily been designed to match ambient properties of germanium rather than high pressure ones. Indeed, high pressure potentials have been created for other materials indicating that it is often needed [136, 149–152]. Additionally, the difference in sample sizes (nm) and timescapes (ps) used here compared to laser experiments (µm, ns) and gas gun experiments (mm, µs) may also lead to these discrepancies.

5.3.2 *Size Effects*



(a) Plot of pressure with z position. For all timesteps, there was no significant difference observed between simulations.



(b) Plot of phase fraction with z position.

Figure 40: Wave profiles for a simulation 24 ps after the shock has been initiated. The legend indicates the transverse side length of the simulation.

The mechanisms responsible for defect generation and phase transitions in MD simulations remain an area of active research interest. Kimminau et al. (2010) discuss the influence of simulation size and its effect on available phonon modes in simulations [153]. Although the specific effects remain an open question, it is clear from their work that the size of a simulation can have a significant effect on how a simulation will evolve.

In an effort to investigate this, a number of simulations were performed at 0.8 and 1.2 km/s with different transverse dimensions but otherwise identical initial parameters. The smallest simulations had a transverse length of 8.5 nm,

with the largest having a side length of 37 nm and were comprised of over 10 million atoms. For simulations at the same piston velocity, bulk properties such as pressure and density were not found to vary with simulation size. Figure 40a compares the pressure profiles of four simulations for a single timestep where U_p is 1.2 kms^{-1}. There is no significant difference, in bulk properties, between these simulations at any timesteps. However the smallest simulation does appear to have a more variable pressure, which is unsurprising considering it is being calculated from many fewer atoms. This behaviour is also seen for other variables.

The nature of the bands within the phase-changed region of the smaller simulations, specifically the creation of fewer bands discussed in Section 5.4.2 and specifically seen in Fig. 43, means that properties such as phase fraction vary to a greater extent than other variables. One section in z can be dominated by a single band whilst a neighbouring one can have almost no phase changed material within it. This still relieves the shear stress in the inelastic region, inhibiting any further phase change, but leads to the highly variable phase fraction which is observed. The larger simulations generate more bands and so are less sensitive to this effect. Therefore the same variance in phase fraction does not occur.

Whilst bulk properties appear to be insensitive to transverse simulation size, the nature of the phase changed material is significantly altered. It appears that when using the smallest simulation dimensions, fewer bands of phase changed material develop. This is shown in Fig. 43 where only atoms with coordination number greater than 12 have been drawn.

5.4 PHASE CHANGE

The structure of the phase changed material is key to understanding the inelastic region in this study. Diamond anvil studies have shown that germanium undergoes a phase transition to the β-Sn structure under hydrostatic compression. However, there has been no published diffraction work to determine the structure of germanium, following a phase transition, in a dynamic compression experiment.

Molecular dynamics simulations provide an ideal platform with which to study the details of this phase change. This is principally due to MD simulations providing the full time history of each atom as the material is compressed.

5.4.1 *Coordination Number*

A quantity that was of particular use in this study was *coordination number*. Specifically, the coordination number of an atom is here defined as the number of other atoms that are within a certain distance of the original atom in question. The work here uses a cutoff radius of 4.0 Å.

It is important to note here that this work uses the definition of coordination number as used in LAMMPS and the molecular dynamics field; it does *not* refer to the number of nearest neighbours of an atom which is its typical usage in condensed matter science. Whilst it may be more appropriate to think of this quantity as local number density, which is less ambiguous, it will be referred to as coordination number to maintain consistency with the molecular dynamics definition.

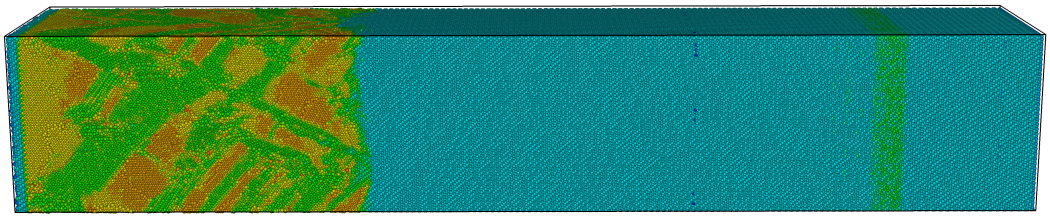


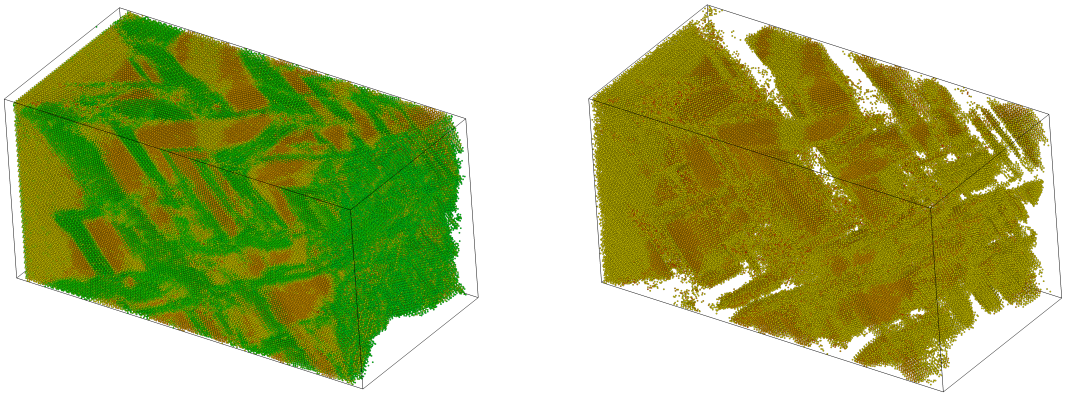
Figure 41: 3D render of all atoms from a single timestep where the shock is moving from left to right. The atoms have been coloured by coordination number. This snapshot is taken 26 ps after the shock was initiated, from the same simulation displayed in Fig. 37.

Separating atoms by coordination number was found to be an extremely robust method of distinguishing between atoms comprising phase changed material and others. This is likely due to coordination number being restricted to integer values; whilst other continuous metrics such as stress or potential energy (which were also tried as methods of identifying and separating phase changed material) did not preform as well.

The use of coordination number here follows the analysis of Lane and Thompson [141], who also found that it was an effective method for identifying phase changed material for a wide range of simulation parameters.

5.4.2 *Band Structures*

Figure 41 is a 3D render of all the atoms from a timestep in the simulation first shown in Fig. 38. In this figure, the shock is moving from left to right and the initial elastic wave is part way through the simulation box. The atoms have been coloured by coordination number and there is a clear divide between atoms behind the inelastic wave and those ahead of it, which have only been elastically compressed.



(a) Phase changed region of MD simulation in Fig. 41. Only atoms with coordination number $\geqslant 8$ are displayed.

(b) In order to highlight the bands of phase changed material, only atoms with coordination number > 12 are shown.

Figure 42: 3D render of atoms from the same timestep as Fig. 41 where only atoms in the phase-changed region have been shown.

Atoms in both uncompressed and elastically compressed material have coordination numbers of 4; whilst atoms that are behind the inelastic wave have coordination numbers greater than 8. Atoms at the shock front can have coordination numbers of up to 5 or 6. The material behind the inelastic wave, the *phase-changed region*, is highly disordered with multiple, inter-penetrating bands of material forming very rapidly. These bands can be further highlighted by rendering only atoms with coordination number greater than 12. It should be noted that the vast majority of atoms in the bands have coordination number equal to 13 or 14, and only a few hundred atoms have coordination numbers higher than this.

Using these values of coordination number to separate the different types of material (elastic and inelastic regions) is consistently effective for all the piston velocities used here, for both the Tersoff and MEAM potentials.

This is shown more clearly in Fig. 42b where the image shows the fragmented and disordered nature of the phase changed material. In particular, this simu-

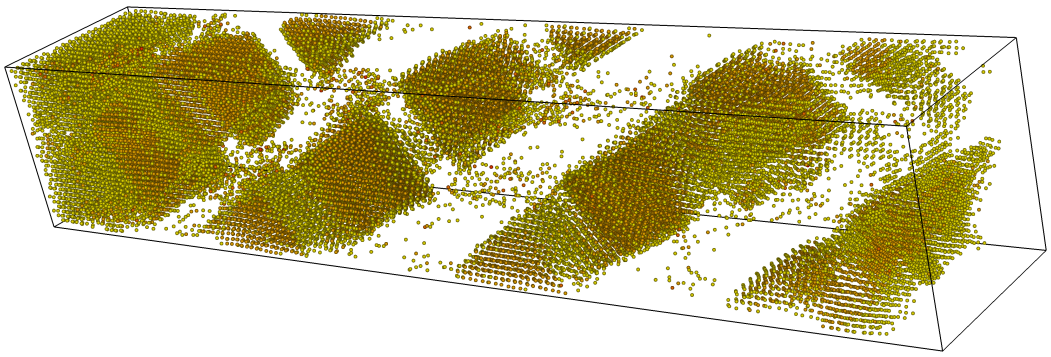


Figure 43: 3D render of atoms from the same timestep as Fig. 42 but for a simulation with smaller transverse size. Only atoms with coordination number greater than 12 have been displayed. A single band structure is shown although it is not continuous and shows a repeated breaks.

lation indicates that a large fraction of the material behind the inelastic wave is comprised of phase changed material. This is consistent with Fig. 38 where over 30 % of the phase-changed region is comprised of phase-changed material.

In order to more easily investigate the structure of the phase changed material, a simulation where only a single band of material has developed would be of tremendous help. In order to encourage this, a simulation was performed which was only 8.5 nm in the x and y dimensions. The effect of simulation size has been discussed in Section 5.3.2. While less physical, a simulation with smaller transverse size can hinder the formation of mutiple bands.

This intentionally small simulation is shown in Fig. 43 where the transverse simulation size is only 8.5 nm. This figure shows that only a single band has developed, although there are repeated breaks along it's length. The band wraps around the simulation edges as would be expected from the periodic boundary conditions in the transverse directions.

The band that has formed in this simulation, whilst still disordered (in that it is not continuous), shows a much more coherent structure than the larger simulations, and is therefore far easier to analyse. Primarily this is due to no

interpenetration of bands which is the main hindrance in analysing the lattice structure of the phase changed material in larger simulations.

The characteristics of the bands and their exact dependence simulation size, remains an open question. The previous work discussed in Section 5.1 also leave this as an area of further work. One potential reason is that the required change in unit cell is an absolute amount that does not depend on simulation size, but it's effects can vary depending on the simulation size. This would mean that a small band could relieve shear stress in the simulation but in larger simulations more material must change phase. Further investigation would be required to explore this.

This process was repeated for the Tersoff potential and a similar render is shown in Fig. 44. This potential shows a similar single band appear however there are a number of differences. Foremost is that behind the formation of the initial band is a highly disordered region which upon visual inspection looks similar to shock melting. This region does not show significantly different bulk properties compared to upstream material, that is to say there is no significant change in quantities such as pressure or density. Whilst surprising, this also indicates that it is not similar to the third wave seen in gas gun work. In addition the single initial band is significantly more disordered than the band shown in Fig. 43. This makes identifying the structure of this material extremely challenging.

5.4.3 *Unusual Phase Transition Location*

There is one unusual set of simulations where the phase changed region does not initiate at the piston surface and instead begins at the elastic shock front

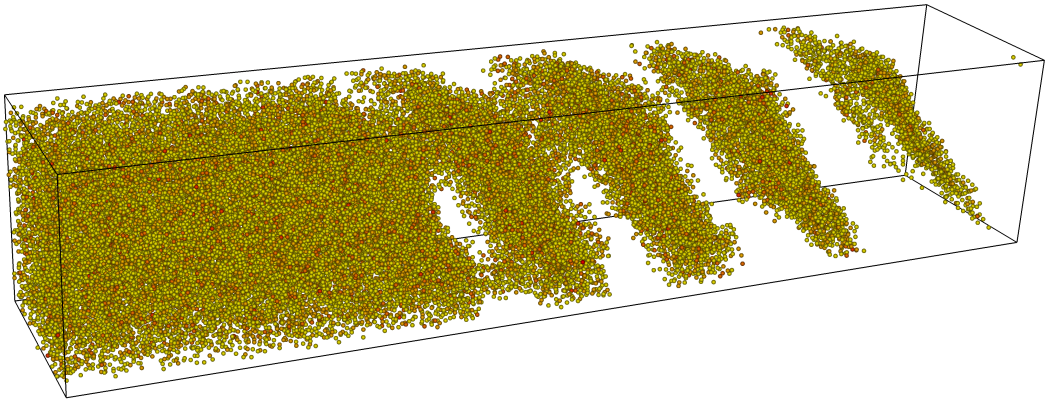


Figure 44: 3D render of atoms from a similar simulation to Fig. 43. In this case however, the Tersoff potential was used showing a qualitatively similar single band structure with no breaks in continuity.

some time after the front starts to propagate. This was seen with the MEAM potential with a piston velocity of $0.8\,\mathrm{kms}^{-1}$, initial temperature of 300 K and transverse size of 8.5 nm. An x-t plot of this is shown in Fig. 45. This simulation was repeated with different setup parameters such that the initial microstate of the simulation was different but the bulk properties remained unchanged. By changing the initial microstate, the phase change was initiated at different times. Although when delayed, it always occurred at the elastic shock front rather than at the piston surface for as in other simulations. What causes the delay in the onset of the phase change remains unknown, but this shows it does at least depend on the initial microstate of the simulation. Further investigation of this could lead to insight into how the phase change is nucleated.

5.4.3.1 *Experimental Comparison*

The highly disordered nature of the phase changed material will have a significant effect on the diffraction signal that it can create. Without yet knowing the

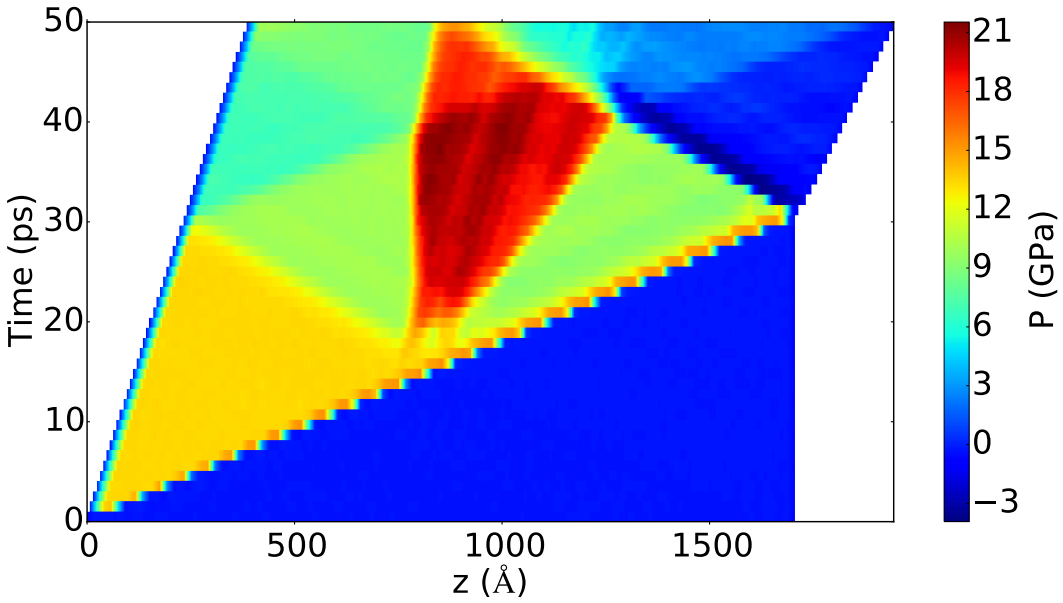


Figure 45: X-t plot of shock compressed germanium where phase changed region starts at shock front some time after the simulation has begun.

structure of the material, a Fourier Transform (FT) can predict the position and intensity of diffraction signal. The FT here is defined as:

$$I(\mathbf{k}) = \left| \sum_{n}^{\text{all atoms}} \exp\left(\frac{2\pi i \mathbf{r}_n.\mathbf{k}}{a_0}\right) \right|^2 \tag{72}$$

which is a non-uniform FT of all the atom positions of the material that is being investigated.

This has been done in Fig. 46 where high intensity points the FT of the atoms in Fig. 43 are shown. Additionally the volumes of reciprocal space that the SHiELD experiment - discussed in Chapter 4 - is sensitive to, have been highlighted. Importantly these volumes do not encompass the high intensity points of the FT, which are themselves significantly less intense than an FT of static or elastically compressed material. Therefore it is not surprising that the phase changed material was not observed in the SHiELD experiment, as it does not diffract efficiently in this geometry. Either a more judicious choice

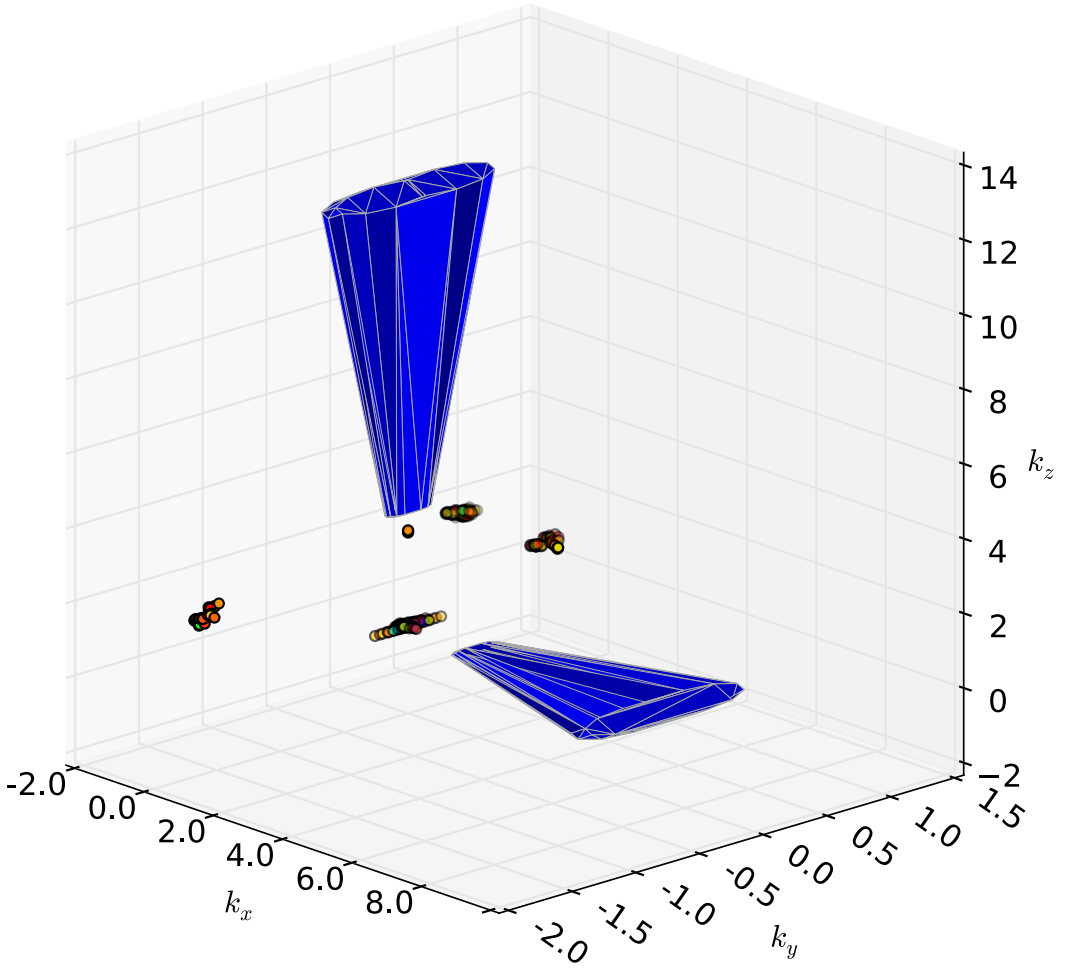


Figure 46: 3D fourier transform of phase changed material. Points in the FT with high intensity are shown as coloured circles. Note than none of these circles are within the SHiELD sensitivity volumes which are coloured blue.

of detector location or an alternative technique would be more sensitive to detecting this material. In particular, XFEL experiments have had recent success with diffracting from shock compressed silicon and silicates; a similar geometry could also be effective at investigating germanium [154].

5.4.4 *Phase-changed Structure*

The structure of the phase-changed material is of extreme importance, as it is key in predicting the diffraction pattern of the phase changed material. The structure would determine both which diffraction peaks would be present as well as where they are likely to be, based on the symmetry and size of the new lattice respectively. Prediction of the new lattice would therefore greatly aid in planning experiments seeking to observe the new phase.

The key analysis technique used in this analysis is the *3D Pair Correlation Function* (3dPcf). This has been used previously by Higginbotham et al. [136] in determining the twinning mechanism in tantalum MD simulations.

The 3dPcf, $g(\mathbf{r})$ can be calculated by,

$$g(\mathbf{r}) = \sum_{i}^{\text{all atoms}} \sum_{n} \delta(\mathbf{r}_n - \mathbf{r}_i - \mathbf{r}) \tag{73}$$

where the second summation over n is over the neighbours of the atom i within a cut-off radius (in this case 4 Å was used). This calculation retains directional information over the more commonly used scalar calculation of the pair correlation function. The 3dPcf is calculated by determining the vector between each atom and other neighbouring atoms, within the cut-off, which are then binned on a 3D grid. The values of this 3D grid can then be displayed giving a representation of the unit cell.

The 3dPcf has lower signal to noise than FT based methods, as with FT techniques the intensity scales with the square of the number of atoms and not linearly as the 3dPcf does. However the much higher computational cost of FT methods makes using the 3dPcf advantageous for fitting the unknown structure.

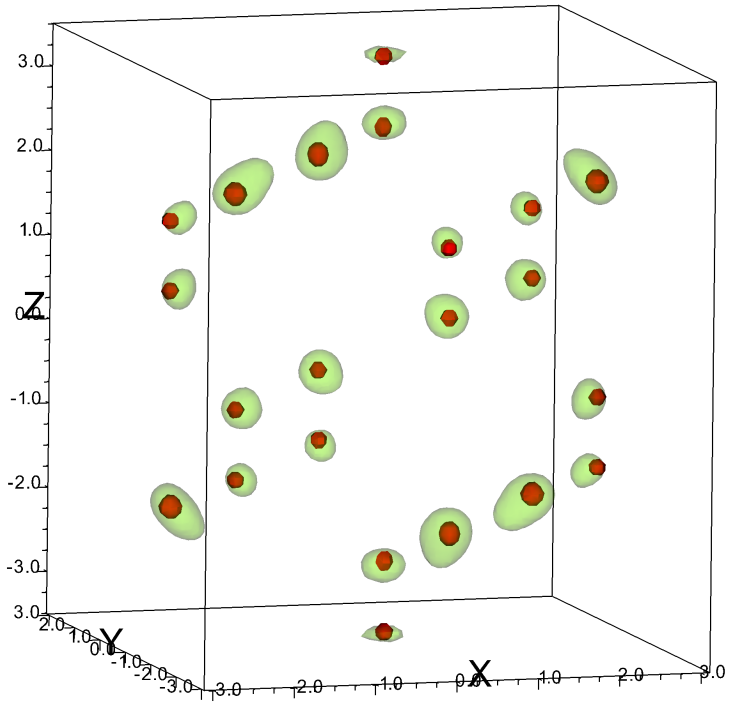


Figure 47: 3D render of the 3D Pair Correlation function for the atoms shown in Fig. 43. The transparent green volumes show the 3dPcf calculation for the atoms in the MD simulation. The solid red spheres show the 3dPcf for a near perfect lattice that has been fitted to the 3dPcf calculated from the MD. The structure of this lattice is discussed in Section 5.4.4.1.

Figure 47 shows the result of the 3dPcf calculation for the single band shown in Fig. 43 as the transparent green volumes. In addition, the 3dPcf of a fit to this phase changed structure has also been plotted and is displayed as the solid red spheres. The details of this structure are discussed below in Section 5.4.4.1. There is close agreement between the fitted lattice in red and the calculation from the MD in green which suggests that the fit is accurate.

The 3dPcf was also calculated from the atoms comprising the single band region of Fig. 44 where the Tersoff potential was used. Unsurprisingly, the 3dPcf is significantly more disorganised and it wasn't possible to find a similar fit for the unit cell in this case. However the highest intensity points at the corners

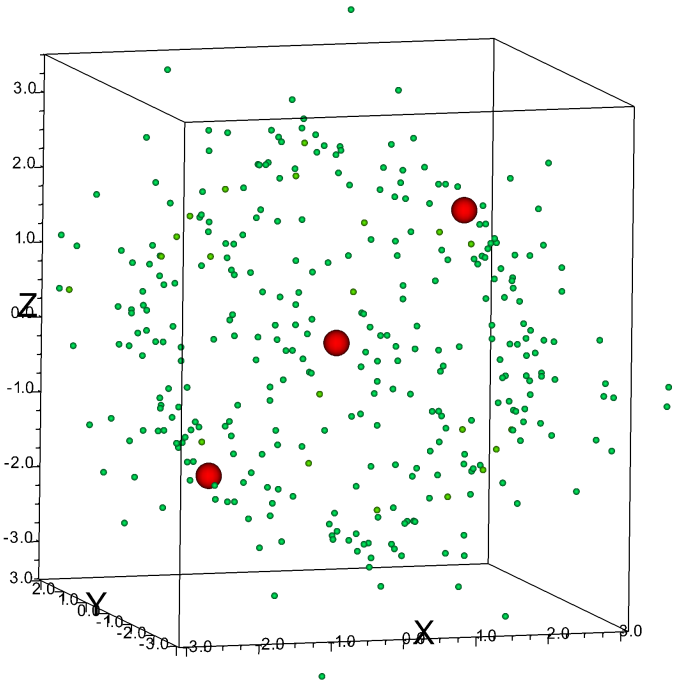


Figure 48: 3D render of the 3D Pair Correlation function for the atoms shown in Fig. 44 but using only atoms from the single band. The highly disordered nature of the atoms in the band makes this 3dPcf much more difficult to analyse. The red spheres are very high intensity points which can be used to calculate the unit cell dimensions.

of the plot (displayed as the larger red spheres) which appear as a result of neighbouring unit cells, allow for the unit cell dimensions to be determined. They indicate that the lattice has been compressed by 40 % along [111] and then rotated 12° around the x-axis, corresponding to the $[1\bar{1}0]$ in the original cubic diamond lattice.

The 3dPcf was found to be disordered when calculating it for larger simulations, such as the one shown in Fig. 42. The more complex band structures there remain a challenge to fully analyse. Although, it is likely that individual bands are comprised of very similar structure to the one found here, a combination of differences in rotation angles and directions, along with the fact that the bands inter-penetrate each other make the analysis challenging.

5.4.4.1 *Unit Cell Parameters*

Figure 49 details the structure of the phase changed material. In summary, there is a 40 % compression in the [111] direction, along with 10 % expansion in the $[1\bar{1}0]$ and $[11\bar{2}]$ directions (the transverse directions). The basis atoms, highlighted in red, move 1.06 Å in the [111] direction. There is also a small rotation 2.5° anti-clockwise around the $[1\bar{1}0]$ direction. The 10 % transverse expansion is not matched by a similar compression in the remaining elastically compressed cubic diamond material within the inelastic region. This implies that the highly disordered boundary material is compressed in the transverse direction, in order to conserve space which is a constraint of the simulation.

This structure is not simply a resizing and rotation of the original cubic diamond unit cell, as was the case in the work of Mogni et al. concerning silicon. Here there is an additional movement of the basis atoms along the [111] direction, the shock direction, which is a more drastic change in the unit

cell. This shows a large advantage of using the real-space analysis of the 3dPcf, as the initial fit was found by trial and error movement of atoms. Knowing the target positions of atoms in real space was of great benefit when performing this analysis.

This structure is highly unusual due to the fact that it requires the movement of atoms along the [111] axis. Whilst the known phase transitions from cubic diamond to β-Sn, Imma or simple hexagonal are a result of similar movements along [001]; it is these same same basis atoms that are moving in both this study and these known transitions. These space groups are related to each other by movements of only the basis atoms along the [001] direction to go from cubic diamond to β-Sn. Different unit cell side lengths change the unit cell to Imma. Further movement of the basis atoms so that they are in line with the other atoms in the unit cell results in a simple hexagonal structure.

The space group describes the symmetry of the crystal system and can be used to predict aspects of the electronic band structure of a material. Of note is that the space group of this new structure is the same as cubic diamond that has been uniaxially compressed along [111] i.e. the phase change does not change the symmetry of the unit cell. Specifically this space group is $R\bar{3}2/m$ which was determined using the FINDSYM code [155].

As there has been little diffraction work on shock compressed germanium along [111], it is perhaps plausible that this phase change does occur under dynamic compression. Alternatively it could be due to the constraint of atoms in the simulation to be bound to a relatively small transverse region; one that is significantly smaller than typical drive areas in experiments. This limitation can inhibit large rotations of the lattice in the simulations, and so shear stress must be relieved via a different mechanism. As the shock is applied along [111],

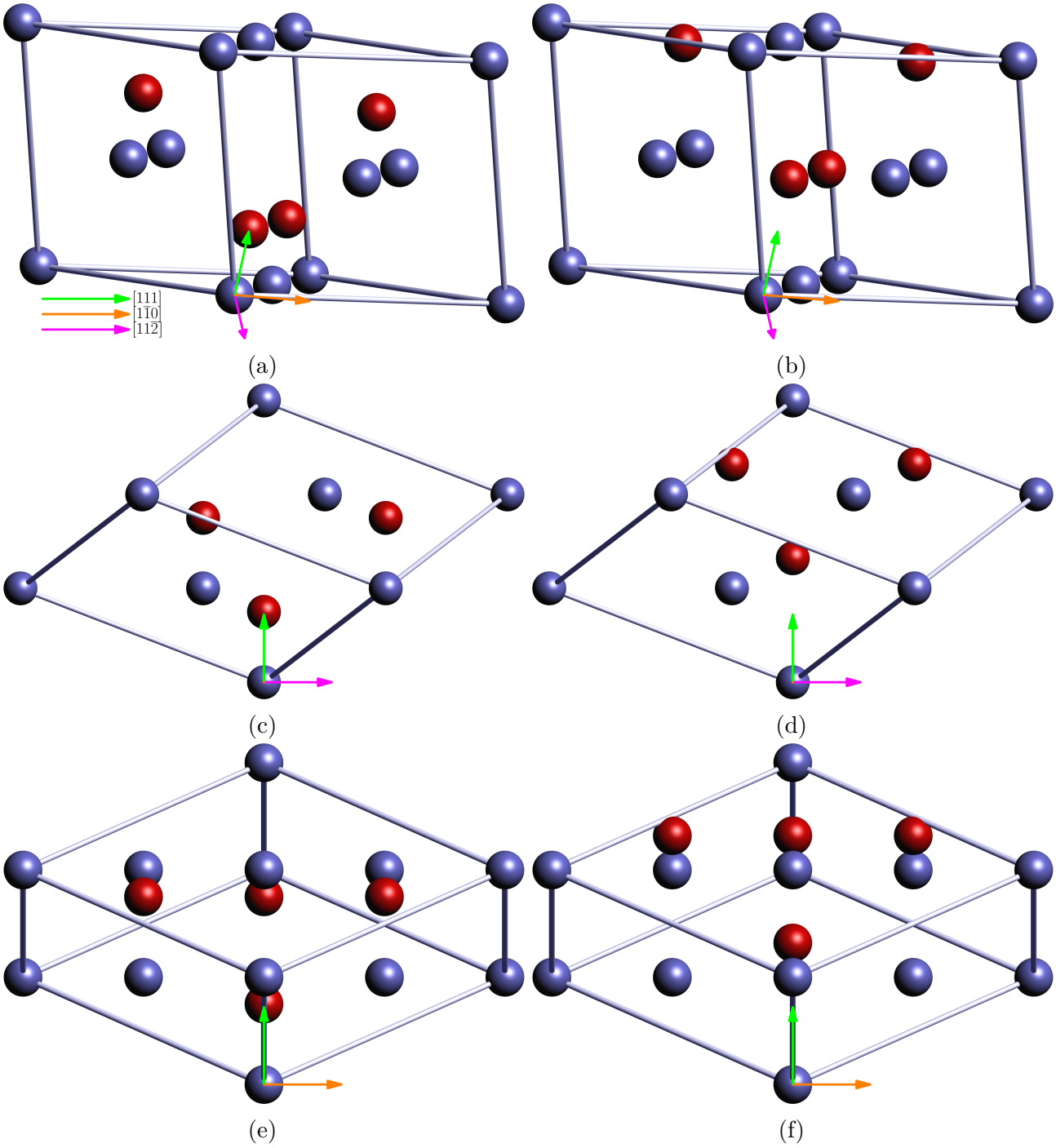


Figure 49: Diagrams of cubic diamond and phase-change structure alongside for comparison. The middle and bottom row show the unit cell with [111] aligned with the vertical of the figure. Left: Cubic diamond structure. Right: Phase-changed structure where the red basis atoms have been moved along [111] by 1.06 Å. Both structures have been compressed along [111] and expanded along [1$\bar{1}$0] and [11$\bar{2}$], which results in the skewed appearance of the unit cell.

it is perhaps unsurprising that the basis atoms move along [111] as movement in perpendicular directions is highly constrained due to the simulation boundaries.

As noted previously, the 3dPcf was not effective for analysing the Tersoff simulations and so this same analysis was not completed for those simulations.

5.4.5 *Potential Stability*

Considering the surprising unit cell parameters discussed above, the effectiveness of the potential at exhibiting known phase transitions was investigated. In order to do this, a series of simulations were set up where there was no shock applied. Instead, a cubic sample was generated in a known strain state and the potential energy of that sample was calculated using LAMMPS. This strain was applied along the axes of the simulation box i.e. [111], [$1\bar{1}0$] and [$11\bar{2}$]. Importantly the atoms are unable to move from their initial positions in order to maintain the structure of the material. The results of this are shown in Fig. 50.

Here we clearly see that while there is a large minimum at ambient conditions, there is no separate minimum for β-Sn. This indicates that the potential, when compressed along the simulation axes - which includes uniaxial compression along [111] - is unstable. Atoms will either become free, i.e. the sample melts, or they will move, as they have in the shock simulations discussed in this study. Note that β-Sn is stable when compressed along [001] as shown in Fig. 51 where a second local minimum is seen at the bottom edge of the figure.

As seen in the previous section, the basis atoms move along [111]. This extra shift in atomic positions is also replicable in LAMMPS and a similar energy surface can then be generated using this structure. The atoms have been moved

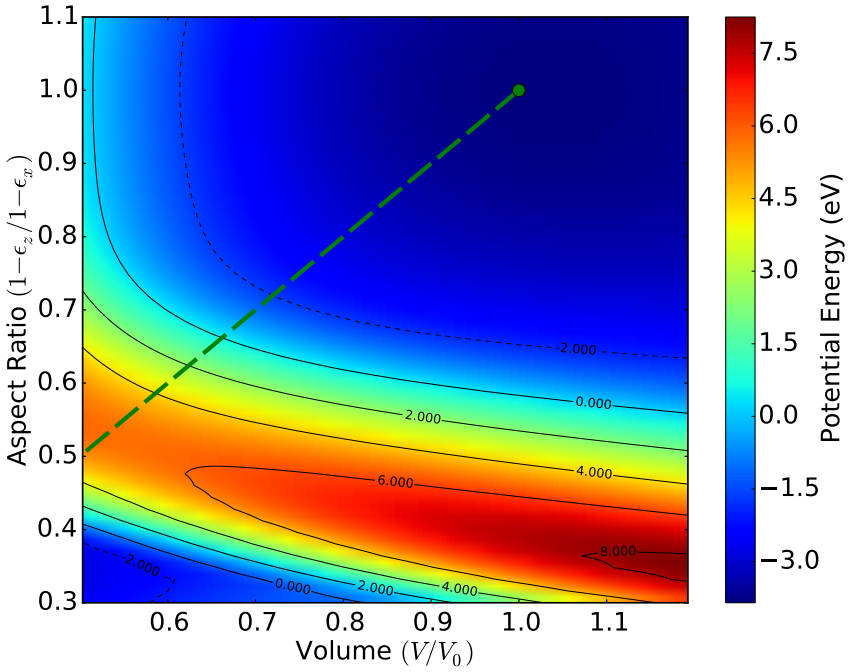


Figure 50: Potential energy surface plot of the MEAM potential for a large range of strain states, where strain is aligned along [111], [1$\bar{1}$0] and [11$\bar{2}$]. The green dashed line indicates the path taken under uniaxial expression starting from the ambient unit cell.

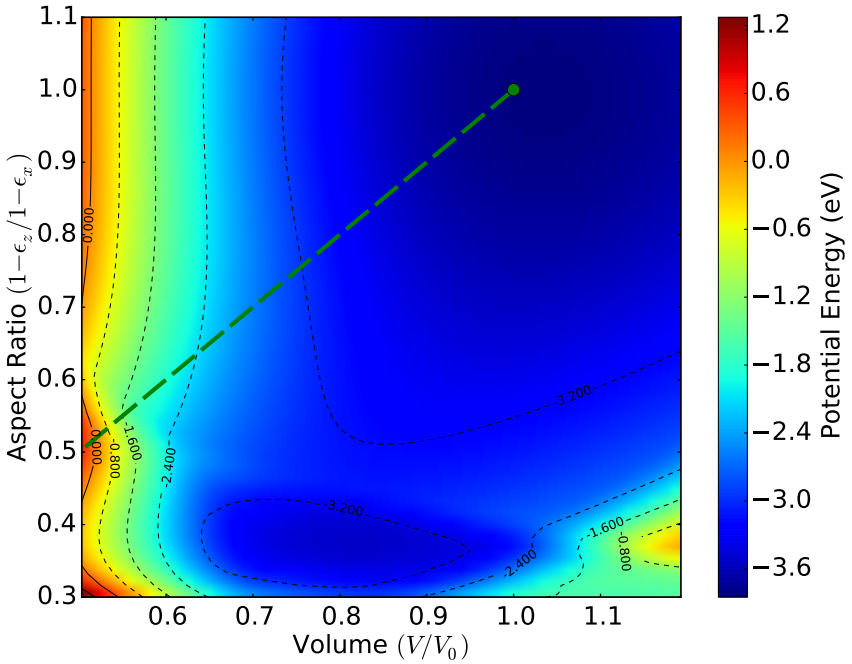


Figure 51: Potential Energy plot of the MEAM potential for a large range of strain states, where strain is aligned along [001], [100] and [010].

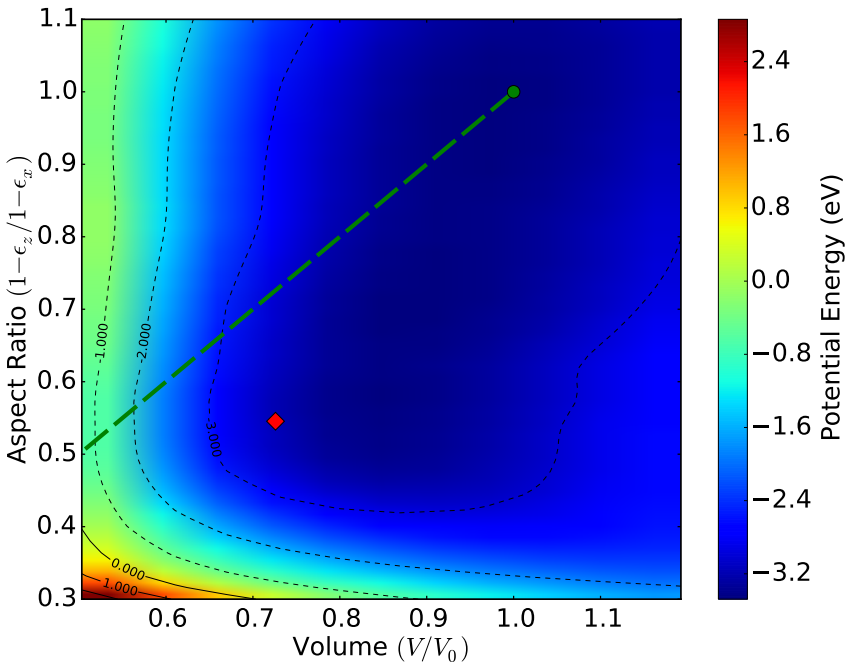


Figure 52: Potential Energy plot similar to Fig. 50 but with the basis atoms moved along [111] for the phase changed unit cell. The red diamond indicates the location of the phase changed material described in section 5.4.4.1.

so that they lie at the same unit cell positions as described in Section 5.4.4.1. This is shown in Fig. 52.

In contrast to Fig. 50, there is no longer just a single minimum which corresponds to ambient conditions. Note that the potential energy minimum at static conditions of the phase changed structure (Fig. 52) is higher (less negative) than the energy surface with no atomic shift (Fig. 50). This is consistent with the potential being stable in the cubic diamond structure at ambient conditions. The extra minima in this energy surface indicate that the structure, with shifted basis atoms, is energetically favourable when significantly strained.

Whether this structure is just an artefact of the potential or of the simulation properties is unclear from this study alone. Performing a significantly larger simulation where large scale rotation is possible could be a fruitful method of investigating this, along with experimental verification.

5.5 CONCLUSION

There has been very little published work on Molecular Dynamics simulations of shock compressed germanium. The work in this chapter therefore represents the most thorough study of this subject. The comparisons to experimental shock work indicate areas where the potentials could be improved. In addition, the nature of the bands of phase changed material are investigate in detail, and some qualitative behaviour of these bands with simulation size is discussed. Understanding the effects of simulation parameters is key to taking simulation work forward and applying it in real experiments or macroscopic models. Furthermore, the structure of the phase changed material (which had not been identified previous to this work) has been discussed in detail using a method not widely used elsewhere. It was found to be significantly more useful than standard FT techniques, and is a good potential analysis method that could be used on other cubic diamond materials or with other structures.

6

CONCLUSIONS

6.1 SINGLE PHOTON ENERGY DISPERSIVE X-RAY DIFFRACTION (SPEDX)

While advances in high power lasers continue to push the intensity and pressure frontier in high energy density physics, diagnostics must be improved and developed to match the increasing demands of these experiments. SPEDX is a diagnostic which aims to perform in-situ x-ray diffraction, with the intention of mitigating many of the problems inherent to performing experiments at the largest laser facilities.

It utilises one, or more, CCD cameras in single photon mode to detect x-rays diffracted from a sample. CCD cameras have previously been used in single photon mode during laser-plasma experiments. However, they have never been used before to record diffraction; the work presented in this thesis is the first use of this technique.

The initial experiment, at the Janus laser in 2012, was successful as a proof-of-principle experiment. It showed that powder-diffraction could be measured using a CCD, with a white-light backlighter. Both these requirements result in a weak diffraction signal and so successfully detecting the signal on a CCD, whilst still using a relatively modest laser facility, is encouraging.

A photon-mapping Monte-Carlo simulation code, to help plan and analyse SPEDX experiments was developed. This code in particular, focussed on faithfully simulating many of the relevant physical processes that lead to the CCD measuring measuring photons. This includes photon interactions with the target, relevant filtering and detector. The good agreement between the results of these simulations, both of diffraction signal and fluorescence, is reassuring; it shows that the code can be a useful tool in supporting SPEDX experiments.

Subsequent efforts at the Vulcan laser in 2013 showed an improvement in diffraction signal from undriven targets. Use of multiple CCD cameras in a single experiment along with a refined backlighter design greatly improved the signal to noise of the technique. However using the technique with driven targets proved to be significantly more challenging. Whilst diffraction from driven material was observed, further analysis of the data showed that the inferred material state was not consistent with current models of material responses. Specifically this refers to observing more transverse than longitudinal compressive strains. Recent XFEL experiments performed on tantalum, the same material that was investigated during the Vulcan experiment, showed that grain rotations and slip can give rise to a highly complex material response, one that is not described by a simple diagonal deformation tensor [156]. However, even with this material model, it would not give rise to observing larger transverse than longitudinal strains.

Placing cameras at significantly different scattering angles, for example in transmission, would be of benefit to this experimental setup. By having a significantly larger difference in scattering angles between the two cameras, they will be sensitive to different parts of the strain state of the material. Recording measurements in transmission also mitigates issues with drive noise as the sam-

ple itself will attenuate much of it. Performing diffraction in transmission does require using thin samples, which creates additional experimental difficulties.

An issue with SPEDX is that the CCDs are small and placed a significant distance away from the sample. This results in the cameras subtending only a small solid angle, in stark difference to image plate based techniques which can cover close to 2π. Moving CCDs closer to the sample or using large area detectors, could help alleviate this issue. Of course, this negates a key benefit of SPEDX where the diagnostic is a sizeable distance from the interaction zone, which reduces the impact of noise.

Further investigation of the limits of how close a CCD can be to the sample, whilst still being in single photon mode and surviving would be beneficial. However covering a larger solid angle, instead by use of many more cameras, would also be of great use in dealing with the issue of texturing; which has been shown to be a potentially significant issue at the highest pressures in recent diffraction work at the NIF.

Other improvements include using higher energy backlighters and recording diffraction at small scattering angles. Both of these would allow for measuring diffraction at higher energies and from higher order lattice planes. The effects of the limited spectral resolution are a smaller issue as the energy is increased, although the quantum efficiency of the CCD does fall off significantly after 10 keV; therefore requiring a suitably brighter backlighter. This could be facilitated by using a large laser facility where plastic capsule implosions are available, which are extremely bright white light x-ray sources. Performing diffraction at higher energies would also allow for harsher filtering to be used. This would allow the effect of drive noise to be significantly reduced.

Whilst SPEDX has been shown to work in principle, further refinement is needed before it is to be widely adopted.

6.2 SINGLE HIT ENERGY RESOLVED LAUE DIFFRACTION (SHIELD)

Intended as an enhancement of the existing Laue platform, SHiELD utilises a CCD camera to resolve the energy of a Laue reflection. This measurement, along with the Laue pattern recorded from image plate, can be used to measure the unit cell volume and aspect ratio simultaneously from the diffraction signal alone. The use of multiple cameras can enable this measurement without the use of image plate at all. This can be of significant benefit for a high shot rate experiment, where the use of solely electronic diagnostics can significantly increase the rate of data collection.

Careful choice of which Laue spots are recorded by the CCD means that the existing Laue platform is not compromised. In the case of the experiments presented in this thesis, the spots did not move under compression. These diffraction spots typically have little use when analysing image plate data; as it is the shift in spot position which is usually most important when interpreting Laue diffraction patterns. However the energy resolving ability of the CCD allows a great deal of additional data to be gathered from a single Laue spot.

In this work, the Laue spot was used to determine volumetric compression of both silicon and germanium. Further analysis allowed precise backlighter timings to be inferred, and along with VISAR measurements, a more in-depth study of the material response of silicon; which would not have been possible from a single laue spot recorded on image plate. This material response was

found to be consistent with other experimental and simulated shock compression work on silicon.

The later study of germanium using SHiELD was less successful, in part due to the lack of VISAR measurements. In addition the lower phase transition pressure, and correspondingly lower HEL, meant that diffraction signal from the driven germanium was more difficult to resolve. A small degree of automated analysis was employed in analysing the SHiELD data from germanium. Analysis of this kind will become more prevalent in the future, especially at facilities such as the European XFEL; where high repetition rate lasers will allow for extremely rapid shot rates.

Similar to SPEDX, a clear route for improvement is using a higher energy backlighter. Whilst the high signal to noise, inherent to the Laue technique, makes drive noise less of an issue; measurements from higher order lattice planes would allow for more precise measurements of lattice structure. This would aid in resolving small strains such as those found in germanium.

Further improvements include using cameras in positions that are sensitive to material responses that are more complex than a transverse and longitudinal strain. The high sensitivity of the Laue technique and the CCD cameras mean that detecting diffraction signal from small disordered regions may be possible. For example, the thin bands of phase changed material in silicon and germanium, that have been predicted by MD simulations. Careful choice of camera positions and experiment geometry could allow for a direct observation of this material and its structure.

The technique could also be used for measuring the degree of plasticity in materials such as tantalum or copper. This would also be a good validation of

the technique, as it has not yet measured transverse strain although this was expected when considering the materials that were being investigated.

SHiELD has been shown to be an extremely useful enhancement to the Laue platform. It not only enables the measurement of further structural information, the technique can also used to increase our understand of the material response beyond the lattice parameters directly observed. This is all achieved without hindering the original Laue platform, where the majority of the information gained by the original technique is preserved.

6.3 MD SIMULATIONS OF SHOCK COMPRESSED GERMANIUM

In order to gain a better understanding of, and support the analysis of the SHiELD study of germanium, a Molecular Dynamics study of shock compressed germanium was undertaken. There has been little previous work on shock compressed germanium and so a detailed Molecular Dynamics study could give insight into its behaviour.

The simulations performed in this work showed that germanium underwent a phase change, although at a higher pressure than gas gun experiments indicated, with thin bands of material being formed. These are qualitatively similar to the bands observed in simulations of silicon. This was seen for both potentials used in this study.

It should be noted that neither potential has been fitted to high pressure work. Therefore the fact that the phase change occurs at a higher pressure, and that the shocked states lie off the experimental Hugoniot, is not surprising. It does lead to some doubt over the study as a whole, however there can still be significant insight gained by taking advantage of the benefits offered from using

molecular dynamics. Namely, this is the ability to look at the behaviour of the material at an atomic level, which has been particularly useful in identifying the structure of the new phase. This was only successful for simulations using the MEAM potential. This was due to the phase changed germanium in the Tersoff simulations being too disordered to analyse effectively. Further work to identify the phase in these simulations would be of benefit. Particularly if they are consistent with the MEAM simulations.

The lattice parameters of the phase changed material were found using the 3DPCF, an analysis technique that is not currently widely used. The significantly lower computational cost was of great benefit. The conventional method of performing this analysis is using Fourier Transform techniques, however more knowledge is required *a priori* when using such techniques.

However, performing an FT of the MD simulations gives a prediction of the diffraction pattern without advance knowledge of the details of the material response. Following this method for the germanium simulations showed that the SHiELD geometry, as it was setup for the two experimental campaigns, would not be able to detect signal from the phase changed material. Therefore it is not surprising that it was not observed.

6.4 SUMMARY

The work in chapter 3 covers the development of a novel in-situ x-ray diffraction technique that aims to overcome many challenges presented when using increasingly large laser facilities. This method of performing diffraction has not been used before in laser-plasma experiments. It utilises existing techniques, such as the recently developed white light x-ray source and a CCD in single photon

counting mode. It was first tested on undriven targets and shown to be able to measure diffraction. Improvements to the technique greatly improved the data quality. However, there were significant difficulties found when analysing data from driven material. The exact cause of this remains unknown.

Chapter 4 similarly covers a new diagnostic. SHiELD enhances the existing white light Laue platform, which can be analysed to gain significantly more information about a material's response under compression. The material response of silicon was shown to be consistent with previous x-ray diffraction work concerning its anomalous elastic response. With a combination of analysis from both VISAR measurements and the SHiELD data, the experiment was also found to be consistent with more recent work concerning the details of the phase change in silicon. A second experimental campaign focussing on germanium found similar behaviour, where elastic compression beyond the HEL was observed. This is consistent with other experimental work on shock compressed germanium.

Following on from this campaign, Molecular Dynamics simulations were performed to support the analysis of the experimental work which are discussed in detail in Chapter 5. Whilst the bulk properties of the shocked germanium do not closely match experimental data, the detailed movements of atoms under compression may still be informative. A detailed study of these simulations gave a prediction of the structure of the phase changed material.

6.5 FUTURE WORK

Greater refinement of the SPEDX technique is required before it is likely to be widely adopted. There are many improvements that have been suggested

in this thesis. These include using a brighter and higher energy backlighter, larger area detectors and alternate camera positions. Alternative choices in target materials, such as silicon or diamond which support high shear stress, may allow for an easier measurement of strain anisotropy.

SHiELD has not yet been able to measure transverse strain, although this was not unexpected considering the materials investigated. Performing the SHiELD technique with metals such as tantalum or copper would be ideal candidates as they have both been found to show transverse strain past the HEL. SHiELD could also be used to investigate either the phase changed material or the presence of twinning. Due to the SHiELD technique supplementing the existing Laue platform, it could easily be used to augment existing Laue campaigns.

Further study, using molecular dynamics, of the mechanism that initiates the phase change in germanium would not only give insight into the material response of germanium; it could also help understanding of how phase changes occur in other cubic diamond materials. More work is required in fitting potentials to high pressure data. This would allow the germanium simulations to more closely match shock hugoniots. Simulations that more closely match experiment would give greater confidence to the mechanisms found using MD. Additionally, performing significantly larger simulations, where large rotations are possible within the simulation, would increase confidence in the work.

REFERENCES

[1] S Seager, M J Kuchner, C A Hier-Majumder, and B Militzer. Mass-Radius Relationships for Solid Exoplanets. *The Astrophysical Journal*, 669:1279, 2007. (Cited on page 1.)

[2] David Charbonneau, Zachory K. Berta, Jonathan Irwin, et al. A super-Earth transiting a nearby low-mass star. *Nature*, 462(7275):891–894, dec 2009. (Cited on page 1.)

[3] D. C. Swift, J. H. Eggert, D. G. Hicks, et al. Mass-Radius Relationships for Exoplanets. *The Astrophysical Journal*, 744(1):59, jan 2012. (Cited on page 1.)

[4] Zachory K. Berta-Thompson, Jonathan Irwin, David Charbonneau, et al. A rocky planet transiting a nearby low-mass star. *Nature*, 527(7577):204–207, 2015. (Cited on page 1.)

[5] Thomas J. Ahrens and V. G. Gregson. Shock compression of crustal rocks: Data for quartz, calcite, and plagioclase rocks. *Journal of Geophysical Research*, 69(22):4839, 1964. (Cited on page 1.)

[6] D. Alfè, G. Price, and M. Gillan. Thermodynamics of hexagonal-close-packed iron under Earth's core conditions. *Physical Review B*, 64(4): 045123, 2001. (Cited on page 1.)

[7] Lars Stixrude, Nico de Koker, Ni Sun, Mainak Mookherjee, and Bijaya B. Karki. Thermodynamics of silicate liquids in the deep Earth. *Earth and Planetary Science Letters*, 278(3-4):226–232, 2009. (Cited on page 1.)

[8] Sarah T. Stewart. Shock Hugoniot of H2O ice. *Geophysical Research Letters*, 30(6):1332, 2003. (Cited on page 1.)

[9] Sarah T. Stewart and Zoë M. Leinhardt. Velocity-Dependent Catastrophic Disruption Criteria for Planetesimals. *The Astrophysical Journal*, 691(2):L133–L137, 2009. (Cited on page 1.)

[10] M. Cuk and S. T. Stewart. Making the Moon from a Fast-Spinning Earth: A Giant Impact Followed by Resonant Despinning. *Science*, 1047 (November):1047–1053, 2012. (Cited on page 1.)

[11] R. L. Akeson, X Chen, D Ciardi, et al. The NASA Exoplanet Archive: Data and Tools for Exoplanet Research. *Publications of the Astronomical Society of the Pacific*, 125(930):989–999, 2013. (Cited on page 1.)

[12] S Anzellini, A Dewaele, M Mezouar, P Loubeyre, and G Morard. Melting of Iron at Earth's Inner Core Boundary Based on Fast X-ray Diffraction. *Science*, 340(6131):464–466, apr 2013. (Cited on page 1.)

[13] G. V. Sin'ko and N. A. Smirnov. Ab initio calculations of elastic constants and thermodynamic properties of bcc, fcc, and hcp Al crystals under pressure. *Journal of Physics: Condensed Matter*, 14(29):6989–7005, 2002. (Cited on page 1.)

[14] Chris J Pickard and R J Needs. Ab initio random structure searching. *Journal of physics. Condensed matter : an Institute of Physics journal*, 23(5):053201, 2011. (Cited on page 1.)

[15] Leonid Dubrovinsky, Natalia Dubrovinskaia, Vitali B Prakapenka, and Artem M Abakumov. Implementation of micro-ball nanodiamond anvils for high-pressure studies above 6 Mbar. *Nature Communications*, 3:1163, 2012. (Cited on pages 1 and 3.)

[16] Bruce A. Remington, Robert E. Rudd, and Justin S. Wark. From microjoules to megajoules and kilobars to gigabars: Probing matter at extreme states of deformation. *Physics of Plasmas*, 22(9):090501, 2015. (Cited on page 1.)

[17] Marvin Ross. The ice layer in Uranus and Neptune - diamonds in the sky? *Nature*, 292(5822):435–436, jul 1981. (Cited on page 2.)

[18] Hugh F Wilson, Michael L Wong, and Burkhard Militzer. Superionic to Superionic Phase Change in Water: Consequences for the Interiors of Uranus and Neptune. *Physical Review Letters*, 110(15):151102, apr 2013. (Cited on page 2.)

[19] Jiming Sun, Bryan K Clark, Salvatore Torquato, and Roberto Car. The phase diagram of high-pressure superionic ice. *Nat Commun*, 6, aug 2015. (Cited on page 2.)

[20] A. Jayaraman. Diamond anvil cell and high-pressure physical investigations. *Reviews of Modern Physics*, 55(1):65–108, 1983. (Cited on page 2.)

[21] P. W. Bridgman. Water, in the Liquid and Five Solid Forms, under Pressure. *Proceedings of the American Academy of Arts and Sciences*, 47 (29):441–558, 1912. (Cited on page 2.)

[22] John C. Jamieson, A. W. Lawson, and N. D. Nachtrieb. New device for obtaining X-ray diffraction patterns from substances exposed to high pressure. *Review of Scientific Instruments*, 30(11):1016–1019, 1959. (Cited on page 2.)

[23] C. E. Weir, E. R. Lippincott, A. Van Valkenburg, and E. N. Bunting. Infrared Studies in the 1- to 15-Micron Region to 30,000 Atmospheres. *Journal of Reasearch of the National Bureau of Standards - A. Physics and Chemistry*, 63A(1):55 – 62, 1959. (Cited on page 2.)

[24] C Weir, S Block, and G Piermarini. Single-Crystal X-ray Diffraction at High Pressures. *Journal of Reasearch of the National Bureau of Standards - C. Engineering and Instrumentation*, 69(4):275–281, 1965. (Cited on page 2.)

[25] M J Edwards, J D Lindl, B K Spears, et al. The experimental plan for cryogenic layered target implosions on the National Ignition Facility - The inertial confinement approach to fusion. *Physics of Plasmas*, 18(5), 2011. (Cited on page 2.)

[26] S H Glenzer, B J MacGowan, N B Meezan, et al. Demonstration of Ignition Radiation Temperatures in Indirect-Drive Inertial Confinement Fusion Hohlraums. *Physical Review Letters*, 106(8):85004, feb 2011. (Cited on page 2.)

[27] M. J. Edwards, P. K. Patel, J. D. Lindl, et al. Progress towards ignition on the National Ignition Facility. *Physics of Plasmas*, 20(7):070501, 2013. (Cited on page 2.)

[28] J M Walsh. Metal Equation of State from Shock Wave Studies. Technical report, Los Alamos Scientific Lab., 1953. (Cited on page 2.)

[29] Dennison Bancroft, Eric L Peterson, and Stanley Minshall. Polymorphism of iron at high pressure. *Journal of Applied Physics*, 27(3):291–298, 1956. (Cited on page 2.)

[30] R F Smith, J H Eggert, R Jeanloz, et al. Ramp compression of diamond to five terapascals. *Nature*, 511(7509):330–333, jul 2014. (Cited on pages 3 and 36.)

[31] L. Dubrovinsky, N. Dubrovinskaia, E. Bykova, et al. The most incompressible metal osmium at static pressures above 750 gigapascals. *Nature*, 525(7568):226–229, 2015. (Cited on page 3.)

[32] John M. Walsh, Melvin H. Rice, Robert G. McQueen, and Frederick L. Yarger. Shock-wave compressions of twenty-seven metals. equations of state of metals. *Physical Review*, 108(2):196–216, 1957. (Cited on page 3.)

[33] A. C. Mitchell and W. J. Nellis. Diagnostic system of the Lawrence Livermore National Laboratory two-stage light-gas gun. *Review of Scientific Instruments*, 52(3):347–359, 1981. (Cited on page 3.)

[34] B. P. Fairand, B. A. Wilcox, W. J. Gallagher, and D. N. Williams. Laser shock-induced microstructural and mechanical property changes in 7075 aluminum. *Journal of Applied Physics*, 43(9):3893–3895, 1972. (Cited on page 3.)

[35] L. C. Yang. Stress waves generated in thin metallic films by a Q -switched ruby laser. *Journal of Applied Physics*, 45(6):2601–2608, 1974. (Cited on page 3.)

[36] T.R Boehly, D.L Brown, R.S Craxton, et al. Initial performance results of the OMEGA laser system. *Optics Communications*, 133(1-6):495–506, 1997. (Cited on page 3.)

[37] E. I. Moses, R. N. Boyd, B. A. Remington, C. J. Keane, and R. Al-Ayat. The National Ignition Facility: Ushering in a new age for high energy density science. *Physics of Plasmas*, 16(4), 2009. (Cited on page 3.)

[38] Nicholas Hopps, Colin Danson, Stuart Duffield, et al. Overview of laser systems for the Orion facility at the AWE. *Applied Optics*, 52(15):3597–607, 2013. (Cited on page 3.)

[39] L. M. Barker. Laser interferometer for measuring high velocities of any reflecting surface. *Journal of Applied Physics*, 43(11):4669, 1972. (Cited on page 4.)

[40] S. D. Rothman and J. Maw. Characteristics analysis of Isentropic Compression Experiments (ICE). *Journal de Physique IV (Proceedings)*, 134: 745–750, jul 2006. (Cited on page 4.)

[41] L. M. Barker and R. E. Hollenbach. Interferometer technique for measuring the dynamic mechanical properties of materials. *Review of Scientific Instruments*, 36(11):1617–1620, 1965. (Cited on page 4.)

[42] D. K. Bradley, J. H. Eggert, R. F. Smith, et al. Diamond at 800 GPa. *Physical Review Letters*, 102(7):075503, feb 2009. (Cited on pages 4 and 36.)

[43] E. J. Hinch. Determining the equation of state of highly plasticised metals from boundary velocimetry. *Journal of Engineering Mathematics*, 68(3-4):279–289, jul 2010. (Cited on page 4.)

[44] J R Rygg, J H Eggert, A E Lazicki, et al. Powder diffraction from solids in the terapascal regime. *Review of Scientific Instruments*, 83(11):113904, nov 2012. (Cited on pages 4 and 36.)

[45] J.H. Eggert, R.F. Smith, D.C. Swift, et al. Ramp compression of tantalum to 330 GPa. *High Pressure Research*, 7959(September):1–16, 2015. (Cited on page 4.)

[46] D. E. Fratanduono, R. F. Smith, D. G. Braun, et al. The effect of nearly steady shock waves in ramp compression experiments. *Journal of Applied Physics*, 117(24):245903, 2015. (Cited on page 4.)

[47] Quitin Johnson, Arthur Mitchell, and L Evans. X-ray Diffraction Evidence for Crystalline Order and Isotropic Compression during the Shock-wave Process. *Nature*, 231(5301):310–311, 1971. (Cited on page 4.)

[48] Quintin Johnson, Arthur C. Mitchell, and L. Evans. X-ray diffraction study of single crystals undergoing shock-wave compression. *Applied Physics Letters*, 21(1):29–30, 1972. (Cited on page 4.)

[49] J. S. Wark, R. R. Whitlock, A. Hauer, J. E. Swain, and P. J. Solone. Shock launching in silicon studied with use of pulsed x-ray diffraction. *Physical Review B*, 35(17):9391–9394, 1987. (Cited on page 5.)

[50] Justin S. Wark, Robert R. Whitlock, Allan A. Hauer, James E. Swain, and Paul J. Solone. Subnanosecond X-ray diffraction from laser-shocked crystals. *Physical Review B*, 40(8):5705–5714, 1989. (Cited on page 5.)

[51] Andrew Higginbotham, Shamim Patel, James A. Hawreliak, et al. Single photon energy dispersive x-ray diffraction. *Review of Scientific Instruments*, 85(3):033906, mar 2014. (Cited on pages 6, 37 and 44.)

[52] Shamim Patel, Matthew J. Suggit, Paul G. Stubley, et al. Single Hit Energy-resolved Laue Diffraction. *Review of Scientific Instruments*, 86 (5):053908, 2015. (Cited on page 6.)

[53] W. H. Bragg and W. L. Bragg. The Reflection of X-rays by Crystals. *Proceedings of the Royal Society of London A: Mathematical, Physical and Engineering Sciences*, 88(605):428–438, 1913. (Cited on page 15.)

[54] D. H. Kalantar, E. A. Chandler, J. D. Colvin, et al. Transient x-ray diffraction used to diagnose shock compressed Si crystals on the Nova laser. *Review of Scientific Instruments*, 70(1999):629, 1999. (Cited on page 17.)

[55] D. H. Kalantar, B. A. Remington, J. D. Colvin, et al. Solid-state experiments at high pressure and strain rate. *Physics of Plasmas*, 7(5):1999, 2000. (Cited on page 17.)

[56] Daniel H. Kalantar, E. Bringa, M. Caturla, et al. Multiple film plane diagnostic for shocked lattice measurements (invited). *Review of Scientific Instruments*, 74(3 II):1929–1934, 2003. (Cited on page 17.)

[57] T G White, J Vorberger, C R D Brown, et al. Observation of inhibited electron-ion coupling in strongly heated graphite. *Scientific reports*, 2: 889, 2012. (Cited on page 17.)

[58] Kouhei Ichiyanagi, Shin Ichi Adachi, Shunsuke Nozawa, et al. Shock-induced lattice deformation of CdS single crystal by nanosecond time-resolved Laue diffraction. *Applied Physics Letters*, 91(23):10–13, 2007. (Cited on page 18.)

[59] Matthew Suggit, Giles Kimminau, James Hawreliak, et al. Nanosecond X-ray Laue diffraction apparatus suitable for laser shock compression experiments. *The Review of Scientific Instruments*, 81(8):083902, aug 2010. (Cited on pages 18, 35, 37 and 70.)

[60] A. J. Comley, B. R. Maddox, R. E. Rudd, et al. Strength of Shock-Loaded Single-Crystal Tantalum [100] Determined using In Situ Broadband X-Ray Laue Diffraction. *Physical Review Letters*, 110(11):115501, mar 2013. (Cited on pages 18 and 70.)

[61] N C Woolsey, J S Wark, and D Riley. Sub-nanosecond X-ray powder diffraction. *Journal of Applied Crystallography*, (23):441–443, 2000. (Cited on page 19.)

[62] J Hawreliak, H E Lorenzana, B a Remington, S Lukezic, and J S Wark. Nanosecond x-ray diffraction from polycrystalline and amorphous materials in a pinhole camera geometry suitable for laser shock compression experiments. *The Review of scientific instruments*, 78(8):083908, aug 2007. (Cited on pages 19 and 25.)

[63] Marc A. Meyers. *Dynamic Behavior of Materials*. Wiley-Interscience, 1994. (Cited on page 20.)

[64] W. J. M. Rankine. On the Thermodynamic Theory of Waves of Finite Longitudinal Disturbance. *Philosophical Transactions of the Royal Society of London*, 160(January):277–288, 1870. (Cited on page 21.)

[65] H Hugoniot. Memoir on the propagation of movements in bodies, especially perfect gases (first part). *J. de l'Ecole Polytechnique*, 57:3–97, 1887. (Cited on page 21.)

[66] Henri Hugoniot. Sur la propagation du movement dans les corps et spécialement dans les gaz parfaits. *J. Ecole Polytechnique*, 58:1–125, 1889. (Cited on page 21.)

[67] James A. Hawreliak, Bassem El-Dasher, Hector Lorenzana, et al. In situ x-ray diffraction measurements of the c/a ratio in the high-pressure ϵ phase of shock-compressed polycrystalline iron. *Physical Review B*, 83 (14):144114, apr 2011. (Cited on pages 23 and 49.)

[68] G E Duvall and R A Graham. Phase transitions under shock-wave loading. *Reviews of Modern Physics*, 49(3):523, 1977. (Cited on page 23.)

[69] R. H. Warnes. Investigation of a Shock-Induced Phase Transition in Antimony. *Journal of Applied Physics*, 38(12):4629, 1967. (Cited on page 24.)

[70] M N Pavlovskii. Formation of metallic modifications of germanium and silicon under shock loading. *Soviet Physics-Solid state*, 9:2514–2518, 1968. (Cited on page 24.)

[71] W. H. Gust and E. B. Royce. Axial yield strengths and two successive phase transition stresses for crystalline silicon. *Journal of Applied Physics*, 42(5):1897–1905, 1971. (Cited on pages 24, 80, 84 and 88.)

[72] Stefan J. Turneaure and Y. M. Gupta. X-ray diffraction and continuum measurements in silicon crystals shocked below the elastic limit. *Applied Physics Letters*, 90(5):051905, 2007. (Cited on page 24.)

[73] A Loveridge-Smith, A Allen, J Belak, et al. Anomalous elastic response of silicon to uniaxial shock compression on nanosecond time scales. *Physical Review Letters*, 86(040):2349–2352, 2001. (Cited on pages 24, 56, 79 and 80.)

[74] Stefan J. Turneaure and Y. M. Gupta. Real-time x-ray diffraction at the impact surface of shocked crystals. *Journal of Applied Physics*, 111(2): 026101, 2012. (Cited on page 24.)

[75] R. F. Smith, R. W. Minich, R. E. Rudd, et al. Orientation and rate dependence in high strain-rate compression of single-crystal silicon. *Physical Review B*, 86(24):245204, dec 2012. (Cited on pages 24 and 80.)

[76] S D Gilev and A M Trubachev. Metallization of silicon in a shock wave: the metallization threshold and ultrahigh defect densities. *Journal of Physics: Condensed Matter*, 16(46):8139, 2004. (Cited on page 25.)

[77] Anil K. Singh and C. Balasingh. The lattice strains in a specimen (hexagonal system) compressed nonhydrostatically in an opposed anvil high pressure setup. *Journal of Applied Physics*, 75(10):4956–4962, 1994. (Cited on page 25.)

[78] Woldemar Voigt. *Lehrbuch der kristallphysik*. Teubner, Liepzig, 1928. (Cited on page 25.)

[79] Andrew Higginbotham and David McGonegle. Prediction of Debye-Scherrer diffraction patterns in arbitrarily strained samples. *Journal of Applied Physics*, 115(17), 2014. (Cited on pages 25 and 50.)

[80] David McGonegle, Despina Milathianaki, Bruce A. Remington, Justin S. Wark, and Andrew Higginbotham. Simulations of in situ x-ray diffraction from uniaxially compressed highly textured polycrystalline targets. *Journal of Applied Physics*, 118(6):065902, 2015. (Cited on page 25.)

[81] David Salzmann. *Atomic physics in hot plasmas*. Number 97. Oxford University Press on Demand, 1998. (Cited on page 27.)

[82] John Ready. *Effects of high-power laser radiation*. Elsevier, 2012. (Cited on page 31.)

[83] S I Anisimov. Vaporization of metal absorbing laser radiation. *Soviet Journal of Experimental and Theoretical Physics*, 27:182, 1968. (Cited on page 31.)

[84] Zhaoyan Zhang and George Gogos. Theory of shock wave propagation during laser ablation. *Physical Review B*, 69(23):1–9, 2004. (Cited on page 31.)

[85] C. Fauquignon. Hydrodynamic Behavior of Solid Deuterium under Laser Heating. *Physics of Fluids*, 13(2):386, 1970. (Cited on page 32.)

[86] D. L. Matthews, E. M. Campbell, N. M. Ceglio, et al. Characterization of laser-produced plasma x-ray sources for use in x-ray radiography. *Journal of Applied Physics*, 54(8):4260, 1983. (Cited on page 35.)

[87] Y. Ping, F. Coppari, D. G. Hicks, et al. Solid Iron Compressed Up to 560 GPa. *Physical Review Letters*, 111(6):065501, aug 2013. (Cited on page 36.)

[88] J. Biener, D.D. Ho, C. Wild, et al. Diamond spheres for inertial confinement fusion. *Nuclear Fusion*, 49(11):112001, nov 2009. (Cited on page 36.)

[89] A. Lazicki, J. R. Rygg, F. Coppari, et al. X-Ray Diffraction of Solid Tin to 1.2 TPa. *Physical Review Letters*, 115(7):1–5, 2015. (Cited on page 36.)

[90] Matthew J Suggit, Andrew Higginbotham, James A Hawreliak, et al. Nanosecond white-light Laue diffraction measurements of dislocation microstructure in shock-compressed single-crystal copper. *Nature Communications*, 3:1224, jan 2012. (Cited on pages 37, 70, 72 and 80.)

[91] B. R. Maddox, H. S. Park, B. A. Remington, et al. Absolute measurements of x-ray backlighter sources at energies above 10 keV. *Physics of Plasmas*, 18(5):0–6, 2011. (Cited on page 37.)

[92] Barukh Yaakobi, Frederic J. Marshall, Thomas R. Boehly, Richard P. J. Town, and David D. Meyerhofer. Extended x-ray absorption fine-structure experiments with a laser-imploded target as a radiation source. *Journal of the Optical Society of America B*, 20(1):238, 2003. (Cited on page 37.)

[93] Bertram E Warren. *X-ray Diffraction*. DoverPublications. com, 1969. (Cited on pages 38, 57, 58 and 89.)

[94] I. J. Paterson, R. J. Clarke, N. C. Woolsey, and G. Gregori. Image plate response for conditions relevant to laser-plasma interaction experiments. *Measurement Science and Technology*, 19(9):095301, 2008. (Cited on page 41.)

[95] Princeton Instruments. Princeton Instruments CCD Data, 2016. (Cited on page 41.)

[96] GR Hopkinson. Charge diffusion effects in CCD x-ray detectors: I. Theory. *Nuclear Instruments and Methods in Physics Research*, 216:423–429, 1983. (Cited on page 41.)

[97] Claude A. Klein. Bandgap Dependence and Related Features of Radiation Ionization Energies in Semiconductors. *Journal of Applied Physics*, 39(4):2029, 1968. (Cited on page 41.)

[98] KJ McCarthy and Alan Owens. Modelling the X-ray response of charge coupled devices. *Nuclear Instruments and Methods in Physics Research A*, 9002(95), 1995. (Cited on page 41.)

[99] R. Devanathan, L.R. Corrales, F. Gao, and W.J. Weber. Signal variance in gamma-ray detectorsâĂŤA review. *Nuclear Instruments and Methods in Physics Research Section A: Accelerators, Spectrometers, Detectors and Associated Equipment*, 565(2):637–649, sep 2006. (Cited on page 42.)

[100] T. Papp, M.-C. Lépy, J. Plagnard, G. Kalinka, and E. Papp-Szabó. A new approach to the determination of the Fano factor for semiconductor detectors. *X-Ray Spectrometry*, 34(2):106–111, mar 2005. (Cited on page 42.)

[101] C Stoeckl, W Theobald, T. C. Sangster, et al. Operation of a single-photon-counting x-ray charge-coupled device camera spectrometer in a petawatt environment. *Review of Scientific Instruments*, 75(2004):3705–3707, 2004. (Cited on page 42.)

[102] J. A. King, K Akli, R. A. Snavely, et al. Characterization of a picosecond laser generated 4.5 keV Ti K -alpha source for pulsed radiography. *Review of Scientific Instruments*, 76:12–14, 2005. (Cited on page 42.)

[103] Luca Labate, M. Galimberti, A. Giulietti, et al. A laser-plasma source for CCD calibration in the soft X-ray range. *Nuclear Instruments and Methods in Physics Research, Section A: Accelerators, Spectrometers, Detectors and Associated Equipment*, 495(2):148–153, 2002. (Cited on page 43.)

[104] Flavio Zamponi, Tino Kämpfer, Andreas Morak, Ingo Uschmann, and Eckhart Förster. Characterization of a deep depletion, back-illuminated charge-coupled device in the x-ray range. *Review of Scientific Instruments*, 76(11):1–3, 2005. (Cited on page 43.)

[105] LK Townsley and PS Broos. Mitigating charge transfer inefficiency in the Chandra X-ray Observatory Advanced CCD Imaging Spectrometer. *The Astrophysical Journal*, pages 1–4, 2008. (Cited on page 43.)

[106] S. Patel, MJ Suggit, P Stubley, et al. CLF Annual Report: Single Photon Energy Dispersive X-ray Diffraction (SPEDX). Technical report, Rutherford Appleton Laboratory, 2013. (Cited on page 48.)

[107] C. E. Wehrenberg, A. J. Comley, N. R. Barton, et al. Lattice-level observation of the elastic-to-plastic relaxation process with subnanosecond resolution in shock-compressed Ta using time-resolved in situ Laue diffraction. *Physical Review B*, 92(10):104305, 2015. (Cited on pages 54 and 55.)

[108] Graeme M Hansford. PoDFluX: a new Monte Carlo ray-tracing model for powder diffraction and fluorescence. *The Review of scientific instruments*, 80(7):073903, jul 2009. (Cited on page 56.)

[109] Theo Hahn, Uri Shmueli, A J Arthur James Cochran Wilson, and Edward Prince. *International tables for crystallography.* D. Reidel Publishing Company, 2005. (Cited on page 57.)

[110] BL Henke, EM Gullikson, and JC Davis. X-Ray Interactions: Photoabsorption, Scattering, Transmission, and Reflection at E= 50-30,000 eV, Z= 1-92. *Atomic data and nuclear data tables*, 1993. (Cited on pages 59 and 85.)

[111] Manfred Otto Krause. Atomic radiative and radiationless yields for K and L shells. *Journal of physical and chemical reference data*, 8(2):307–327, 1979. (Cited on page 59.)

[112] M O Krause and J H Oliver. Natural widths of atomic K and L levels, Ka X-ray lines and several KLL Auger lines. *J. Phys. Chem. Ref. Data*, 1979. (Cited on page 59.)

[113] Karl Pearson. Regression, heredity, and panmixia. *Philosophical Transactions of the Royal Society of London*, 187:253–318, 1896. (Cited on page 65.)

[114] A. Higginbotham, P. G. Stubley, A. J. Comley, et al. Inelastic response of silicon to shock compression. *Scientific Reports*, 6(April):24211, 2016. (Cited on pages 70, 82 and 88.)

[115] R. I. Barabash, G. E. Ice, B. C. Larson, and Wenge Yang. Application of white x-ray microbeams for the analysis of dislocation structures. *Review of Scientific Instruments*, 73(3 II):1652, 2002. (Cited on page 70.)

[116] A George. Measurements of the Dislocation Velocities in Silicon. *Journal de Physique Colloques*, 40(C6):133–137, 1979. (Cited on page 73.)

[117] P. M. Celliers, G. W. Collins, L. B. Da Silva, D. M. Gold, and R. Cauble. Accurate measurement of laser-driven shock trajectories with velocity interferometry. *Applied Physics Letters*, 73(10):1320, 1998. (Cited on page 74.)

[118] Andrew Loveridge-Smith. *Quantitative analysis of shock propagation in crystals by use of time resolved x-ray diffraction.* PhD thesis, University of Oxford, 2001. (Cited on page 80.)

[119] Gabriele Mogni, Andrew Higginbotham, Katalin Gaál-Nagy, Nigel Park, and Justin S. Wark. Molecular dynamics simulations of shock-compressed single-crystal silicon. *Physical Review B*, 89(6):064104, feb 2014. (Cited on pages 80, 102, 107 and 112.)

[120] Stefan J. Turneaure and Y. M. Gupta. Inelastic deformation and phase transformation of shock compressed silicon single crystals. *Applied Physics Letters*, 91(20):201913, 2007. (Cited on pages 80 and 88.)

[121] Nick W Hopps, Thomas H Bett, Nicolas Cann, et al. Overview of Project Orion. volume 7916, pages 79160C–79160C–10, 2011. (Cited on page 82.)

[122] T Goto, T Sato, and Y Syono. Reduction of Shear Strength and Phase-Transition in Shock-Loaded Silicon. *Japanese Journal of Applied Physics*, 1982. (Cited on page 88.)

[123] Paul Stubley, David McGonegle, Shamim Patel, et al. Hydrocode and Molecular Dynamics modelling of uniaxial shock wave experiments on Silicon. *Bulletin of the American Physical Society*, 60, 2015. (Cited on page 88.)

[124] W. H. Gust and E. B. Royce. Axial yield strengths and phase-transition stresses for <100>, <110>, and <111> germanium. *Journal of Applied Physics*, 43(11):4437–4442, 1972. (Cited on pages 99, 109 and 110.)

[125] Kazutaka G. Nakamura, Hidetaka Kawano, Hiroaki Kishimura, et al. Picosecond time-resolved X-ray diffraction from a laser-shocked germanium crystal above hugoniot elastic limit. *Japanese Journal of Applied Physics, Part 1: Regular Papers and Short Notes and Review Papers*, 43 (8 A):5477–5479, 2004. (Cited on page 99.)

[126] Kazutaka G. Nakamura, Yoichiro Hironaka, Hidetaka Kawano, Hiroaki Kishimura, and Ken-Ichi Kondo. Picosecond time-resolved X-ray diffraction from laser-shocked semiconductors. *Laser and Particle Beams*, 22 (03):285–288, jul 2004. (Cited on page 99.)

[127] B. J. Alder and T. E. Wainwright. Studies in molecular dynamics. General method. *Journal of chemical physics*, 31(2):459, 1959. (Cited on page 100.)

[128] B J Alder. Computer dynamics. *Annu. Rev. Phys. Chem.*, 24:325, 1973. (Cited on page 100.)

[129] Kai Kadau, Timothy C. Germann, and Peter S. Lomdahl. MOLECULAR DYNAMICS COMES OF AGE: 320 BILLION ATOM SIMULATION ON BlueGene/L. *International Journal of Modern Physics C*, 17(12): 1755–1761, 2006. (Cited on page 100.)

[130] J E Jones. On the Determination of Molecular Fields. II. From the Equation of State of a Gas. *Proceedings of the Royal Society of London A: Mathematical, Physical and Engineering Sciences*, 106(738):463–477, oct 1924. (Cited on page 100.)

[131] R. A. Johnson. Empirical potentials and their use in the calculation of energies of point defects in metals. *Journal of Physics F: Metal Physics*, 3(2):295–321, 1973. (Cited on page 100.)

[132] J Tersoff. Modelling of solid-state chemistry: Interatomic potentials for multicomponent systems. *Physical Review B*, 39(8):5566–5568, 1989. (Cited on pages 100 and 102.)

[133] M. I. Baskes. Modified embedded-atom potentials for cubic materials and impurities. *Physical Review B*, 46(5):2727–2742, 1992. (Cited on page 100.)

[134] John A Moriarty. Density-functional formulation of the generalized pseudopotential theory. *Physical Review B*, 16(6):2537–2555, 1977. (Cited on page 100.)

[135] Kai Kadau, Timothy C Germann, Peter S Lomdahl, and Brad Lee Holian. Microscopic view of structural phase transitions induced by shock

waves. *Science (New York, N.Y.)*, 296(5573):1681–4, may 2002. (Cited on page 101.)

[136] A. Higginbotham, M. J. Suggit, E. M. Bringa, et al. Molecular dynamics simulations of shock-induced deformation twinning of a body-centered-cubic metal. *Physical Review B*, 88(10):104105, sep 2013. (Cited on pages 101, 112 and 123.)

[137] Steve Plimpton. Fast Parallel Algorithms for Short-Range Molecular Dynamics, 1995. (Cited on page 101.)

[138] Kejian Ding and Hans Andersen. Molecular-dynamics simulation of amorphous germanium. *Physical Review B*, 34(10):6987–6991, 1986. (Cited on page 101.)

[139] J. Q. Broughton and X. P. Li. Phase diagram of silicon by molecular dynamics. *Physical Review B*, 35(17):9120–9127, 1987. (Cited on page 101.)

[140] P L Novikov, Zh V Smagina, and A V Dvurechenskii. Formation of Germanium Nanoislands on Pit-Patterned Silicon Substrates by Means of the Molecular Dynamics Method. *Optoelectronics, Instrumentation and Data Processing*, 50(3):247–251, 2014. (Cited on page 101.)

[141] J. M D Lane and Aidan P. Thompson. Molecular dynamics simulation of shock-induced phase transition in germanium. *AIP Conference Proceedings*, 1195(May 2015):1157–1160, 2009. (Cited on pages 101, 112 and 116.)

[142] You Lin, Romain Perriot, Vasily V. Zhakhovsky, et al. Shock-induced phase transition in diamond. *AIP Conference Proceedings*, 1426:1171–1174, 2012. (Cited on pages 102 and 107.)

[143] E. M. Bringa, J. U. Cazamias, P. Erhart, et al. Atomistic shock Hugoniot simulation of single-crystal copper. *Journal of Applied Physics*, 96(7): 3793, 2004. (Cited on page 102.)

[144] Eun Ha Kim, Young-Han Shin, and Byeong-Joo Lee. A modified embedded-atom method interatomic potential for germanium. *Computer Coupling of Phase Diagrams and Thermochemistry*, 32(1):34–42, 2008. (Cited on page 102.)

[145] Brad Lee Holian, William G Hoover, Bill Moran, and Galen K Straub. Shock-wave structure via nonequilibrium molecular dynamics and Navier-Stokes continuum mechanics. *Physical Review A*, 22(6):2798–2808, dec 1980. (Cited on page 103.)

[146] B. L. Holian. Plasticity Induced by Shock Waves in Nonequilibrium Molecular-Dynamics Simulations. *Science*, 280(5372):2085–2088, jun 1998. (Cited on page 103.)

[147] A. Higginbotham, J. Hawreliak, E. M. Bringa, et al. Molecular dynamics simulations of ramp-compressed copper. *Physical Review B*, 85(2):024112, jan 2012. (Cited on page 103.)

[148] R.A. Graham, O.E. Jones, and J.R. Holland. Physical behavior of germanium under shock wave compression. *Solid State Communications*, 27 (5):1519–1529, may 1966. (Cited on page 111.)

[149] J A Moriarty, J F Belak, and R E Rudd. Quantum-based atomistic simulation of materials properties in transition metals. *Journal of Physics: Condensed Matter*, 2825(11), 2002. (Cited on page 112.)

[150] R. Ravelo, T. C. Germann, O. Guerrero, Q. An, and B. L. Holian. Shock-induced plasticity in tantalum single crystals: Interatomic potentials and large-scale molecular-dynamics simulations. *Physical Review B - Condensed Matter and Materials Physics*, 88(13):1–17, 2013. (Cited on page 112.)

[151] In-Ho Lee, Ji-Wook Jeong, and K. J. Chang. Invariant-molecular-dynamics study of the diamond-to-ÎŠ-Sn transition in Si under hydrostatic and uniaxial compressions. *Physical Review B*, 55(9):5689–5693, 1997. (Cited on page 112.)

[152] E. M. Bringa, J. U. Cazamias, P. Erhart, et al. Atomistic shock Hugoniot simulation of single-crystal copper. *Journal of Applied Physics*, 96(7): 3793–3799, 2004. (Cited on page 112.)

[153] Giles Kimminau, Paul Erhart, Eduardo M. Bringa, Bruce Remington, and Justin S. Wark. Phonon instabilities in uniaxially compressed fcc metals as seen in molecular dynamics simulations. *Physical Review B - Condensed Matter and Materials Physics*, 81:1–4, 2010. (Cited on page 113.)

[154] A. E. Gleason, C. A. Bolme, H. J. Lee, et al. Ultrafast visualization of crystallization and grain growth in shock-compressed SiO2. *Nature Communications*, 6:8191, 2015. (Cited on page 122.)

[155] Harold T. Stokes and Dorian M. Hatch. FINDSYM: Program for identifying the space-group symmetry of a crystal. *Journal of Applied Crystallography*, 38(1):237–238, 2005. (Cited on page 127.)

[156] David McGonegle, Despina Milathianaki, Bruce Remington, Justin Wark, and Andrew Higginbotham. Investigations into uniaxial deformation of textured polycrystalline targets using X-ray diffraction. In *APS Shock*

Compression of Condensed Matter Meeting Abstracts, volume 1, page 1003, 2015. (Cited on page 134.)

COLOPHON

This document was typeset using the typographical look-and-feel `classicthesis` developed by André Miede. The style was inspired by Robert Bringhurst's seminal book on typography "*The Elements of Typographic Style*". `classicthesis` is available for both LaTeX and LyX:

`http://code.google.com/p/classicthesis/`

Happy users of `classicthesis` usually send a real postcard to the author, a collection of postcards received so far is featured here:

`http://postcards.miede.de/`

Final Version as of October 16, 2016 (`classicthesis`).